SLAC-PUB-13664
July 2009

Experimental studies of light emission phenomena in superconducting RF cavities[+]

P.L. Anthony[a], J.R. Delayen[b], D. Fryberger[a, *], W.S. Goree[c, ✦], J. Mammosser[b,d], Z. M. Szalata[a], J.G. Weisend II[a]

[a] *SLAC National Accelerator Laboratory, Menlo Park, CA 94025*
[b] *Thomas Jefferson National Accelerator Facility (TJNAF), Newport, News, VA 23606*
[c] *2G Enterprises, Pacific Grove, CA 93950*
[d] *Present Affiliation: The SNS Facility, Oak Ridge National Laboratory, Oak Ridge, TN*

Abstract

Experimental studies of light emission phenomena in superconducting RF cavities, which we categorize under the general heading of cavity lights, are described. The cavity lights data, which were obtained using a small CCD video camera, were collected in a series of nine experimental runs ranging from ~½ to ~2 h in duration. The video data were recorded on a standard VHS tape. As the runs progressed, additional instrumentation was added. For the last three runs a LabVIEW controlled data acquisition system was included. These runs furnish evidence for several, possibly related, light emission phenomena. The most intriguing of these is what appear to be small luminous objects ≤ 1.5 mm in size, freely moving about in the vacuum space, generally without wall contact, as verified by reflections of the tracks in the cavity walls. In addition, on a number of occasions, these objects were observed to bounce off of the cavity walls. The wall-bounce aspect of most of these events was clearly confirmed by pre-bounce and post-bounce reflections concurrent with the tracks. In one of the later runs, a mode of behavior was observed that was qualitatively different from anything observed in the earlier runs. Perhaps the most perplexing aspect of this new mode was the observation of as many as seven luminous objects arrayed in what might be described as a macromolecular formation, coherently moving about in the interior of the cavity for extended periods of time, evidently without any wall contact. It is suggested that these mobile luminous objects are without explanation within the realm of established physics. Some remarks about more exotic theoretical possibilities are made, and future plans are discussed.

PACS: 46.90 + s; 52.80 Mg
Keywords: Field emission; cavity lights

1. Introduction

In 1999, Delayen and Mammosser [1] reported observations of glowing filaments of light suspended in the vacuum space of superconducting niobium RF cavities. These observations were obtained using a small CCD video camera[1] looking along the axis into the cavity. The original purpose of the experiment was to study field emission phenomena. Two different experimental setups were used, one with a single-cell cavity and one with a five-cell cavity. Similar results were obtained in both setups. It was reported that: "Three general classes of glowing filaments were observed: 1) regular-

[+] Supported by the Department of Energy Contracts DE-AC02-76SF-00515 and DE-AC05-84ER40150.

[*] Corresponding author. E-mail address: fryberger@slac.stanford.edu (D. Fryberger).Tel.: + 1-650-926-2768.

[✦] Deceased

[1] Monochrome Micro Camera, Model H53004, Edmund Scientific Optics and Optical Catalogue N991A, 1999, p. 177.

shaped closed, 2) irregular-shaped closed, and 3) open." We reproduce in Fig. 1 the example of 1) as shown in Fig. 2a of Ref. [1]. As discussed in *Sec. 5.1*, this is a track representing a ~16 ms time exposure of a small luminous object moving about in the vacuum space of the cavity. We shall use the acronym MLO to refer to these mobile luminous objects.

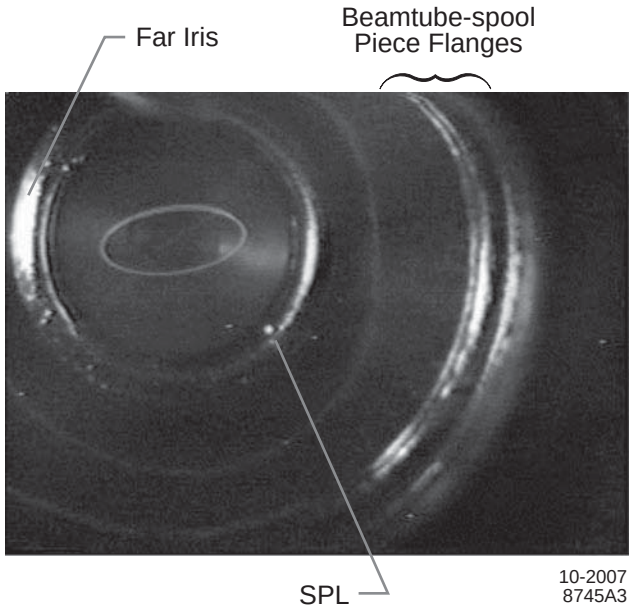

Figure 1. Video frame (field) of a closed filament in the single-cell data. (Orbit No. 4 of Table I. For reference purposes, the eccentricity, ε, of the ellipse in this figure is 0.9.) A glowing point of light or SPL (see text) is indicated. The arcs of light reflected from the flange joining the beamtube to the spool piece are also indicated.

These MLO's were completely unexpected. In order to study further this most intriguing phenomenon, the ALE (Anomalous Light Experiment) Collaboration was formed with membership from SLAC, TJNAF, and 2G Enterprises. The goals of this collaboration are: 1) to determine the conditions that are conducive to the occurrence of cavity lights, and 2) to understand the underlying physics.

Subsequent to the initial two runs, a number of additional experimental runs have been undertaken. This present paper includes additional analysis of the data from the initial two runs as well a discussion of data obtained in seven subsequent experimental runs. Table I gives a brief overview of these runs. Through a more detailed analysis of the data from these runs, we found that there are several light emission phenomena that appear to have a physics relationship to the MLO's. Furthermore, in Run 7, as described in **Sec. 7**, MLO's were observed behaving in ways that were qualitatively different from anything seen in the earlier runs. This observation introduces a significant level of additional complexity into the cavity lights phenomena. In addition to the data analysis, some remarks about theoretical possibilities and plans for future work are also included.

For convenient reference, we list in Table II various luminous phenomena seen in these runs, including brief descriptions of their salient characteristics. As described below, there were a number of occasions in which two or more of these phenomena were present in the cavity at the same time.

2. Initial experimental setups

The initial test performed in this series, which we call Run 1, used a single-cell superconducting niobium RF cavity of the standard CEBAF design [1], which operates at 2 K and resonates at 1.5 GHz. It was installed vertically in one of the cryogenic test dewars in the TJNAF Vertical Test Area (VTA). The CCD camera (maintained at 295 K by an electric heater) was mounted in an evacuated space attached to the bottom flange of the cavity as depicted in Fig. 2. Thus, the camera had an unobstructed view looking up along the cavity axis. A sapphire viewport isolated the camera vacuum (instrumentation vacuum) from the cavity vacuum. These two vacua were pumped separately.

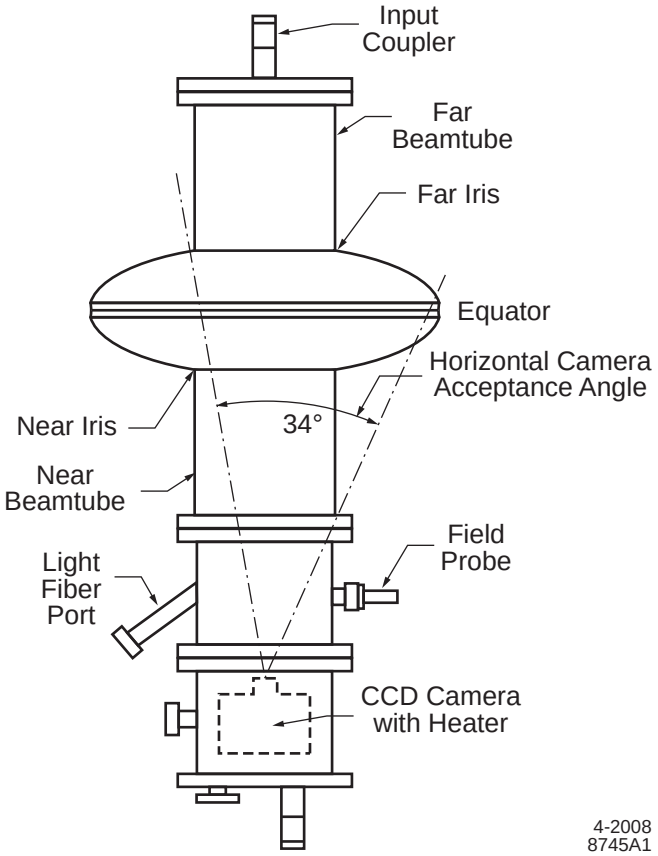

Figure 2. Schematic depiction of experimental setup used in Run 1 for single-cell cavity (not to scale). The iris regions are indicated as well as the horizontal acceptance angle that is viewed by the camera.

An RF input coupler was affixed to the top flange on the cavity; there was no electron beam present in this or any of the follow-on experiments. (Of course, as mentioned below, at times there were electrons present from field emission.) Also included, as indicated in Fig. 2, are a light fiber port and a field probe. The light fiber port made it possible to illuminate the interior of the cavity and hence to verify the operation of the CCD camera. Reflections of this illumination from the interior surfaces of the cavity are indicated in Fig. 1. The pair of arcs of larger radius derives from the flanges joining the near beamtube to the spool piece, and the arcs of smaller radius are from the surface of the cavity interior near the far iris. The near iris is not easily visible via its reflections, but its location can be deduced by other means (see below).

The field probe enables one to monitor the electric field strength in the cavity. The signal from this probe is rectified and fed to the cavity RF power control unit where it represents the transmitted power as a cavity parameter. The five-cell setup for Run 2 used a production CEBAF five-cell cavity, fitted with the same CCD camera, as depicted in Fig. 3. For all of the runs reported here, the output of the CCD camera was recorded in black and white on a standard VHS tape.

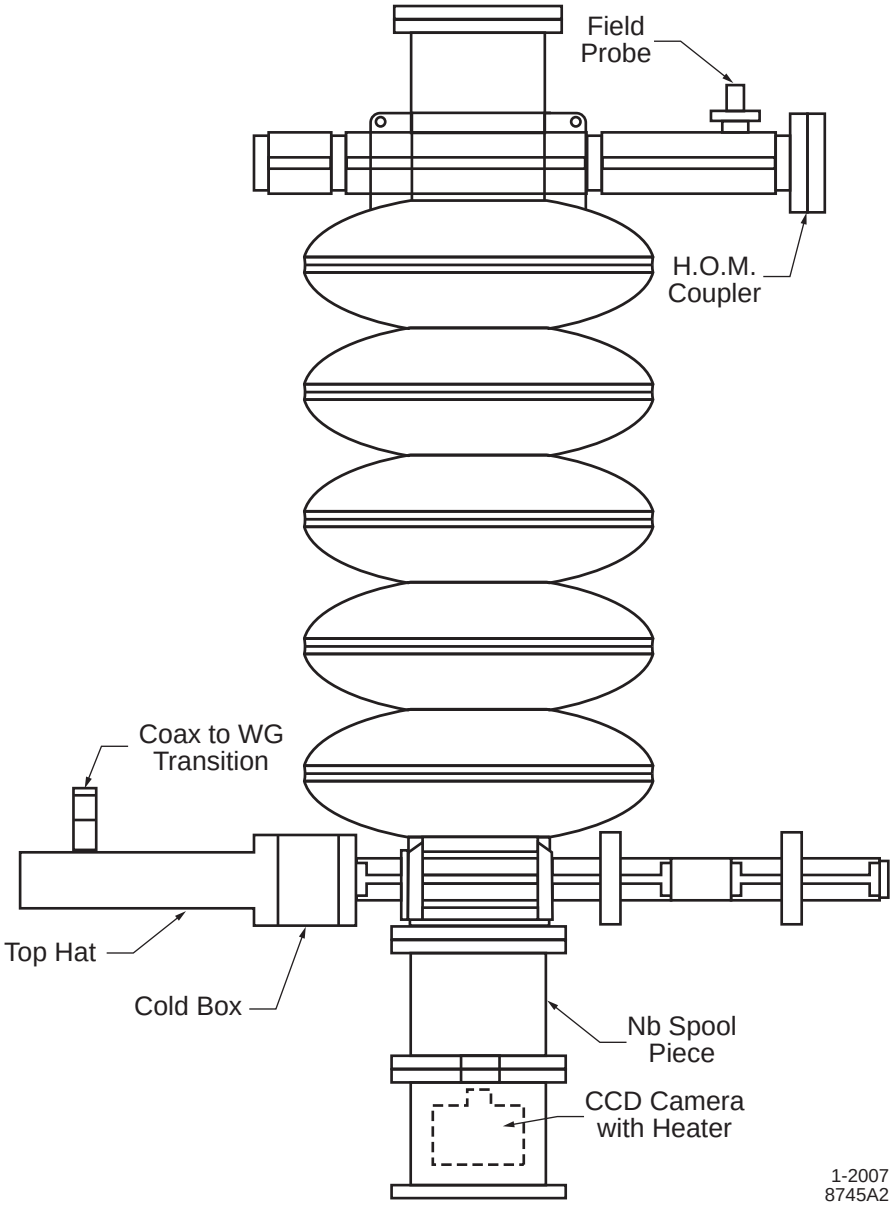

Figure 3. Schematic depiction of experimental setup for the five-cell cavity used in Run 2 (not to scale).

3. Video format and frame sequence numbering

The analysis reported herein has been pursued using a high-end home VCR[2] and its (digital) frame-by-frame scan feature. In order to better understand the analysis using the VCR, it is useful to review the NTSC video signal format [2] used in the U.S.A., which

[2] JVC Hi-Fi Stereo Video Cassette Recorder Model HR-S8000U

consists of frames of 525 lines produced at a rate of 29.97 frames/s. Each frame comprises a sequence of two interlaced fields; each field contains half of the lines allocated to the frame. The use of interlaced fields reduces the bandwidth requirement for video transmission and at the same time eliminates flicker in the eye of the observer. The CCD exposure for each field of the video waveform is done separately and lasts a nominal $1/60^{th}$ of a second, which, for our CCD camera, is the maximum available shutter open time for each field. Since the CCD exposure must be complete before the contents of the individual pixels can be converted into a video waveform, the camera delays by one field the timing of the input light. For most applications this fact is unimportant, but it needs to be kept in mind when comparing the timing of the recorded video data to that of the recorded DAQ (Data Acquisition System, Run 7 et seq.) data. This maximum available shutter open time for each field is reduced by the need to readout the CCD after the (electronic) shutter closes. This readout function takes place during the blanking time between the two fields, which reduces the displayed frame format from 525 lines to 480 lines. This blanking time is used to make time available to insert the vertical synchronization pulses into the video waveform [2]. (There are also horizontal blanking intervals at the end of each line used to insert horizontal synchronization pulses and provisions for color reference signals.) It is important to note that the vertical synchronization sequences preceding Field 1 and Field 2 are slightly different, which difference electronically defines Field 1 as the first field of the relevant frame.

We have acquired a "reference" video camera[3] (with the same specifications as the original camera) to use for the study of various details of camera performance. These CCD cameras automatically vary the shutter open time to adjust for the light intensity of the subject. Measurements on the (reference) camera indicate that the CCD dead time for the readout between fields (when the auto-electronic iris is fully open) is 0.28 ± 0.02 ms.

Thus, for dark subjects the frame and field format allow for a maximum shutter open time of ~ 16.4 ms for each field (a live time of 98%). For bright subjects the auto-electronic iris can, depending upon subject brightness, reduce the shutter open time to as little as 0.1 ms (a live time of 0.6%). As far as our video data is concerned, the extent to which the (continuous) fiber illumination, mentioned above, reduces the maximum shutter open time is not known, but the track segment study discussed below indicates that the shutter is open for most, if not all, of the available live time (except during bright CID's, for which we sometimes observed a significant effect upon abrupt CID extinction). Thus, the sequence of fields and frames comprise a sequence of "time exposures" of fields of 1/60 s duration. Two sequential fields are paired to comprise an interlaced frame, yielding a nominal frame rate of 30/s.

When using a home VCR in the frame-by-frame scan mode, only first field in each frame is displayed (at least in the several VCR's tested by the authors). One result of this single field display feature is that when using the frame-by-frame scan mode it sometimes was not possible to locate the specific frame of a flash that had been observed when viewing the tape at its standard real-time viewing mode of 30 frames/s. This was because the flash occurred in the second field of the relevant frame. This conclusion was verified by using a tape copied such that the frame pairing of the fields was inverted. (See below.) As discussed below, the data recorded by the DAQ in Run 7 indicates that the flash typically drains all of the energy from the cavity and that it takes one or more frames to recover.

[3] Monochrome Micro Camera, Model WAT-660A, Watec America Corp.

(That a flash drains all of the energy from a superconducting cavity was experimentally demonstrated by Phillips et al [3], who studied RF windows employed with CEBAF 5-cell cavities.) Thus, the presence of flashes in the un-scanned field in the frame-by frame scan can often be deduced from the dark field (which includes the momentary extinguishing of the extant SPL's) in the subsequent frame(s).

To assist in further analysis of the video data, frame numbers were incorporated by elementary means into the data tapes. The arrangement to generate a VHS tape with sequential frame numbering is depicted in Fig. 4. The frame sequence from this tape with the sequential frame numbering, as given by the count on the scaler, was then inserted into a corner of a copy of the original data tape using the picture-in-picture (PIP) feature of our VCR. See Fig. 5. (N. B. Just as the CCD camera entails a timing delay, the digitizing requirement of the PIP feature also entails a timing delay.) While this step obscured a portion of the video frame, for most events the interesting portion of the screen was still fully visible. Also, no data was lost; should a portion of an interesting track or track sequence be obscured by the PIP insertion, one could always refer back to the original data tape. (Note that Figs. 1, 6, 25, and 27 were taken from the original video data tape before the frame numbers were added.)

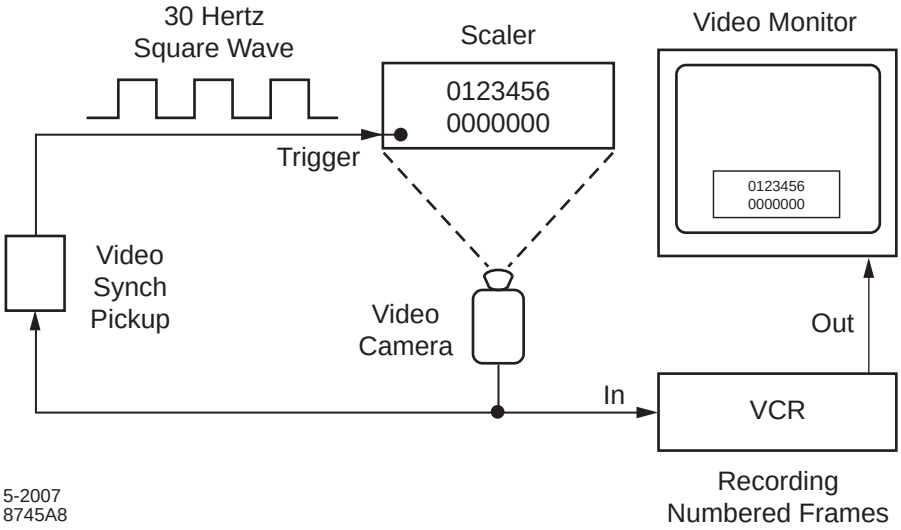

Figure 4. Arrangement to furnish a VHS tape with each frame numbered. The video camera views a scaler that is triggered by a 30 Hz square wave derived from the vertical synchronization portion of the camera video output waveform. The incrementation of the scaler is fast enough to fall fully within the video blanking time. (As is evident in the video frames that include this PIP insert (e. g., Fig. 8), one can see that the camera also recorded an image of the lab equipment that happened to be behind the scaler.)

The final result, then, was a (copy of the original) VHS data tape with frames that each included a sequential frame number. Proper incrementation and legibility of this number sequence was verified using a frame-by-frame scan of this derived data tape. The initial frame number representing "t = 0" for a tape copy of a given run varied somewhat due to coordinating the start times of the three VCR's (Fig. 5). But the nonzero frame number for "t = 0" on the tape does not impair the main purpose for the frame numbers: to locate (and relocate) and study specific events and event sequences of interest. Most of the data analysis using these frame numbers (and DAQ sample numbers) was done by using Excel spreadsheets supplemented by the Chart Wizard and Mathcad.

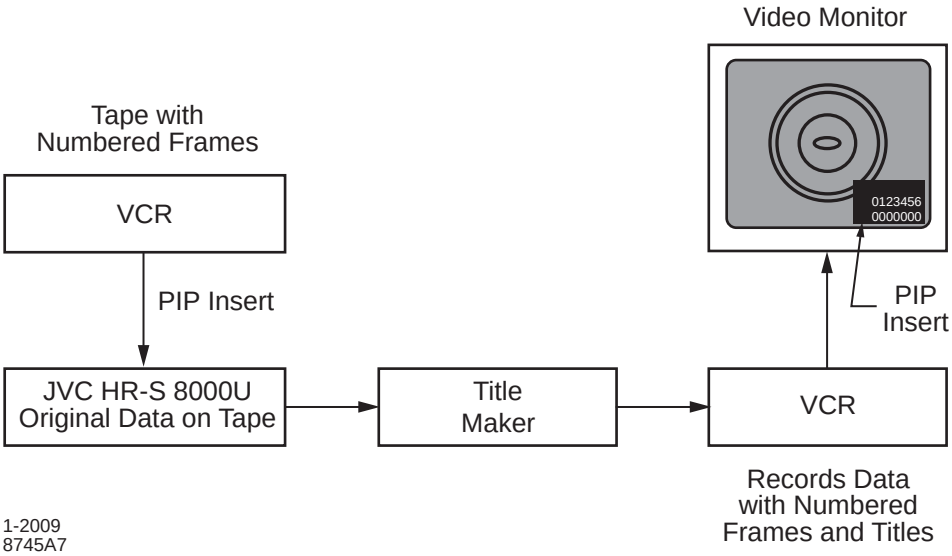

Figure 5. Configuration using three VCR's and the PIP feature (in one of them: HR-S8000U) for numbering the frames on a derived VHS data tape. The PIP insert is indicated. Titles, or other information, can also be added in this step as shown.

4. Overview of initial data

In Runs 1 and 2, as the accelerating gradient was increased at the beginning of the runs, SPL's were the first of these luminous phenomena to be observed. In Run 2, the onset of observable SPL's was found to be at a gradient of ~3MV/m. And various SPL's remained in view throughout these runs whenever there was an adequate accelerating gradient in the cavity. As one would expect, the amount of light emission from these sites tends to correlate with the magnitude of the accelerating gradient, and hence they are a useful indicator of the gradient.

While we attribute these SPL's to a field emission process, the specific physics involved or their relationship to the MLO phenomenon is not clear. In this regard, it is relevant to note that there are two intriguing sequences involving SPL's described in *Sec. 5.4*. These sequences support the notion that (some of) the flashes and the SPL's are specifically associated with field emission sites. They also imply the possibility that (some) flashes, SPL's, and MLO's are related phenomena.

MLO's are the most intriguing of the luminous phenomena observed in this series of runs, and they are the major focus of our interest. The intrigue derives from the challenge to find a proper physics understanding of the MLO phenomenon. These MLO's occurred with cavity accelerating gradients in the range of 2 to 4.4 MV/m, but this phenomenon was actually quite episodic. Often, the MLO's would appear subsequent to a flash of light, or FoL (discussed in more detail below). Usually, the tracks of the MLO's (if they appeared) would last only a few frames. However, there were three video tape segments in which the continuous existence of MLO's was observed in a sequence of frames (orbits) of more than 10 s duration: two (single MLO orbits) in the single-cell data, and one (containing three contemporaneous MLO orbits) in the five-cell data. In these segments it appears that the MLO's were orbiting the axis of the cavity without any wall contact. Fig. 6, which reproduces Fig. 5a from Ref. [1], is an early frame the (only) orbit

sequence in Run 2. In this sequence (which appeared right after a flash), there initially appear to be three orbiting MLO's (note the three track segments indicated in Fig. 6: Orbits 11, 12, and 13, as listed below in Table IV), soon reduced to two, both of which disappeared at about the same time ~11 s later. Another category of MLO behavior was also observed in Run 1; that is, there were examples of MLO's bouncing off of the cavity walls. Reflections of these tracks in the cavity walls concurrent with the directly viewed MLO tracks assisted in the analysis of these events.

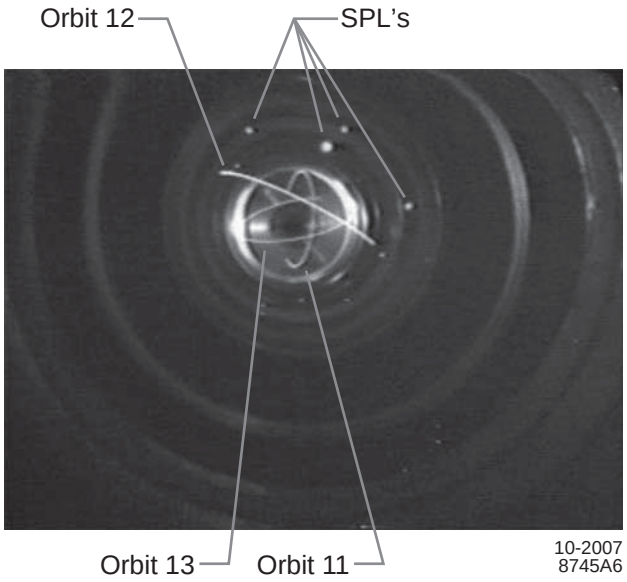

Figure 6. Video frame (field) of orbiting MLO's in the long-lived episode observed in Run 2. The three track segments are from the Orbits 11, 12, and 13, as indicated. Also, several SPL's are indicated. The concentric arcs of the irises, easily seen in this figure, are mainly due to reflections of the light generated by the MLO's and SPL's. As in Run 1, light was introduced into the cavity via a fiber optics cable, and this light also contributes to the visibility of the irises.

Finally, we note that we frequently observed numerous spatially and temporally uncorrelated speckles in the video data (sometimes dozens in a single field of a single frame), which we attribute to X-radiation hitting individual pixels in the CCD camera. The X rays would be bremsstrahlung generated by accelerated field emission electrons hitting the cavity walls. These speckles do not appear to have any obvious direct relationship to the cavity lights phenomena reported herein, but they are good indicators of copious field emission. (Also, their density tends to correlate with the cavity gradient.)

5. Additional analysis of initial data

5.1 Small moving objects appear as extended filaments

From the above discussion we see that when the VHS tape is viewed at normal speed, one is continuously (except for the small segments of time utilized for CCD readout and the automatic light intensity control feature) observing the interior of the cavity as a 60/s sequence of 16.4 ms time exposures. In this situation, then, to an observer's eye a small moving glowing object will appear in the video display as an extended glowing filament. And for orbits of frequency $\geq$ 60 Hz, even a freeze-frame view will look like a filament (e. g., Fig. 1). However, for slow moving objects observed using a frame-by-frame scan, one obtains a segmented track, one segment per (field of each) frame; the length of each

segment depends upon the velocity of the object and the shutter open time. In this scan, the empty portions between track segments, which are approximately the same length as the segmented tracks, are recorded on Field 2 of each frame, which is skipped by the VCR in the frame-by-frame scan mode.

Using a frame-by-frame scan mode, it is easy to trace out a (partial, i. e., the Field 1 parts of the) trajectory of an object on a transparency sheet ad-fixed to the face of the video monitor. Such a tracing was done for a 10-frame sequence starting at Frame 62799 in which the MLO in question entered the camera view at the bottom, appearing to emerge (from the main cavity volume) into view from behind the near iris. After its entry, the MLO moved up, slowed and reversed its direction, and then accelerated downward; it was not visible in the 11th frame. The resultant 10 track segments from this tracing are depicted in Fig.7. (For geometric reference purposes, locations of the reflections from the far iris and an estimate of the location of the near iris are indicated.) To give an idea of the actual video representation of this track, we reproduce in Fig. 8 a digital photograph[4] of Frame 62800, as displayed in freeze-frame on the video monitor. It is interesting to observe in this figure that there are track segments from other MLO's that were simultaneously moving about in the cavity.

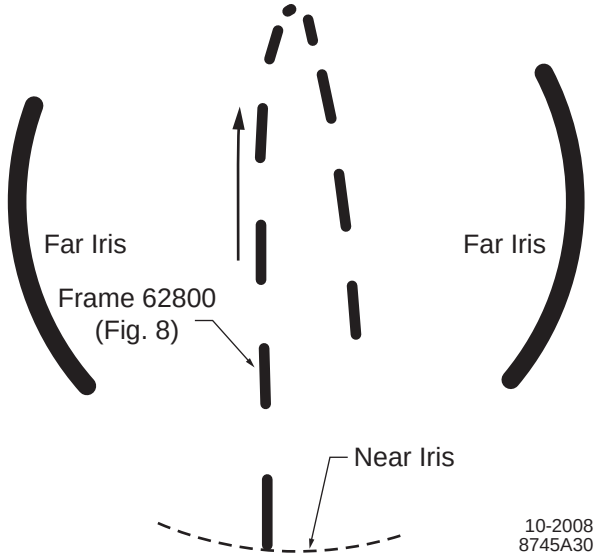

Figure 7. Depiction of segmented track as obtained from 10 frames (starting at Frame 62799) of a (Field 1) frame-by-frame scan taken from Run 1. An arrow indicates the direction of travel. The track segment exhibited in Fig. 8 is indicated.

[4] Sony Model DSC-H9.

Figure 8. Digital photograph of the freeze-frame display of (Field 1 of) Frame 62800 (as can be seen in the PIP insert in the lower right hand corner). The MLO track segment as seen in the MLO trajectories of Figs. 7 and 10 is indicated.

We found that in the frame numbering procedure (Figs. 4 and 5) and the making of copies of the frame-numbered tapes, the VCR sometimes reversed the vertical synchronization sequences that define Field 1 and Field 2. This electronic error modifies the collection of the fields into the frames of the output video tape: Field 1 becomes Field 2 (of the prior frame) and Field 2 becomes Field 1, as depicted in Fig. 9. Of course, the real-time sequence of the fields is unchanged. We were able to utilize this error to obtain a field-reversed output tape for all of the major events on the original data tape. This is a useful result for the analysis: using the frame-by-frame scans of these field-reversed tapes, one can view on the video monitor a sequence of the second fields from the original tape and fill in the gaps in a trajectory (or investigate other Field 2 aspects of Δt < 16 ms, e. g., a flash). Using this technique, we depict in Fig. 10 the same event (sequence) as in Fig. 7, but show the second-field segments of each frame (of the original tape). Also in this figure we show, in outline, the (Field 1) track segments of Fig. 7. We see that the second-field segments fit nicely into the gaps between the first-field segments. The fact that this composite trajectory appears to be essentially complete indicates that the auto-electronic iris of the video camera is fully (or nearly fully) open.

This analysis, of which Figs. 7 and 10 are examples, verifies that what we are calling MLO's are not (linear) glowing filaments or discharges, but are indeed small luminous objects moving about inside the cavity. It is obvious, then, that for the faster moving objects, the filament-like appearance is a result of the ~16 ms time exposure/field.

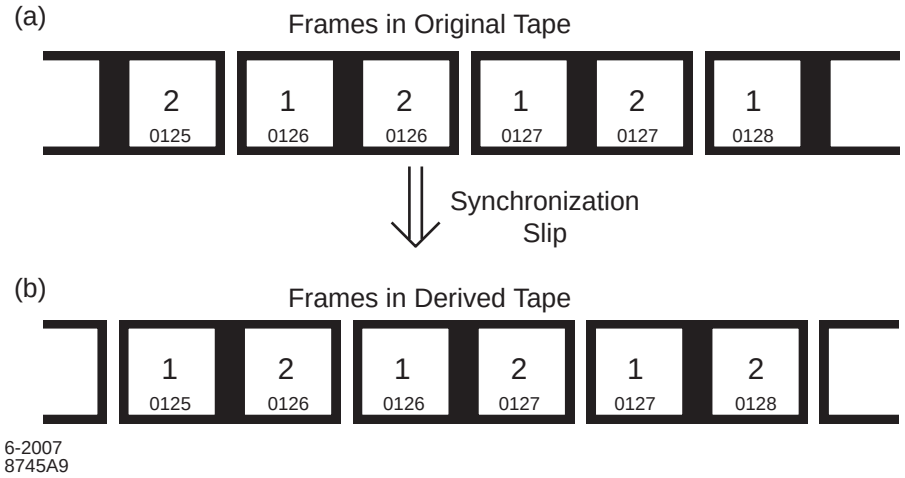

Figure 9. a. Field/Frame sequence in a properly synchronized tape. b. Field/Frame sequence after VCR improperly reverses the vertical synchronization sequences. Note that the original PIP frame numbers are now split between two adjacent frames, as re-defined by the electronic signature reversal.

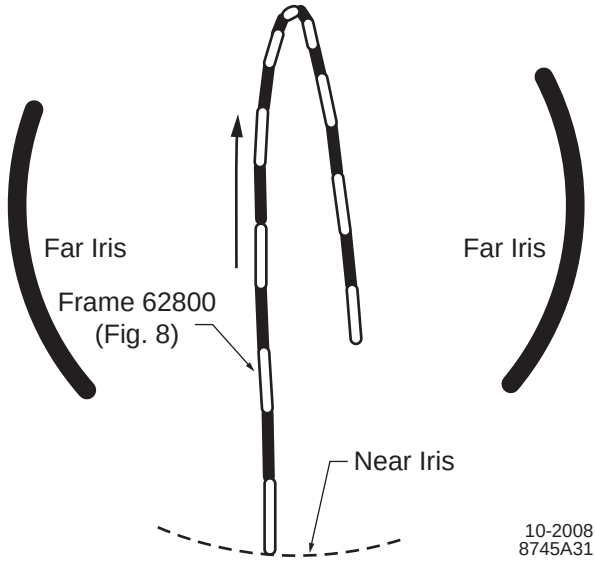

Figure 10. A depiction of the Field 2 track segments (of the original tape) of the same event sequence as in Fig. 7. The (Field 1) segments as shown in Fig. 7 are also shown here in outline, completing the depiction of the 10-frame video trajectory.

5.2 Camera resolution and object size

Camera resolution depends upon a number of factors: 1) the lens optics, 2) the pixel count of the CCD, 3) the line density of the raster scan (vertical resolution), and 4) the video bandwidth (horizontal resolution). Since the CCD pixel count is 537(H)×505(V), we expect that the camera resolution will be determined by other factors. In examining single fields that contain narrow almost horizontal track segments (See Fig. 11), we conclude that (in the absence of other effects) it is the line density (240 lines/field) that determines the (best possible) vertical resolution for MLO's. Since these 240 lines cover the 26° vertical acceptance of the camera, one obtains 1.9×10^{-3} radians/field line. For a

distance of 25 cm (in Run 1) between the camera lens and the equatorial plane of the cavity, we obtain ~0.5 mm/line as a suitable figure for the (best possible) vertical resolution for tracks in the equatorial plane. This estimated value for our resolution is somewhat inferior to that generally taken for NTSC video systems, which is 340 lines [4]. The reason, of course, is that in our case the lines of only one field are available for measurement purposes. By examination of thin, vertically moving tracks as well as the X ray stimulation of individual CCD pixels (mentioned above), we conclude that the (best) horizontal resolution is about the same as the vertical. Hence, we can say that many of the observed MLO tracks in Run 1 appear to be ≤ 0.5 mm in width (one field line).

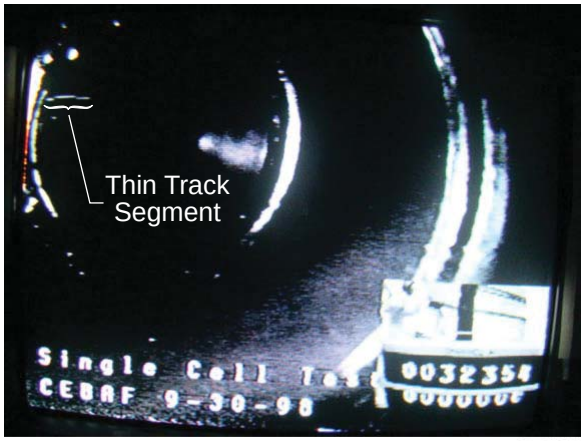

7-2008
8745A23

Figure 11. Nearly horizontal (very thin) track segment in a single field of Frame 32354 from Run 1, indicating the limit of (the best) vertical resolution. This track segment is part of Orbit 1 (See Table IV), is concave downward, orbiting CW, and moving from left to right. One can see that this (curved) track, as it advances, is visible in only one field line at a time. (The vertical line count is 240/field.)

In consideration of the tracks that appear to be as large as 1.5 mm (cf. Fig. 15), it is appropriate to explore further the "other factors" alluded to above. These include the fact that the lens-object distance is below the camera specification (≥16 in), possible chromatic aberrations, and image blooming as a function of object brightness. We have studied these effects in the reference camera and have concluded that at an object distance of 25 cm such effects may augment the apparent video image size by a factor of two or more, depending upon the spectrum and optical intensity of the object. Thus, the notion that some MLO's appear to be as large as 1.5 mm in size should be viewed with caution until better data is available. (We do not estimate the sizes for the MLO's in Run 2, but they appear to be comparable to those in Run 1.)

Similarly, there is a size distribution of the apparent luminous diameter of the SPL's; the largest of these appears to be ~ 2 mm. But again, some caution is appropriate. First, we observe that at times these SPL's appear to be quite bright, which would tend to augment the size of their luminous image. In addition, there is evidence that SPL's radiate the bulk of their energy into the red and near infrared (NIR) region (630 to 1000 nm) [5], and as a consequence, one expects an additional image size augmentation due to a residual chromatic aberration of the lens at the long wavelength limit of the camera acceptance. (The camera does not have an IR filter, and has some sensitivity even out to 1000 nm.) This NIR augmentation was confirmed by measurements using our reference camera).

5.3 Initial luminous phenomena

As mentioned above, SPL's were the first of the luminous phenomena to be observed at the beginning of these initial runs. (Examples of SPL's are indicated in Figs. 1 and 6.) Specifically, in Run 1 the first SPL's appeared in Frame 4967 and remained luminous for 1106 frames. There were then brief appearances (Frames 6140 through 6143 and again in Frames 12086 through 12091) of an SPL in the same location as the initial SPL. The next SPL series began at Frame 12168, which was followed by an MLO, starting at Frame 12174 with track segments in 8 sequential frames. These data are interesting because there was no observed precursor flash to this initial MLO, only the SPL sequences. Since the SPL's remained visible through the initial frames of the MLO, we did not tabulate the additional light in the cavity as a flash (See *Sec. 5.5*, below.); this additional light, in fact, appeared to be due to a significant brightening of the SPL's.

The initial sequence of luminous phenomena observed in Run 2 started off (in Frame 23231) as in Run 1 with fairly extended periods of visible SPL's, varying in brightness in response to varying accelerating gradients. There were also some (field emission) speckles seen in this time period. This initial sequence culminated in a flash in Frame 40641. The interior of the cavity as seen (later) in Frame 40643 (See Fig. 12a.) appears to have only the externally introduced light, having the same light pattern seen in Frames <23231. (The continued presence of the externally introduced light in Runs 1 and 2 made it difficult to clearly discern gradient induced, low-level luminous effects. In Runs ≥3 we only used externally introduced illumination prior to the run, which light furnished a reference for the cavity interior.) At Frame 40696 the SPL's began to be visible again. At Frame ~41000, et seq., some speckles were again evident. In the succeeding frames, in addition to the brightening SPL's and more frequent speckles, we observed a continuing brightening of a general interior illumination. This is an example of what we have categorized as a CID. While this CID enabled one to see outlines of the interior irises, its source is not evident; it does not appear to be associated with the SPL's. Another interesting aspect of this CID is that the light level appears uniform throughout the video raster. Thus, it appears to overlay the darker regions of the cavity (e. g., the apertures opening into the resonant cells of the cavity and the far flange) without rendering any of the interior details more discernable. (Similar optical effects were also seen in later runs.) The uniformly illuminated video raster suggests the possibility that the CID induced a ruby fluorescence in the sapphire viewport window. (See discussion in *Sec. 8.1*.) This CID continued to brighten (See Fig. 12b.), culminating in a flash (saturating all of the CCD pixels) in Frame 42787 (See Fig. 12c.). In Fig. 12d we show Frame 42789, in which there is no gradient induced luminosity and the externally introduced luminosity is evidently reduced by (a vestige of) the action of the auto-electronic iris, being activated by the high light level of the prior CID. (The fact that the SPL's were extinguished after the flash is consistent with the argument that the flash drains all of the energy from the cavity. See further discussions below.) The initial orbital sequence (for Orbit 11) starts in Frame 42796 (See Table IV).

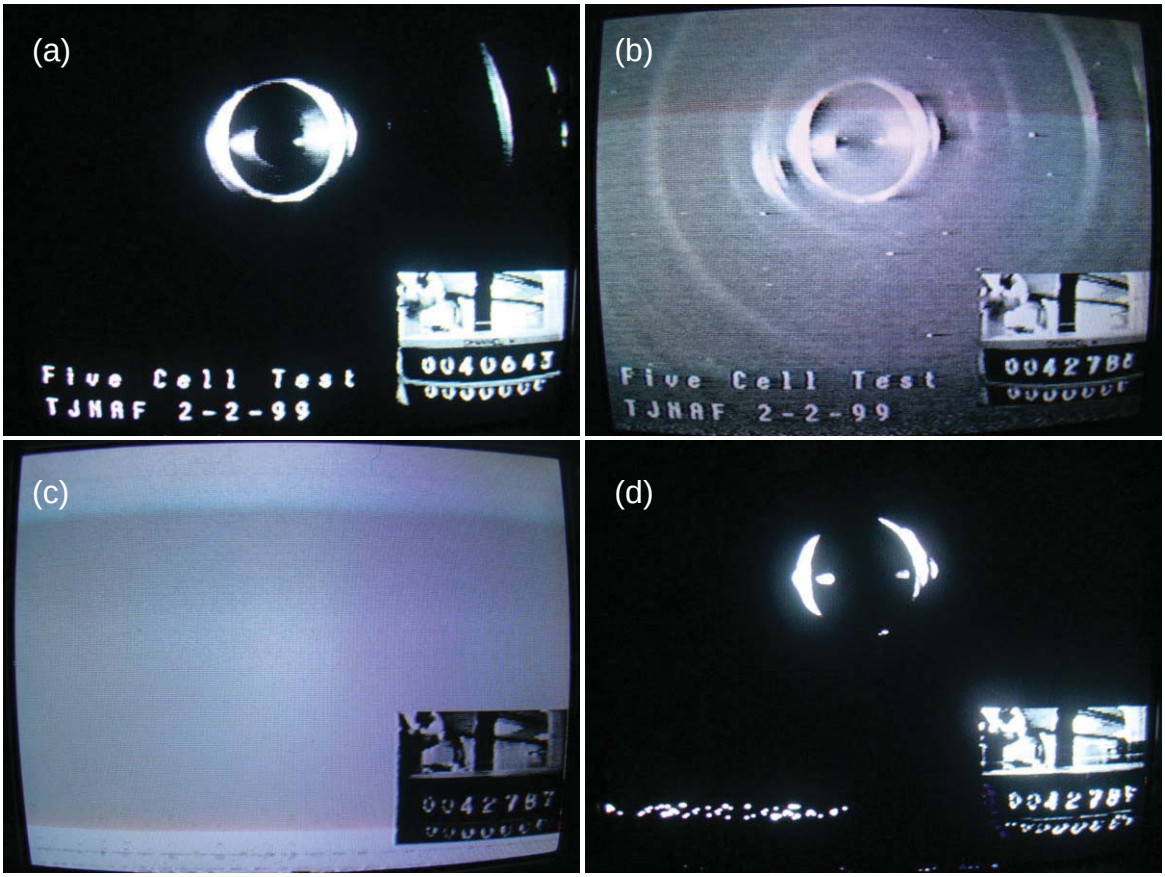

7-2008
8745A29

Figure 12. a. Frame 40643: only externally introduced light; b. Frame 42786: a bright CID; c. Frame 42787: a saturating flash; d. Frame 42789: only the externally introduced light, but diminished by the auto-electronic iris.

5.4 Field emission sites, SPL's, flashes, and MLO's

That SPL's remain stationary whenever they are visible and that they are located on or near the irises (regions of highest electric field) furnish prima facie evidence that SPL's are associated with field emission sites. This assertion is consistent with the fact that simultaneous optical luminescence and electron emission from small, localized sources on surfaces in evacuated cavities at room temperature have been observed. Such results have been found both for high DC gradients at a cathode surface [6] and for high (pulsed) RF gradients in the maximum gradient region of a copper reentrant $\lambda/4$ (1.5 GHz) cavity [5].

At this juncture, an interesting question is: what is the relationship of SPL's to flashes and MLO's. Relevant to this latter question, we include below descriptions of two video sequences that accompany flashes found in Run 1. The first, shown in Fig. 13, is a (Field 1) sequence from four contiguous frames starting at Frame 28634. In the first frame we see a quiescent, track-free cavity with several bright SPL's, as indicated. (These SPL's had been continuously visible for >500 frames prior to Frame 28634.) In the second frame we see a general illumination from a mild flash with an MLO track appearing to start out across the cavity from the location of one of the indicated SPL's. In the third and

fourth frames we see the track continuing out across the cavity. Immediately after the "launch" frame, we observe that the indicated SPL's are no longer visible; presumably the flash has drained the energy from the cavity (cf. the discussion of the flashes in Run 7: *Sec. 7.2.3.*). If it is true that the RF energy has been drained from the cavity, an interesting question is: where at this juncture does the optical energy radiated by the MLO come from? Though not shown, the missing track segments are visible (as in Figs. 7 and 10) in the second fields of the relevant frames. The MLO track then moved across the cavity for 4 more frames (also not shown) at which point it bounced off the near beamtube (as confirmed by track reflections; wall-bounce events are described in *Sec. 5.10.1*) and disappeared. A most intriguing feature of this event, however, is that the "launch" SPL does not reappear in subsequent frames, although all of the others do. This assertion is confirmed in the next sequence (Fig. 14).

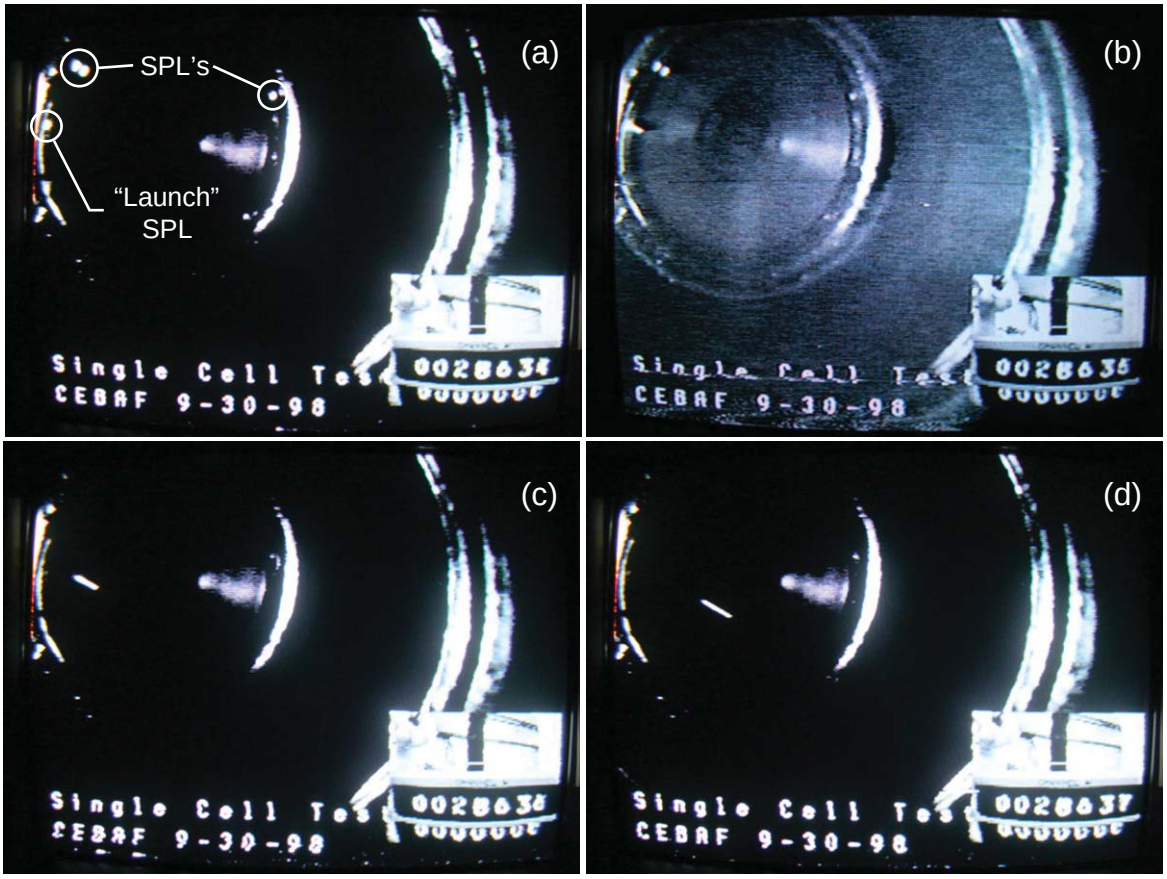

10-2008
8745A27

Figure 13. The apparent launching of an MLO from an SPL site (indicated): a four-frame sequence starting at Frame 28634. As in Fig. 7, we show the (Field 1) MLO track segments as they trace out the trajectory.

The second sequence is shown in Fig. 14. The first three images are of three contiguous fields taken from two adjacent frames. (The second field is obtained from a tape that is field-reversed with respect to the tape furnishing the first and third; recall the NTSC video format discussion above.) In the first image (with frame label 30142) we see a quiescent cavity with the accelerating gradient adequate to render several (indicated) SPL's to be luminous. In the next field (with frame label 30143/28607) we see the general illumination of the flash as well as what appears to be debris flying into the cavity with the point of divergence located at one of the SPL's. (This luminous debris has some

resemblance to that shown in Fig. 2 of Ref. [5].) In the next field (with frame label 30143) we see a track that appears to be a late stage of the debris jet. This implies that the time of the crest of the flash was near the end (within ~1 ms, say) of the field labeled 30143/28607. (Later measurements, discussed below, indicate that flash durations are 1 to 2 ms.) Finally, we show Frame 30187, in which the cavity is again energized and the SPL's are again luminous at what appears to be their original brightness. We note, however, that the SPL from which the debris appeared to originate is no longer visible. (Note also the absence in this sequence of the launch SPL seen at the beginning of the first sequence.)

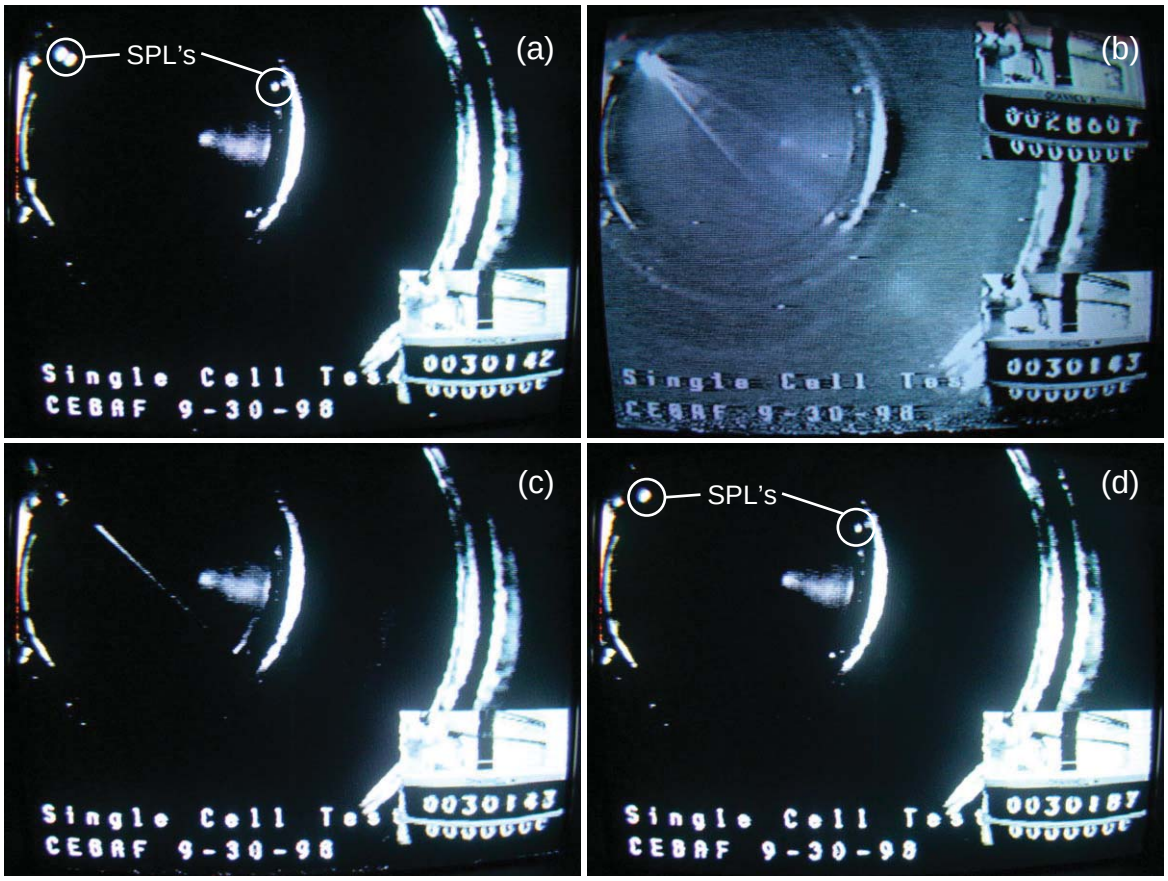

Figure 14. A sequence of three contiguous fields showing the apparent destruction of an SPL site. In the second (and third) field we can see debris radiating from the location of the SPL. Finally, we show a later frame (30187), in which the SPL in question is absent. Also note the absence throughout this sequence of the "launch" SPL seen in Fig. 13.

While there may be some other explanation, the sequences shown in Figs. 13 and 14 offer significant support for the hypothesis that flashes are associated with the explosive destruction of individual field emission sites [7]. And the diminution late in Run 1 of the MLO phenomenon as a whole (i. e., the incidence of tracks, orbits, and flashes; see next section), if field emission sites are an important aspect, is consistent with the elimination of field emission sites by standard (RF) processing procedures of superconducting cavities [7, 8].

It is interesting to observe that the characteristics of the objects moving out from the two SPL sites appear to be qualitatively different in nature. The MLO in Frame 28636 is moving relatively slowly, and its (apparent) track width appears to be fairly uniform along its length, at about two to three field lines wide. To better evaluate this statement, we reproduce (using Adobe Photoshop Elements) a blow-up of this track segment in Fig. 15. While the (lowest order) camera calibration derived in the prior section would indicate a track width possibly as large as 1.5 mm, due consideration of image spreading associated with the optical effects mentioned above imply that the MLO size is actually smaller, perhaps even at or below the video line resolution limit of 0.5 mm. On the other hand, the "debris" tracks emanating from the SPL explosion event appear to vary significantly from near the (apparent) source SPL to the end of their visible trajectory, being thicker and brighter near the beginning and dimmer and at (or below) the system resolution near the end. Also their velocity is several times that of the MLO in the first sequence. Quantitative evaluation of the debris tracks is complicated by the fact that near the explosion site there is a considerable amount of luminous activity and possibly many tracks. As one looks at the tracks farther from the SPL, they are fewer in number and can be seen to be relatively thin. This observation is quite noticeable in Frame 30143. However, it may be that the relative track brightness could affect the apparent track width. (Are these debris objects incandescent solid or liquid ejecta, cooling as they move away from the explosion source point?)

7-2008
8745A20

Figure 15. A blow-up of the track segment seen in Frame 28636 of Fig. 13. The seven bumps seen along the upper and lower borders of this segment are artifacts of the TV field lines that comprise the luminous portion of the image. As such, they furnish a scale that enables an estimate of the (apparent maximum) track width.

5.5 Production rates of FoL's, and MLO's

To date, the data from Run 1 contained by far the most FoL's and MLO's; we examine here their production rates over the course of that run. The data compiled for this section were obtained by scanning (and rescanning) the entire tape at 30 frames/s, and stopping whenever one of these transient luminous phenomena was observed. We then went back and identified the specific frame containing the event in question. (Often this required examining a field-reversed tape, as in Fig. 14.) The frame number was then tabulated along with a note describing the event. (FoL's and MLO's were the objects of separate scanning runs, but, of course, appropriate tabulations were made when found.)

The category FoL contains both flashes and semi-flashes as subcategories. A flash is defined as a brief (seen in only one field) generally distributed area of luminosity in the camera view-field, but not necessarily covering the entire field. (Occasionally the flash saturates all of the CCD pixels, as shown in Fig. 12c.) To be categorized as a flash, it was also required that all of the visible SPL's would be extinguished for at least one subsequent field. (There were always enough visible SPL's to enable us to apply this criterion.) A semi-flash consists of a significant region of luminosity (in only one field), but one which did not extinguish the SPL's present. (In the succeeding fields, sometimes the SPL's became noticeably dimmer, but usually not.) An example of a semi-flash is given in Fig. 16.

7-2008
8745A15

Figure 16. A semi-flash event in Frame 136436.

An MLO was identified by a track segment resembling the one in Fig. 15. In the subsequent frames, usually, but not always, there were MLO tracks that were clearly continuations of the initially observed segment(s). (The most extreme examples of MLO's tracks continuing for many frames are discussed below in *Sec. 5.8: Orbits*.) For the purposes of this tabulation of MLO production rates, only the frame (number) containing the initial segment of the MLO track sequence was tabulated. As specific examples of the application of these criteria, we note that the event detailed in Fig. 13 was tabulated as a Flash and an MLO in Frame 28635 (the only such coincidence in the run), while the event detailed in Fig. 14 was tabulated as (only) a flash in Frame 30143.

Using the above criteria, we tabulated 50 flashes, 80 semi-flashes, and 245 MLO's in the 90 min (~162000 frames) run, which correspond to rather small (average) event probabilities/frame: 3×10^{-4}, 5×10^{-4}, and 1.5×10^{-3}, respectively. Hence, it is more informative to plot the running time integrals of these distributions (rather than the densities) as a function of time, which we do in Fig. 17. The (local) slope of the line in each category is proportional to the (local) rate of event production in that category, and the final point gives the total event count for the run. From this plot it is easy to discern the episodic nature of these phenomena. (For the first ~5 min power was not yet applied to the cavity.) The high production rates tended to coincide with the program of increasing in steps the accelerating gradient in the cavity. The periods of low (or null) rates can be attributed to the power being off to make various adjustments to the apparatus, or to when the gradients were less than those already applied.

The most active period of MLO production occurred in an 11.6 min interval starting 27.3 min into the run (cf., Fig. 17). This period of high MLO production (167/245) coincided with more than half of the flash production (32/50) and a significant fraction (20/80) of the semi-flash production. (For a later comparison, we note that the FoL production rate in this 11.6 min period was ~2.5×10^{-3}/frame.) It is also of interest to note that the semi-flash events didn't start until the 30th min, and that almost all of the flash events occurred in the first 40 min of the run. The fact that the flash production essentially stopped less than half way through the run offers support for the earlier speculation that flashes are associated with the explosive destruction of field emission sites by RF processing of the cavity. The continued existence of visible SPL's in the cavity at the end of the run implies that the maximum applied accelerating gradient was inadequate to process away all of the extant field emission sites. (Supporting this implication is the large number of CCD speckles seen in the video frames at the end of the run.) The continued production of (a rather high rate of) semi-flash events after the 40th min would indicate that semi-flashes are associated with other unknown conditions in the cavity.

5.6 Tabulation errors, qualitative discussion

Although relatively small tabulation errors (i. e., overcounts and undercounts) do not impinge on the validity of the phenomena themselves, we give here a brief discussion to help inform an evaluation of Fig. 17. Because the definition of a flash includes the easily recognizable SPL-extinction criterion, the flash tabulation is the most accurate, entailing an error of perhaps ±2 at most. We suppose that the tabulation error in the MLO count is somewhat larger (±6, say). Undercounts are possible as a result of missing a short one-segment MLO (We do not address undercounts due to the possibility that there may be MLO-like objects below the threshold of visibility; see Fig. 32.), and overcounts are possible should an MLO move out of the view of the camera, returning several frames later to be tabulated as a new MLO. (For example, if the MLO tracked in Fig. 7 had had enough kinetic energy to move out of the camera view for one or two frames, it could have been counted twice. And such behavior is indeed possible, for as we shall describe in *Sec. 5.8*, some of the MLO's did, in fact, move out of the camera's view for portions of their orbits.) Also, the occasional MLO flurry, i. e., numerous MLO's in the same video field, further complicated the tabulation process. As an example, we give Fig. 18 which reproduces Frame 136445, in which we indicate 3 MLO track segments in addition to that of Orbit 10. This flurry appeared soon after the semi-flash observed in Frame 136436 (shown in Fig. 16), and accounts for the large step in MLO counts at ~75 min. (This semi-flash did not terminate the orbit, as flashes were observed to do; see *Sec. 5.8*.)

Since the criteria for a semi-flash includes a qualitative evaluation of luminous intensity in terms of brightness and area, the notion of tabulation error is not really applicable. (There were, in fact, numerous examples of semi-flash candidates, particularly later in the run, that were deemed too weak for inclusion in the tabulation.) Hence, we do not furnish a tabulation error estimate for semi-flashes.

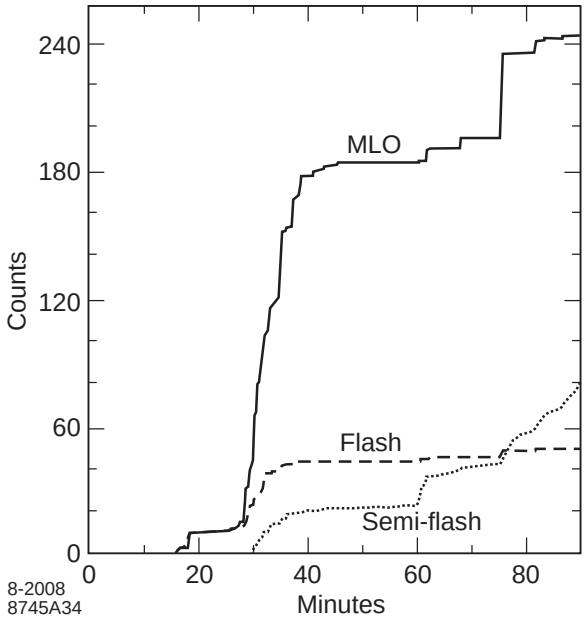

Figure 17. Running integrals of events found in Run 1: Flashes, Semi-flashes, and MLO's. (N. B. The plots of the MLO's and the Flashes track too closely in the interval from 15 to 28 min for this representation to discriminate.)

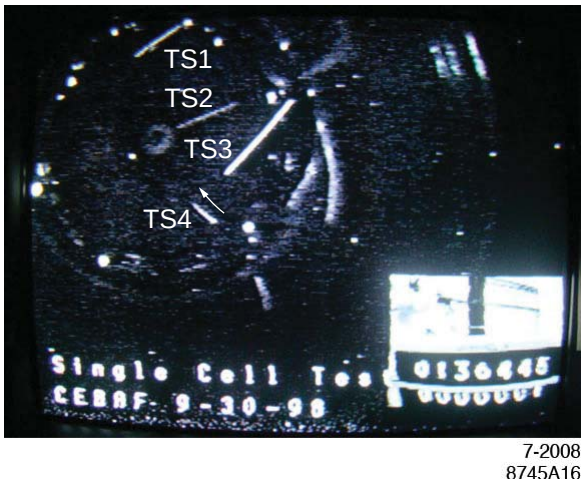

Figure 18. Frame 136445 (9 frames subsequent the semi-flash in Fig. 16), which contains a flurry of MLO's. Four separate MLO track segments are indicated, one of which is associated with Orbit 10 (TS4). (There are also a number of track reflections, as well as SPL's.)

5.7 MLO correlations with FoL's, a conceptual framework

In Ref. [1] it was observed that a "flash of light" (denoted by FoL in this paper) often appeared to precede the MLO events. In this section we subject all of the (Run 1) FoL's and MOL's to a statistical analysis to better reveal this correlation. The first conceptual step is to view the video data as a sequence of samples, where each video frame is a sample with only two possible results: "success," i. e., an observed event, or "failure," no event. Since we have two kinds of events (an FoL or an MOL), our video data actually generates two "independent" sample set sequences.

In these sequences, the number, *k*, of empty frames (i. e., failures) to achieve a single success is analogous to the waiting time in probability theory. In the theory, if the

samples are truly random (with a uniform success rate probability and uncorrelated), then the set of waiting time probabilities (indexed by k) is described by a geometric distribution [9]. It is important to note that from such a sample set one obtains a geometric distribution using any criterion to define the $k = 0$ start-sample in the search for a success as long as that criterion is independent of the location of that success [9]. For our analysis, it is also crucial to observe that such a sample set can be searched in either time direction. That is, a downstream search will give a waiting time distribution while an upstream search will give what might be called a precursor time distribution, and (assuming independent sample probabilities and start-sample locations) both of these will be geometric distributions described by the same parameters.

The theoretical geometric distribution has a structure analogous to the waiting time distributions derived from our experimental data; hence, it is a useful phenomenological representation of the data. One of the tools we shall use to compare data to theory is the method of least squares [10]. In view of the relatively small number of events and the large varability of experimental conditions during this run, there are some limits to the applicability of this method. However, this approach is still useful because we seek qualitative rather than quantitative results. (Also, the results of this method are more accessible than those of more sophisticated methods–such as maximum likelihood.)

The most important result from our waiting time analysis derives from a comparison of the upstream and downstream distributions obtained from the MLO and FoL data to appropriately constructed theoretical geometric distributions.

5.7.1 The geometric distribution, some theoretical details

For a given sample sequence, it is assumed that there are only two possible sampling outcomes: success or failure. For these samples, denoting the probability of success (failure) by p (q), we have

$$p + q = 1. \tag{1}$$

Stipulating that $0 < p, q < 1$, and that they are uniform and independent of time, the waiting time probability $f(k; 1, p)$ for exactly k failures to precede one success is given by

$$f(k; 1, p) = q^k p, \tag{2}$$

where $f(k; 1, p) < 1$ is a general term of a geometric distribution. This is a special case of the Pascal distribution, $f(k; r, p)$, which describes the waiting time to achieve r successes [9]. It is easy to show that the probabilities $f(k; 1, p)$ satisfy the normalization condition

$$\sum_{k=0}^{\infty} f(k;1,p) = 1. \tag{3}$$

The first moment of this distribution $\bar{k}$ characterizes the time scale of the distribution, where the unit of time is the video frame duration. Given the functional form of Eq. (2) it is straightforward, using Ref. [11], to calculate $\bar{k}(p)$:

$$\bar{k}(p) \equiv \sum_{k=0}^{\infty} k\, f(k;1,p) = \frac{q}{p}. \tag{4}$$

Thus, one finds that $p\bar{k}(p) \to 1$ as $p \to 0$.

We shall see that the span of the waiting time distributions derived from the data, as indexed by *k*, partitions into three regions: small, medium, and large. These regions will be analyzed in more detail below. To effect the comparison of data to theory, we bin the data (in bins of width n_b) and sum the theory over each bin. Using Eqs. (1 and 2) for the theory, for the K^{th} bin we write:

$$Bin_T(K; n_b, p) = A \sum_{k=Kn_b}^{(K+1)n_b-1} f(k;1,p) = Apq^{Kn_b} \sum_{j=0}^{n_b-1} q^j, \tag{5}$$

where the subscript $_T$ denotes theory, and *A* is a normalization factor; *K* = 0, 1, 2, ⋯, and n_b = 1, 2, 3, ⋯.

5.7.2 A χ^2 fit for the FoL waiting times (medium k region)

For this purpose, we computed the FoL waiting time distribution by tabulating the time (in frames) between FoL's:

$$\Delta F_{FoL_i} = F_{FoL_{(i+1)}} - (F_{FoL_i} + 1), \tag{6}$$

where *i* is the FoL index. (The the +1 in the second term dictates that flashes in two adjacent frames will have a waiting time index of *k* = 0.) Thus, our 130 FoL's yielded 129 waiting time entries. It is obvious that the magnitudes of the elements ΔF_{FoL} in this experimentally obtained FoL waiting time distribution are invariant with respect to time reversal. The analysis of this (simpler) FoL waiting time distribution will enable a better basis for understanding the exploration of the correlations between the FoL and MOL events.

The first step is to fit our (binned) experimental data to a theoretical waiting time distribution. In looking for the right bin size, we observe that if n_b is too small, there will be low occupancy (or even empty) data bins, and if n_b is too large we will lose sensitivity to the shape of the (experimental) geometric distribution. For the χ^2 fit we selected n_b = 100 as a suitable compromise. In Fig. 19, we have plotted the histogrammed FoL intervals out to ΔF_{FoL} = 2000 frames = 66.7 s. This histogram captures 117/129 data points, the remainder being in a long tail (out to a maximum ΔF_{FoL} = 30528 or ~17 min).

The number of useful bins for fitting purposes is limited by the natural reduction in occupancy number as *K* gets larger. For our fit, we chose the maximum to be *K* = 5 (i. e., out to 20 s). (Varying the maximum *K* by ±1 makes a modest quantitative but no qualitative difference to the χ^2 fit.) This truncation of the fit region also limits the skewing of the results by the events residing in the low *p* (i. e., large *k*) regions of the data. Thus, our expression for χ^2 is

$$\chi^2(p) = \sum_{K=0}^{5} \frac{[Bin_E(K;100) - Bin_T(K;100,p)]^2}{Bin_T(K;100,p)}. \tag{7}$$

Minimizing $\chi^2(p)$ with respect to *p*, yields $p = (5.0 \pm 0.7) \times 10^{-3}$ as the best (one parameter) fit. The normalization *A* was eliminated as a degree of freedom by requiring

that the integrated theoretical curve (out to 20 s) be normalized to be equal the number of events (89) in those first 6 bins. Thus, these 89 events comprise the medium *k* region of our data (and, as an aside, also include the small *k* region). In Fig. 19 we have included the plot of the best theoretical fit function ($p = 5.0\times10^{-3}$) along with the location of its $\bar{k}$ (= 199).

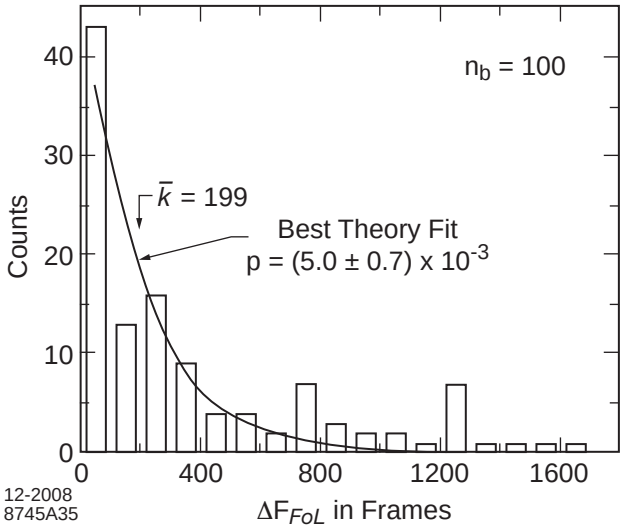

Figure 19. Using n_b = 100, histogrammed FoL intervals out to ΔF_{FoL} = 1800 frames plus a best χ^2 fit as described in the text. The location of $\bar{k}$ = 199 for that fit is indicated.

For $p = 5.0 \times 10^{-3}$, $A = 93.6$, which means that the (theoretically) expected number of events beyond $k = 599$ is 4.6. The actual number (129 – 89 = 40) of events in the data beyond $k = 599$ are generally associated with the regions of much lower p, and comprise the large k region, which we do not analyze further.

This best fit yields a $\chi^2 = 6.0 \Rightarrow 1.2$ per degree of freedom (dof), which is much better than one might expect since our data obviously depend upon a number of unknown parameters, deriving from both experimental conditions and the physics of the phenomena. It is interesting that this best fit value of p is twice that found above in the 11.6 min high rate period. This would seem to indicate some non-random bunching in the high rate FoL data.

5.7.3 The small k region

The bin size, $n_b = 100$, used in the above χ^2 fit obscures possible structure in the small k region. Explicit examination of this region (i. e., set $n_b = 1$) reveals that for $0 \le k \le 3$, there are no ΔF_{FoL} events. In contrast, the best fit curve indicates an expectation of 1.86 events in these first four bins. Taking 1.86 to be the mean value of a Poisson distribution [9], the fraction of comparable data sets with no events would be 15.6%. Thus, while this probability is low, it is certainly quite plausible that these first four bins could be empty through statistical variability alone. However, it is also likely that physics is a contributing cause: the flash events, as confirmed by data from later runs, quickly drain off all of the energy in the cavity, and the high cavity Q causes a several frame delay in the re-excitation of the cavity (see below). Presumably, the semi-flashes have a similar (but lesser) effect.

5.7.4 MLO correlations with FoL's

We can now use the above development as a conceptual framework to investigate the correlations between the timing of FoL's and MOL's. We shall do this by comparing the upstream or precursor time distribution to the standard downstream waiting time distribution, starting the upstream and downstream failure count at the very frame in which each MOL was tabulated. Each MOL, then, will generate two entries, one in each wing, in the final ±waiting time distribution. (We note that, as discussed in *Sec. 5.3*, the initial MLO does not actually have a precursor FoL, thus reducing by one the number of entries in the precursor distribution.) In either direction a success will be established at the frame which contains the first FoL; the coincidence (at Frame 28635) enters twice (once in each wing) as an event with $k = 0$. (Presumably, if we had adequate time resolution within a frame, we could assign this $k = 0$ event to the correct distribution.)

If the underlying physics of this ±distribution were governed by variables having truly random and time-invariant probabilities, the two wings would (within statistics) be geometric in form and mirror images of each other. (We remark that the presence of MOL flurries will augment the bin contents of the associated k values. To the extent that this effect introduces shape variations, the ability of a one parameter geometric distribution to represent the underlying phenomenology is impared.) On the other hand, the fact that the data streams for the FoL's and the MOL's separately do not satisfy ideal conditions of randomness with time independent probabilities should not introduce significant asymmetries between the upstream and downstream distributions. Thus, any asymmetry (beyond counting statistics) that is revealed in this FoL-MOL two-way correlation plot is evidence that the physics of these two phenomena are related.

Using $n_b = 100$, we have plotted in Fig. 20 the upstream and downstream wings of the waiting time distributions obtained by binning the tabulations of:

$$\Delta F^{(\pm)}_{(F-M)_i} = \pm(F_{FoL_{(i\pm1)}} - F_{MOL_i}), \tag{8}$$

where i is the index of the chronological union of the FoL and MOL events. The + (–) sign indicates the waiting (precursor) time distribution.

Following the FoL analysis above, we have done a χ^2 fit to the first 6 bins of the +wing of the FoL-MOL waiting time distribution. In Fig. 20 we include the best χ^2 fit to this wing of the distribution, which yields $p = (5.7 \pm 0.6)\times10^{-3}$, $\bar{k} = 174$, and $\chi^2 = 5.42$ or 1.08/dof. This fit value of p is somewhat higher than that for the source FoL distribution, but the difference is not statistically significant. It also is noteworthy that the value of χ^2/dof is again quite reasonable, indicating that the presence of the preceding MOL does not appear to have significantly distorted this wing of the FoL-MOL distribution.

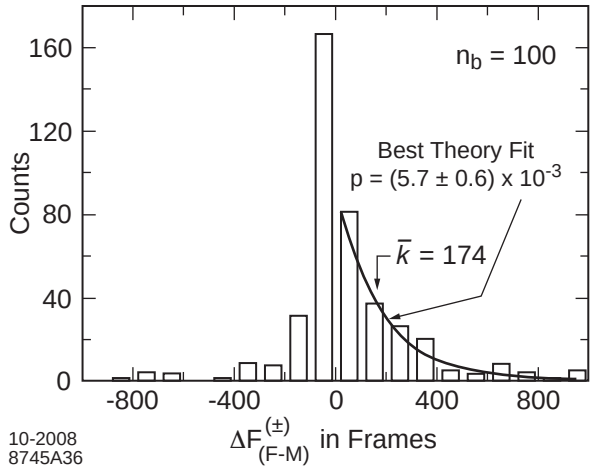

Figure 20. Using n_b = 100, a plot of the upstream and downstream wings of the distribution defined by Eq. (8), plus a best χ^2 fit to the positive wing of the distribution, with its associated $\bar{k}$ = 174 indicated.

In examining the precursor wing as displayed in Fig. 20, we see that there appears to be a significant increase in the success probability/frame (or equivalently a lower $\bar{k}$). Hence, for fitting purposes we have rebinned the data in this wing using n_b = 50 and made a χ^2 fit in the range $0 \le K^{(-)} \le 4$. The rebinned data and the best fit to this distribution, which are plotted in Fig. 21, yields $p = (19.4 \pm 1.4) \times 10^{-3}$, $\bar{k} = -51$, and $\chi^2 = 10.4$ or 2.6/dof. Several things are revealed by this result. First the much higher p indicates that indeed MOL's tend to follow FoL's, or said another way: FoL's appear to be a causal factor in the appearance of MOL's. Second, the associated value of $\bar{k}$, indicates that the characteristic time scale for the interval between FoL and MLP is one or two seconds. And third, the rather large value of χ^2/dof indicates a significant distortion of the putative waiting (i. e., precursor) time distribution by unknown physics processes. All of these results are indications of a fundamental asymmetry in the full ±distribution.

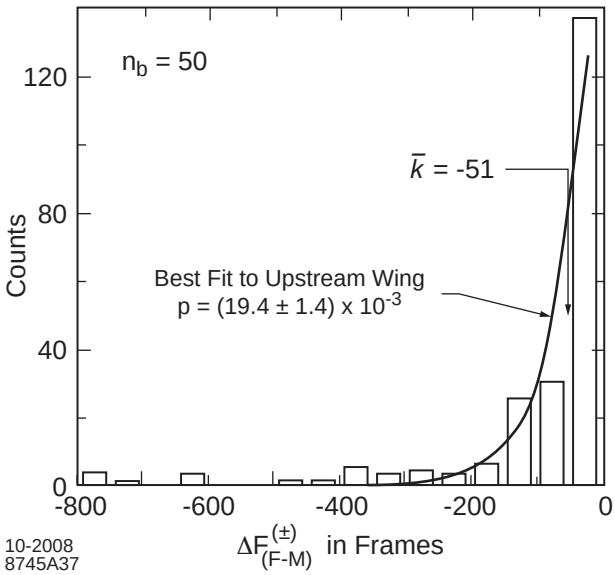

Figure 21. Rebinning of the upstream wing of Fig. 20 using n_b = 50. A best χ^2 fit to this distribution is included, with its associated $\bar{k}$ = – 51 indicated.

A quantitative indicator of this asymmetry can be written as the ratio:

$$\mathcal{A}(n_b) = \frac{N^{(-)}(n_b) - N^{(+)}(n_b)}{N^{(-)}(n_b) + N^{(+)}(n_b)}, \tag{9}$$

where $N^{(\pm)}(n_b)$ are the counts in the $K^{(\pm)} = 0$ bin (of bin size n_b) in the distribution. The standard deviation for $\mathcal{A}(n_b)$ is given by the equation:

$$\sigma_{\mathcal{A}}(n_b) = 2\sqrt{\frac{N^{(-)}(n_b)N^{(+)}(n_b)}{[N^{(-)}(n_b) + N^{(+)}(n_b)]^3}}\ . \tag{10}$$

The number of standard deviations, i. e., ratio $\mathcal{R} = \mathcal{A} / \sigma_{\mathcal{A}}$, gives an indication of the statistical distance from symmetry of the wings of our ±waiting time distribution. In Table III we have listed these quantities for several values of n_b. The values of $\mathcal{R}$ clearly demonstrate that the observed experimental asymmetry is well beyond any reasonable statistical fluctuation.

It is interesting that the asymmetry is maximum for $n_b = 20$, dropping to a value consistent with $\mathcal{A} = 0$ for $n_b = 3$. (Of course, as n_b becomes very large, the initial bin in each direction will encompass the entire wing, driving $\mathcal{A} \to 0$.) To reveal possible structure for small k, we plot in Fig. 22 the ±waiting time distribution for $n_b = 3$. Here we see that the peak bin in the precursor distribution is at $K^{(-)} = 3$, putting the peak at $k \sim 7$; this peak has a FWHM of $\Delta k \sim 6$. It is interesting to compare these general results to the data on the orbital MLO's (which, of course, comprise a subset of the distributions in Figs. 21 and 22). In Column **B** of Table IV we see that the FoL-MOL interval ranges from 3 to 33 frames with a mean of 12.7.

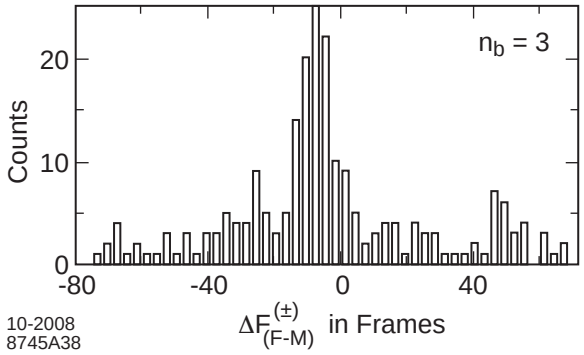

Figure 22. Plot of the two wings of Fig. 20 using $n_b = 3$.

As a point of further insight, we see that this plot is consistent with the notion that at small k the value of $p^{(-)}$ tends toward that of $p^{(+)}$. This indicates that whatever the causal relationship between an FoL and the subsequent MOL, it appears to entail a certain nonzero time interval consistent with column B of Table 4. (Is there an MOL formation time?)

5.8 Orbits

In addition to tracks extending over only a few frames (e.g., Fig. 7), MLO's orbiting for extended periods were observed. Thirteen such orbits and some of their salient features are listed in Table IV. A common feature exhibited in most of these orbits (at least in some frames) is an elliptical path (e. g., Fig. 1). It was shown in Ref. [13] that a small conducting (or dielectric) particle moving about in a cylindrically symmetric resonant cavity with an excited TM_{010} mode will be residing in a two dimensional harmonic oscillator potential well symmetric about the cavity axis. (Ref. [13] calls this the Small Particle Model or SPM; see *Sec. 8.4.1,* below.) The general solution for the radial portion of the orbit in such a well is an elliptical path. In this analysis, the center of the ellipse is, of course, located on the axis of the cavity. Since the camera is looking along the *z*-axis, the (video patterns of the) data can be viewed as a projection of the radial component of the orbit onto the equatorial plane of the cavity. While the details of the *z*-component of the orbit (and the forces that govern it) are not well known, one can invoke a symmetry argument that (for the long-lived orbits) the orbit centroid must be located at the highest symmetry point of the cavity, that is, in the equatorial plane at the center of the cavity. (Of course, fluctuations of the orbit centroid about the cavity center are possible.) And when one includes information available from the reflections of the orbital luminosity (see below), it appears that this conjecture is confirmed. That is, the orbits are centered on the cavity axis between the irises; they are not inside the beamtubes nor some kind of luminous activity on the optical windows or end flanges.

Often the initial track segments of the orbits were characterized by low luminosity. In fact, sometimes portions of some of these initial track segments fell below the threshold for observable luminosity for our video system. We have confidence, however, that the track portions not seen were in fact there because of the periodicity and consistent sequencing (from frame to frame) of the orbits themselves. With respect to track luminosity, we also note that in many cases the brightest portion of the orbital track was seen to be at or near the ends of the major axis. One cause for this, of course, is that the linear velocity is (by conservation of energy expected to be) reduced for greater displacements from the cavity axis. But there could be other effects as well.

The observed orbital frequencies ranged from 5 to 80 Hz. At the low frequency end are Orbits 1 and 3. The ends of the major axis of each of these orbits resided in the cavity volume at a radius out of view of the camera. For tracks in the equatorial plane, the occultation radius due to the near iris is estimated to be ~4.5 cm. At the high end of orbital frequency is the orbit displayed in Fig. 1 (from Orbit 4), which was shown to have a frequency of 80 Hz [13]. Similar to the orbit of Fig. 1, many of these orbits exhibit paths that are to first order nearly perfect ellipses. In general, however, the trace of the elliptical path never remains fixed in space. The simplest path variation is that the orbits precess while maintaining their (quasi) elliptical shape.

Two beautiful examples of precessing elliptical orbits were observed in the 5-cell data (Orbits 11 and 12, as described in Table IV). These orbiting MLO's appeared right after a bright flash (which saturated all of the pixels in the video camera), and appeared to be located in the center cell of the 5-cell string. Each of this pair of long-lived orbits exhibited a fairly steady precession rate (in opposite directions) lasting over their full lifetime of >300 frames. The nearly perfect elliptical shape of these two orbits persisted throughout their lifetime.

More complicated shape and orientation changes were also observed. For example, Orbit 2 tended to maintain an elliptical shape, but its eccentricity and orientation varied continuously and smoothly. It is interesting to observe that during the course of these orbit contortions, the (projection of the) orbit never exhibited an eccentricity $\varepsilon = 1$, i. e., a straight line. On the other hand, as recorded in Table IV, both Orbit 4 and Orbit 7, in some frames, exhibited the $\varepsilon = 1$ shape. An example of this from Orbit 4 is given in Fig. 23. In general, however, Orbit 4, for the most part, tended to be quite erratic, probably due to the influence of other objects (tracks) sporadically crossing the orbit region during the 39 frame sequence. Fig. 24 shows Frame 53858 from this sequence containing an example of a distorted orbit and a passing track segment that is due to a separate, non-orbiting MLO. One supposes that the flash that (evidently) terminated Orbit 4 also initiated Orbit 5. Orbit 5 remained fairly stable in shape, but it was not an ellipse, which is characterized by two apoaxial extrema. Rather, it had three apoaxial extrema, and hence might be described as quasi-triangular. This non-elliptical shape again indicates that the force associated with the harmonic oscillator potential well is not the only one acting on the orbiting MLO's (Re other forces, see *Sec. 5.10*, below.).

7-2008
8745A17

Figure 23. A linear ellipse seen in Frame 53862 of Orbit 4.

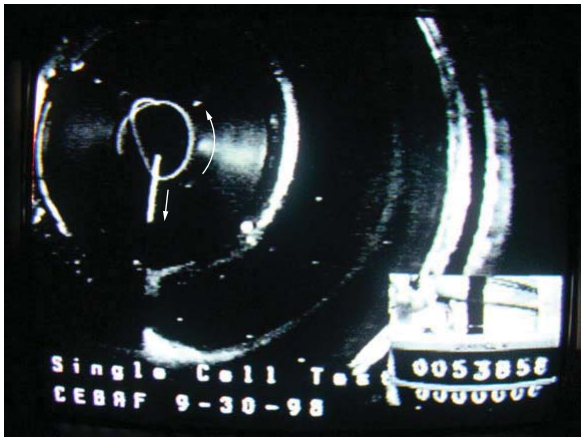

2-2009
8745A18

Figure 24. Distorted track segment of Orbit 4 (in Frame 53858) with an additional passing track. Arrows indicate the direction of travel.

As indicated in Table IV (for the orbits in Run 1 that are slow enough and stable enough to be properly measured), there is a one-to-one correlation between the orbital direction and the precession direction. Note that although the orbit and precession directions are listed for Orbits 7b and 10 as "both," the above one-to-one correlation still obtained, with both directions switching at the same time (at the $\varepsilon = 1$ frame). On the other hand, in both of the long-lived orbits of Run 2, these two characteristics of the orbital motion are anticorrelated. (For Orbit 13, the orbit duration was too short and the simultaneous presence of other two orbits made determining its orbital direction too problematical.)

This progression of orbital distortions culminates in what was described in Ref. [1] as an "irregular-shaped closed filament," an example of which was shown there as Fig. 2b and which is reproduced here in Fig. 25. In Fig. 25a, we reproduce the video field as it was recorded in the computer. In order to enhance the visibility of the track, we uniformly increased the brightness and the contrast of this image (using Adobe Photoshop). The result, shown in Fig. 25b, shows a significantly improved visibility of the track.

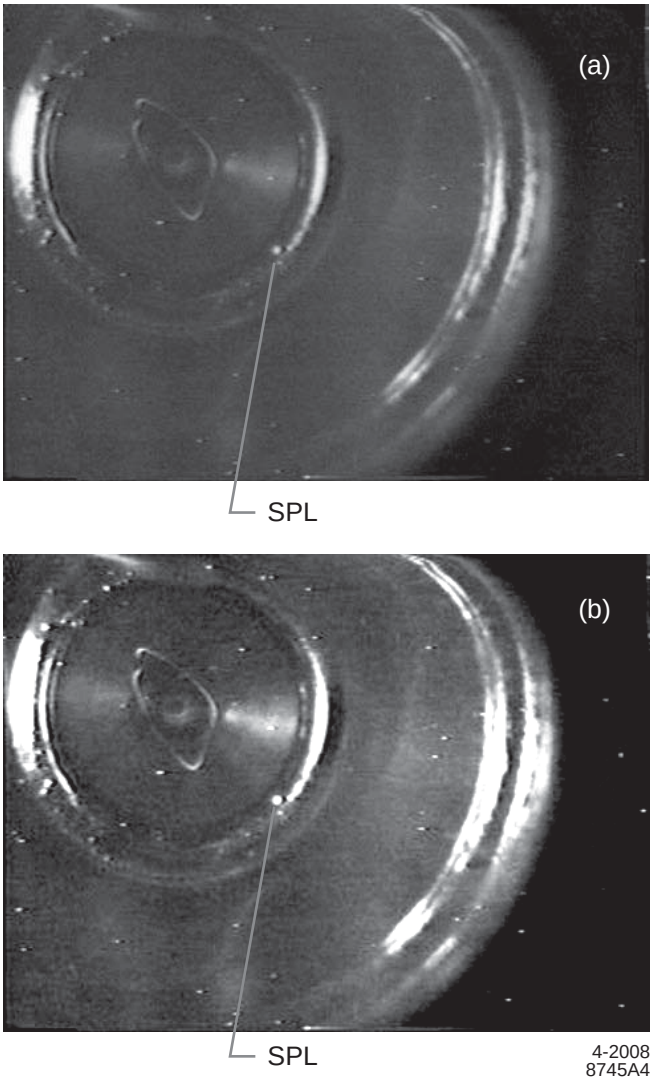

Figure 25. Irregular-shaped closed orbit. This image has been enhanced, as described in the text. The SPL visible in Fig. 1 is indicated.

This figure is a video field taken from Orbit 9. This orbit, perhaps perturbed by a mild flash at Frame 64811, then morphed into an orbit of large aspect ratio that exhibited a rocking motion, i. e., an oscillating precession. Its rocking rate was about 32 frames/cycle or ~1 Hz, and the full rocking motion spanned an angle of ~ 100°. The observed orbital tracks (before and after Frame 64811) were such that it was not possible to unambiguously determine the orbital frequency (although Fig. 25b implies that it is ~60 Hz; it appears to execute a nearly full loop in the frame--1/60th of a second/field) or the direction of orbital rotation. Orbit 10, another rocking orbit, was quite regular in its motion. (Its orbiting and precession frequencies are given in Table IV.) Though it only executes ¾ of a rocking cycle in its 15 s duration, one easily estimates its rocking rate as 0.05 Hz; its full span in azimuthal angle was measured to be ~35°.

5.9 Reflections in the walls

The interior of a processed niobium cavity has a rather smooth, mirror-like surface. Frequently reflections of the region of the track luminosity can be clearly seen in the cavity walls. There are two possible surfaces that have a geometry that can yield reflections of the interior tracks that are visible to the CCD camera: 1) the beamtube and 2) the interior of the cavity near the far iris. Fig. 26 gives a schematic depiction of these two paths. Examples of reflections in the beamtube are more numerous because it affords the larger solid angle. An excellent example of a beamtube reflection is seen in the single track segment shown in Fig. 27 (which was given as Fig. 2c in Ref. [1]). As one would expect, surface variations in the wall cause the track reflection to appear more diffuse and irregular than the directly viewed track. These differences enable one to distinguish track from reflection.

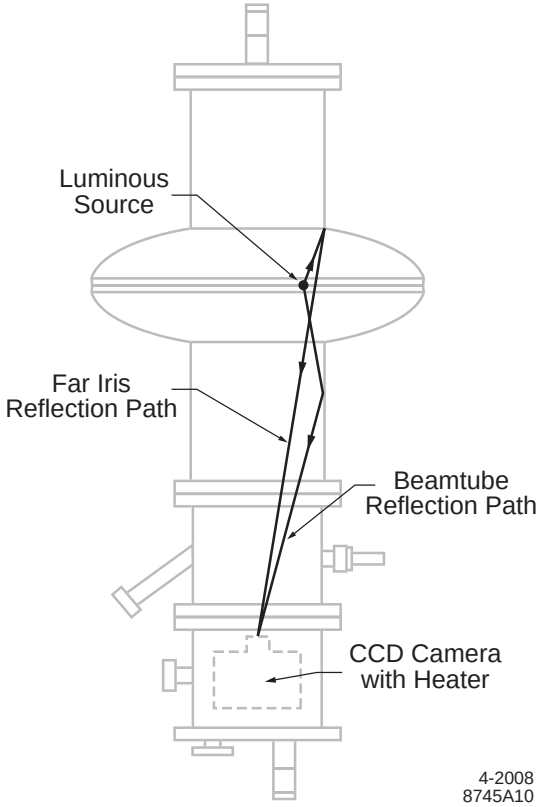

Figure 26. Depiction of the two possible optical reflection paths in niobium cavity walls. The luminous source is assumed to lie in the equatorial plane of the cavity.

As noted, Fig. 27 also exhibits a second (partial) reflection from the far iris region of the cavity interior. We have found several instances that more clearly exhibit simultaneous track reflections following both reflecting paths. We give an example of this (from Frame 52523) in Fig. 28. Of course, when the relevant optical paths are available throughout the track segment, segmented tracks also lead to segmented reflections that, as one would expect from geometry and the cylindrical symmetry of the cavity, subtend the same azimuthal angle from the cavity axis. To assist in visualizing this effect, radial lines are drawn into Fig. 28 to guide the eye.

Reflections in the walls, then, afford a useful quasi-stereo view of the track and indicate the geometric relationship of the MLO to the cavity walls. It is most important to observe that these reflections show that long-lived orbits (discussed above) can and do exist without any wall contact. Also, as discussed below, they assist in the analysis of specific wall collision events.

As an example of the usefulness of these reflections, we note that the event illustrated in Fig. 27, appears to be an example of a wall collision event. However, a close examination of the nexus of the track and its reflection indicates that they do not, in fact, join at a point. This fact is revealed by a close-up of this region as shown in Fig. 29. Further clarification derives from an examination of the frames prior and subsequent to that in Fig. 27. From this we conclude that the MLO was initially headed across the beam region at a radius less than that of the beamtube, and it then moved into the resonant cavity volume out of sight of the camera when its radius exceeded the occultation radius. Unlike the tracks of Orbits 1, 3, and 10, this track did not reappear.

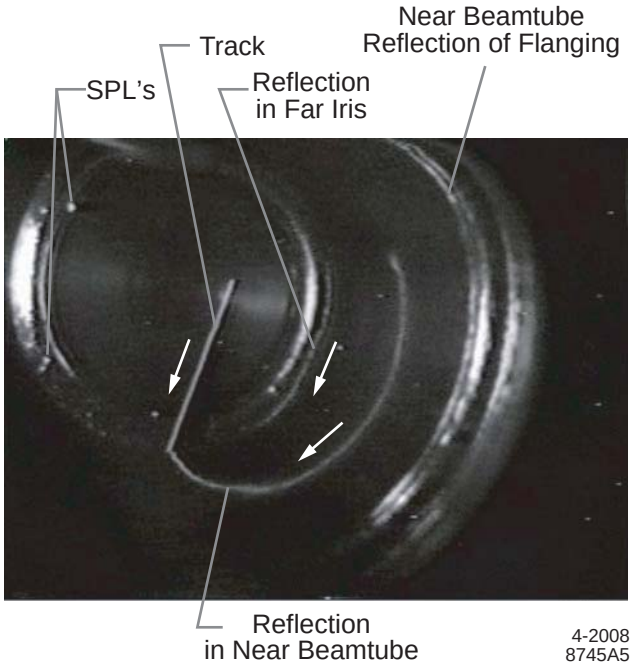

Figure 27. A track and its reflections in the beamtube, as indicated. Arrows indicate the direction of motion. The reflections from the near beamtube and spoolpiece flanges are due to the externally introduced light.

7-2008
8745A19

Figure 28. Track segment with a double reflection in Frame 52523. The track segment **T** is moving from right to left. **RFI** indicates the reflection in the far iris, and **RBT** indicates the reflection in the beam tube.

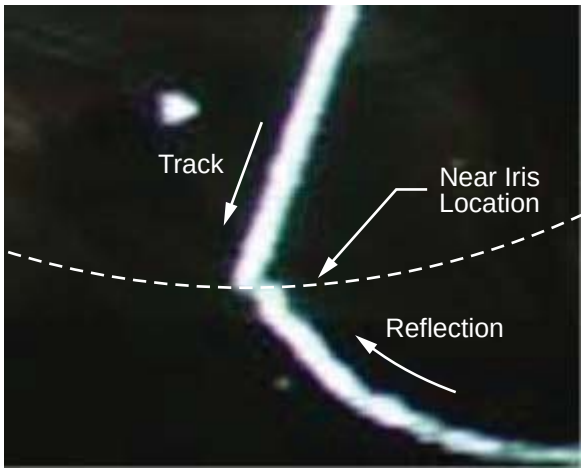

7-2008
8745A21

Figure 29. Blow-up of the track-reflection nexus region of Fig. 27, which indicates a lack of connection between track and reflection. (Compare this nexus region to that of the wall-bounce event shown in Fig. 30.) Arrows indicate the direction of track (and reflection) motion. The dashed arc indicates the location of the near iris.

5.10 Interactions

As argued above, the orbiting MLO's reside in a cylindrically symmetric two-dimensional harmonic oscillator potential well deriving from the RF cavity fields. As noted, elliptical orbits about the cavity axis are general solutions for objects moving in such a well. Hence, the observed long-lived quasi-elliptical orbits (in particular, Orbits 11 and 12) are prima facie evidence that such a well exists, that the MLO's carry a certain mass, and that to lowest order the force associated with this potential well defines the orbital paths. However, the various paths that exhibit more complicated curvature (e. g., the distorted orbit of Fig. 24, the irregular shaped orbit of Fig. 25, the quasi-triangular orbit, the wall-bounce events, and the mid-vacuum collision event discussed below) clearly indicate that the MLO's are also subject to other forces.

5.10.1 Wall-bounce events

There are clear examples in which MLO's collided with the cavity walls and bounced back into the vacuum space. The recognition of these events is significantly aided by the accompanying track reflections. While none of these events are associated with MLO's in orbit, we believe that is reasonable to assume that these wall-bounce MLO's are intrinsically of the same character as those in orbit. In the data from Run 1, at least 9 such events were identified. Fig. 30 shows what might be called a gold plated wall-bounce event because both the entering and exiting tracks with their respective reflections all meet at the collision point in a single field of a single frame, unambiguously defining the wall contact point. (Not shown in Fig. 30 are the natural extensions of the entering and exiting tracks, with reflections, which are found in preceding and subsequent frames.)

The wall-bounce events raise important questions with regard to a proper description of the MLO as a discrete self-coherent object. For example, if, as is argued in Ref. [13], its density is too small to be a solid object, how does it survive a relatively violent wall collision event? One theoretical possibility is discussed further in *Sec. 9.3.*

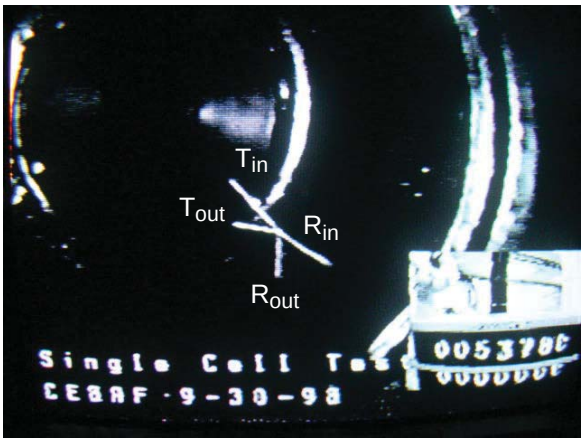

7-2008
8745A24

Figure 30. Wall-bounce event (in Frame 53780) in which the MLO luminosity is maintained throughout the collision process. Subscripts indicate the direction of track (**T**) and reflection (**R**) motion.

As an aside, it should be remarked here that, while the MLO's in orbit appear to be confined to the cavity volume between the irises, some of the wall-bounce MLO's were observed to enter into the beamtubes: as confirmed by reflections, one was clearly seen to enter the far beamtube and one into the near beamtube. It is interesting to note that the luminosity of the MLO entering the far beamtube appeared to diminish as it moved farther into the beamtube. (Of course, it is moving into a region of reduced field strength.) Unfortunately, the MLO moving into the near beamtube became significantly out of focus and an evaluation of its change in luminosity wasn't feasible.

5.10.2 Long-range mutual interactions

The perturbations seen in Orbit 4 are excellent examples of a possible long-range mutual MLO-MLO interaction. In Fig. 24, for example, if we consider the ratio of the track

length prior to the track intersection point to the total length of that track segment, we obtain 0.23 for the passing track and 0.33 for the orbiting track. This implies that the two MLO's passed in close proximity in space and time at the intersection point, but probably did not contact each other. But contact or not, it is certainly reasonable to conclude that the distinct change in direction and curvature of the orbiting track subsequent to the track intersection point was due to an MLO-MLO interaction. A second example is the "irregular-shaped closed filament," reproduced above in Fig. 25. While there is no evidence here for other MLO's, one interpretation of this figure is that there are two (or more) MLO's in simultaneous orbit and that in addition to being in a two-dimensional harmonic oscillator potential well, they are also experiencing a mutual interaction force. The postulated mutual interaction, then, would account for the transformation of a simple elliptical orbit into the observed irregular shaped orbit. Unfortunately, the possible presence of two (or more) MLO's in simultaneous orbit puts further analysis of these tracks beyond our present capabilities. Except to say that we can observe that these examples indicate that the range of the putative MLO-MLO interaction evidently can exceed the apparent object size (as defined by its region of luminosity).

5.10.3 Short-range interaction

It is particularly interesting to include here an example of a short-range interaction: Fig. 31a, which is taken from Orbit 7, exhibits a sharp kink (in a single field of Frame 56808) in an otherwise smooth path. Examination of the wall reflection of the path at the location of the kink confirms that it is in the vacuum space away from the cavity walls. Fig. 31b depicts the orbit shape before and after the kink. Before the kink it was a well-formed ellipse of $\varepsilon = 0.99$, and after the kink the orbit was a well-formed ellipse of $\varepsilon = 0.95$. As can be seen from the figures, at the kink the track was deflected by an angle of 40°, and the major axis of the orbital ellipse was deflected by an angle of 28°. The track deflection of 40° indicates that the magnitude of the momentum transfer is comparable to that of the initial momentum of the orbiting MLO at the kink. That the orbits before and after the kink are of comparable size indicates that the magnitude of the momentum after the kink is also comparable to that before. Hence, we believe that the most probable interpretation of this kink is an abrupt ($\Delta t < 1$ ms) momentum transfer $\Delta \boldsymbol{p}$ between some unseen object in the vacuum space and the orbiting MLO. (Bold faced variables indicate 3-vectors.) There are two obvious candidates for the unseen object: 1) a passing (MLO-like) object with parameters that render it below the threshold of visibility (evidence for this possibility was given above), or 2) a small fleck of ordinary material (niobium?) that is too small to heat up to a visible level of incandescence in the ambient RF field. (We remark that efforts to enhance this kink-image, as was done for the image in Fig. 25, gave no indication of a possible sub-visible track colliding with the MLO in orbit.) Further analysis of this mid-vacuum event is beyond the scope of this paper.

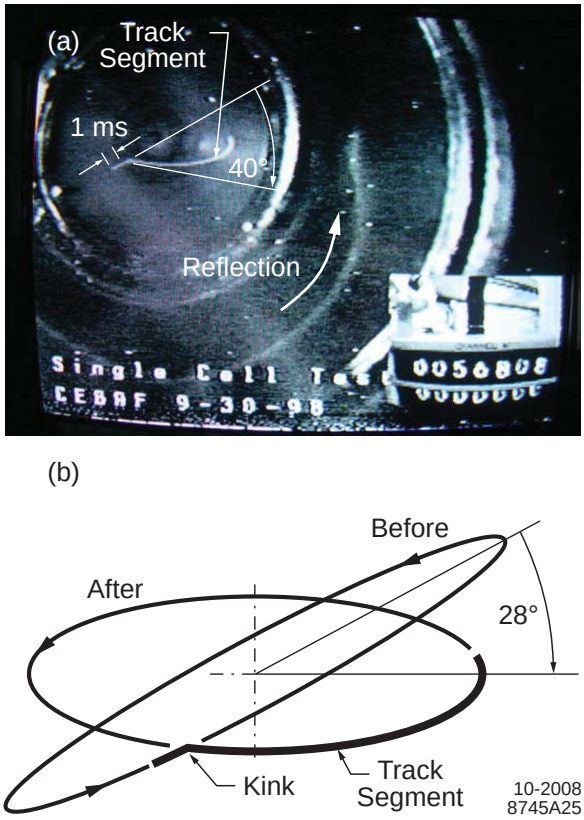

Figure 31. a. Track in Orbit 7 that exhibits an abrupt deflection or kink (in Frame 56808). An estimated path length of 1 ms duration and the angle of track deflection (40°) are indicated. b. Depiction (enlarged by a factor of 3.7) of the orbit ellipses before and after the mid-vacuum kink shown in Fig. 31a. The track segment containing the kink is drawn in bold. The location of the kink and the angle of reorientation of the major axis of the orbital ellipse (28°) are shown.

5.11 Modes of track demise

In the first two runs, we have observed three modes of track demise: 1) flash-induced, 2) losing luminosity, and 3) moving out of sight.

It has already been noted in Table IV that the terminus of several orbital sequences was coincident with a flash. This observation is consistent with the assumption that the (radial) stability of the orbit is a consequence of the electromagnetically generated two-dimensional harmonic oscillator potential well (SPM model of Ref. [13]): the flash drains all of the energy from the cavity, and (as we measured in Run 7, discussed below) it takes from 70 to 200 ms to regain full excitation in the cavity. (Varying conditions in the cavity cause a variation in the cavity *Q*, an observation already reported in Ref. [1], as well as elsewhere.) In this analysis, a flash (or a quench) eliminates the potential well that enables the orbit and hence terminates the orbit.

Examples of 2) are found in Orbits 11 and 12, which ended when the track luminosity faded, leaving a possible uncertainty of a few frames in the actual orbit duration. Orbits 1 and 3 were of low luminosity with their ends beyond the occultation radius. In these cases, the precise mode of demise could not be clearly established, but either 2) or 3) appears plausible. As another example of mode 3), the track in Fig. 27 vanished when (after?) it moved beyond the occultation radius (defined by the location of the near iris).

6. Additional runs

As mentioned above, we report the results of seven additional tests or experimental runs, Runs 3 through 9 all at TJNAF, that were undertaken in order to try to determine the conditions that are conducive to the formation of the cavity lights phenomena. For these runs, as discussed below, there were some modifications to the experimental configuration and additional instrumentation was incorporated.

6.1 Cavities

Runs 3 through 6 were performed with a new single-cell CEBAF cavity (Ser. P4-1311) obtained for the purpose of these investigations. (By the time this new series of runs was initiated, the original single-cell cavity was being used for a different set of experiments and was temporarily unavailable.) Runs 7 and 8 had both this new cavity and the original cavity mounted side by side in the same test dewar. The purpose of using two cavities was to double the possibilities for obtaining data in a single cool-down with liquid He. A second CCD camera with its evacuated enclosure was employed for the second cavity.

In Runs 7 and 8 each cavity had separate RF coaxial connections through the main He dewar flange, but only one cavity at a time could be excited with RF or monitored by the DAQ, described below. In Runs 7, 8, and 9 we inserted a 10 db directional coupler (with a crystal detector) into the cavity transmitted power line (which feeds the RF power control console) to obtain a transmitted power signal for the DAQ. In Runs 8 and 9, a high power 20 db bidirectional RF coupler[5] (also with crystal detectors) was employed to enable the DAQ to monitor the incident power to and the reflected power from the cavity.

Because of the experimental complications associated with the two-cavity test configuration, we elected to go back to the single cavity configuration for Run 9, for which we used the new cavity, P4-1311, as well as the bidirectional RF coupler.

6.2 Additional instrumentation

6.2.1 Magnetometers

For Runs 3 through 8, a single-axis fluxgate magnetometer[6] (FGM) was configured to operate in the 2 K environment. This configuration was effected by enclosing the fluxgate probe in an evacuated cylindrical stainless steel "anti-cryostat" (OD = 2.5") which had an internal heater to maintain the probe temperature at ~300 K. During the runs, the probe heater had to be turned off because the magnetic field from the current to the heating element dominated the magnetic data. The magnetometer had a flat sensitivity of $<10^{-5}$ G from dc to 200 Hz. The vacuum insulation of the probe was such that the probe temperature drift with the heater off was –19 °C/h. Thus, the heater could be turned off at the beginning of the run and the probe comfortably remained within its specified operating range (down to –40 °C) for the duration of the run (~1 hr). The probe wires (two shielded twisted pair), the (two) heater power wires, and the (four) temperature sensing wires were brought out through the instrumentation vacuum line, eliminating the need for cryogenic feed through connectors.

[5] NARDA 20 db bidirectional coupler.

[6] MEDA μMag.

The active element of the probe was situated in the equatorial plane of the cavity as close as possible to the exterior cavity wall (~3 cm) and was oriented to measure the ***B*** component along a radius extending out along a perpendicular from the cavity axis. For Runs 7 and 8 the probe was situated directly between the two cavities, again measuring essentially with equal sensitivity the radial component of the ***B*** field from either cavity.

In order to improve our capability to measure magnetic fields, we acquired a 3-axis FGM with a cryogenic probe[7], which is designed to operate at liquid helium temperature, and which has a noise (specification) level of 10^{-6} G/√Hz and a flat frequency response from dc to 250 Hz. The cryogenic head is much smaller than our anti-cryostat (discussed above), and permits more flexibility in probe placement. And measuring the three vector components of the magnetic field gives a more complete picture. This magnetometer was used in Run 9, where it was mounted as closely as possible to the lower cavity flange, which location is optimum for measuring the magnetic fields coming from the interior of the cavity. (A location near the upper flange would be equivalent.)

It is appropriate to mention here that in order to achieve a sensitivity to smaller magnetic fields, we also initiated the development of a prototype SQUID magnetometer. For this purpose we used an RF SQUID that became available through the upgrade of a commercially available rock magnetometer. (The upgrade involved replacing the original RF SQUID in the rock magnetometer with a DC SQUID). However, the (point contact) RF SQUID that had been made available to us could not operate in the 2 K environment required for proper cavity operation. And our attempts to thermally stabilize it at 4 K in this 2 K environment were not satisfactory. (And we decided that at this juncture it would not be prudent to change our cavity operating temperature to 4 K.)

6.2.2 Helmholtz coils

For Run 3 et seq., two pair of Helmholtz coils (with 5 turns on each coil) were mounted on the flanges of the cavity to inject a magnetic field into the center of the cavity. The axis of the Helmholtz coils intersected the cavity axis at right angles. Thus, the field generated by these coils was across the face of each flange. There was one coil pair mounted on the upper flange and one pair on the lower flange such that their injected fields would add in the equatorial plane at the center of the cavity. A calculation for such a field injection into the center of the cavity gave 3.6×10^{-5} as the ratio of the transverse field at the center of the cavity to that of the Helmholtz coils across the face of the flange. The purpose of these coils was to see if injecting a small magnetic field into the cavity volume would perturb the MLO's.

6.2.3 Photomultiplier tube (PMT)

It is obviously desirable to be able to continuously monitor the light intensity in the interior of the cavity. Data from such a monitor would also be useful to correlate with the video data. To effect this result, one end of a bundle of plastic fibers (each ~ 2 mm in diameter and covered with a thin opaque plastic tube) was abutted to a small sapphire viewport adjacent to the RF input coupler on the upper cavity flange. (This is an additional feature included in Runs 3 through 9. Hence, it is not indicated in Fig. 2, which is relevant to Run 1.) This bundle, which is reasonably flexible, was then brought

[7] Applied Physics 3-Axis Fluxgate Magnetometer, Model 520.

out of the helium dewar through an epoxy seal in a 2¾" conflat flange, and its other end was placed where it would illuminate the photocathode of a (side-on type) PMT[8]. This is the same bundle that was used to illuminate the interior of the cavities in Runs 1 and 2. In its new location it was still used before the run (by transporting light into the cavity) to verify the operation of the CCD camera and to furnish reference points for the cavity interior. In Runs 3 and later there was no externally applied cavity illumination during the data taking phase.

In Runs 7 and 8, the fiber bundle was split into two smaller bundles inside the dewar, one for each cavity. In this way it was possible to obtain a light signal from either of the two cavities when under test.

The configuration of the PMT and its housing is depicted in Fig. 32. (The PMT assembly is a modified JLAB arc detector.) Using the test LED in this configuration, it was determined that the response time constant of the PMT and circuitry is $\ll 1$ μs, which is negligible with respect to the flash duration. The LED light pulse can also test the PMT trigger for the DAQ system. In addition, the LED can furnish a timed light pulse through a fiber to the optical spectrometer, which enables pre-run testing of the timing, buffering, and spectral analysis of the optical spectrometer.

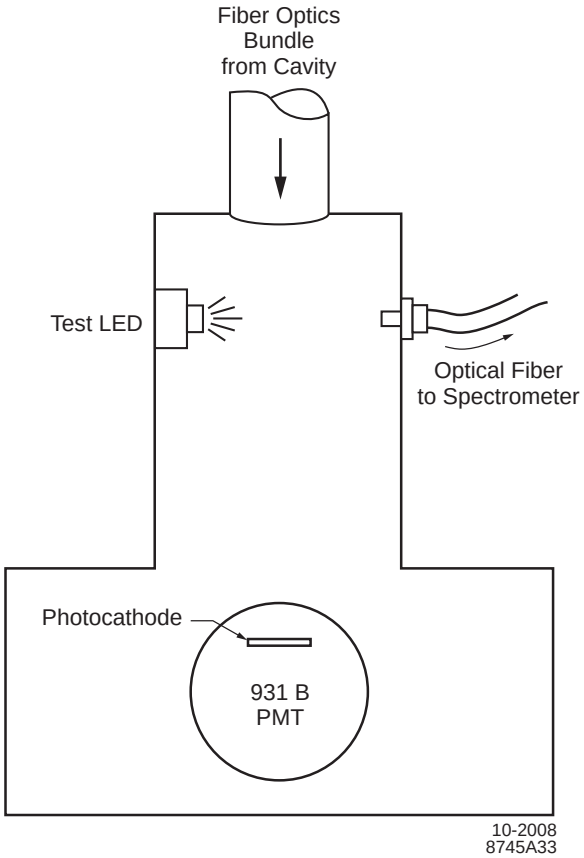

Figure 32. Schematic depiction of PMT and PMT housing (not to scale). Note the placement of the LED (light emitting diode) and the optical fiber port. Light from both the cavity fiber optic bundle and the LED illuminate the PMT photocathode. For timing tests, this geometry also enables the optical fiber to the spectrometer and the PMT to simultaneously capture light from the LED.

[8] Hamamatsu type 931B.

6.2.4 Optical spectrometer

In Run 7 et seq., one of the plastic fibers in the bundle described above (actually one fiber for each cavity, as appropriate) was split away from the bundle to the PMT and fed to an optical spectrometer[9]. While it appears quite possible to obtain a spectrum of the light associated with the flash, it is not clear that there will be sufficient light to obtain a spectrum from the other cavity lights phenomena. The range of the spectrometer analysis (for > 30% efficiency) is from 350 to 850 nm (grating #3). (We chose to collect spectra in the visible region to match the nominal range of the video camera.) A 50 μm entrance slit was chosen as a compromise between light collection and resolution. The spectrometer integration time can be set by the operator. The flagging of spectrometer data in the DAQ was set up to be triggered by a PMT pulse exceeding a threshold selected by the operator. (The optical spectrometer does not have an electronic trigger-to-read feature.) In this regard, it is of interest to note that we used the optical spectrometer, as controlled by the LabVIEW program, to record a test spectrum of the LED in the PMT assembly, which is a relatively narrow line with a peak at 575 nm. This step, in which the LED also triggered the PMT, confirmed that if there is sufficient light reaching the spectrometer, we can obtain and record an analyzed spectrum (See *Sec. 6.4.*).

6.3 Video/audio configurations

For Runs 3 through 7, the time waveform outputs of the PMT and the FGM were displayed on a free running dual trace digital scope[10], which was viewed by a second video camera. The time base of the scope was set at 20 ms/div, which led to a 200 ms display of the two waveforms. At this setting we measured 162 ms dead time between the sweeps for data collection or, equivalently, a 55% live time. (A 10 ms/div setting lead to a measured 44% live time.) Of course, the scope display is actually continuous. That is, it continues to display the last waveform while it is collecting and processing the data for the next waveform display. When the next data set is ready, the scope makes a transition to the next data display (which takes about one video frame). By using two PIP video mixers[11], it was possible to record on a single VHS tape the output of the two video cameras as well as (a portion of) the video display of the 1.5 GHz RF power control console. This two-camera video arrangement was used for Runs 3 through 7, and is shown as a component in the block diagram (Fig. 33) for the DAQ system discussed below.

A two channel audio system was set up to enable experimenters at two locations to be in voice communication. The locations were: 1) the computer control station for the RF cavity power and 2) the experimental data collection station. For Runs 3 through 6 the latter location was at the cryogenic test dewar in the VTA, and for Runs 7, 8, and 9 it was at the location of the computer monitor for the DAQ. For assistance in the data analysis, the two audio channels were (individually) recorded on the two stereo channels of the VHS data tape.

In Runs 1 through 9 we displayed on a video monitor at location 2) the video signal that was being recorded on the VHS data tape. For Runs 3 through 7 this display was

[9] Ocean Optics USB2000.

[10] LeCroy 9400A Dual 175 MHz Digital Scope.

[11] Kramer Electronics, Inc., Model PIP-200.

processed through two the PIP video units, as described above. In Runs 7, 8, and 9 we also fed the video signal (without PIP processing) from the (appropriate) camera in the dewar to a monitor at the RF control station at location 1).

The data derived from Runs 3 through 6 were modest in importance, and no difficulties with the PIP system were apparent. However, as will be seen from the discussion below, Run 7 generated data of considerable significance. It was in the course of the analysis of this data that the deficiencies of the PIP video system we were using became apparent. In reviewing the data on the VHS tape from Run 7, we realized that a certain amount of low-level video information was lost as a result of the PIP processing chain and the reduction in size of the cavity display. In particular, toward the end of Run 7, there was considerable general illumination in the cavity (due to some sort of internal discharge) and at the same time the MLO's appeared to be less luminous. As a consequence, we lost visibility of the MLO's when viewing them using the recorded data, although we had, in fact, been able to observe them (though with some difficulty) during this latter portion of the run on the full-scale real time video display. (The auto-iris of the CCD camera as well as the putative ruby fluorescence in the camera viewport may have contributed to this problem.) In addition, our analysis of the video data from Run 7 revealed another unanticipated problem with the PIP video mixers. We discovered that our PIP mixer arrangement discarded one of the fields from the PIP insert of the cavity camera video, filling out the interlaced frame of the insert by recording the other field twice. Thus, a segmented track study, like those done for Run 1, was in principle not possible using our recorded data for Run 7.

As a result of these deficiencies, we discontinued using the PIP video system for Runs 8 et seq. At the same time, our experience with the DAQ in Run 7 gave us confidence that there would be no significant loss of data with the implementation of this change (the PMT and FGM output signals were satisfactorily recorded by the DAQ), and we concluded that the use of the digital oscilloscope and a second camera and VCR would not be required.

6.4 Data Acquisition System

As mentioned above, for Runs 7, 8, and 9 a LabVIEW controlled DAQ system was incorporated into the experimental configuration. The LabVIEW program resides in a Dell PC and controls a 16 bit A/D converter[12], which has a maximum of 32 channels of differential input. The voltage range of each input can be specified separately, from a minimum of ± 0.1 V up to a maximum of ± 10 V. The A/D sampling rate can be set by the operator. The maximum rate is 10^5/s. The sample duration for each input channel was measured to be ~3 μs. The computer also houses a card to process the data from the optical spectrometer, which also is controlled by the LabVIEW program.

In order to be assured (except for spectrometer dead time) of obtaining a spectrum upon a PMT trigger, a ring buffer of ten sequential spectra resides in computer memory. During the data taking runs, the spectrometer continuously updates the ring buffer in a free-running mode. The integration time for each spectrum was set to be 300 ms. With this setting, the average cycle time per spectrum was measured to be 0.588 s, which yields a spectrometer live time of 51% for this ring buffer arrangement. Upon receiving a PMT

[12] National Instruments Model SCB-100 (PCI-6031E).

trigger, the LabVIEW program stores in memory the last *n* and the next (10 – *n*) optical spectra, where *n* can be selected by the operator. We empirically determined that *n* = 3 was suitable to assure that the 10 spectra in the ring buffer (which was then read into the DAQ data set for the run) would span the event time of the PMT trigger. (Of course, the specific event could still fall into the readout dead time between the recorded spectra.)

The LabVIEW program also includes provision for a software trigger so that the operator can (try to) obtain a spectrum of the cavity lights for those occasions when the cavity lights would be of sufficient duration, but for which there might not be a PMT trigger. A block diagram of the experimental configuration for Run 7 is given in Fig. 33.

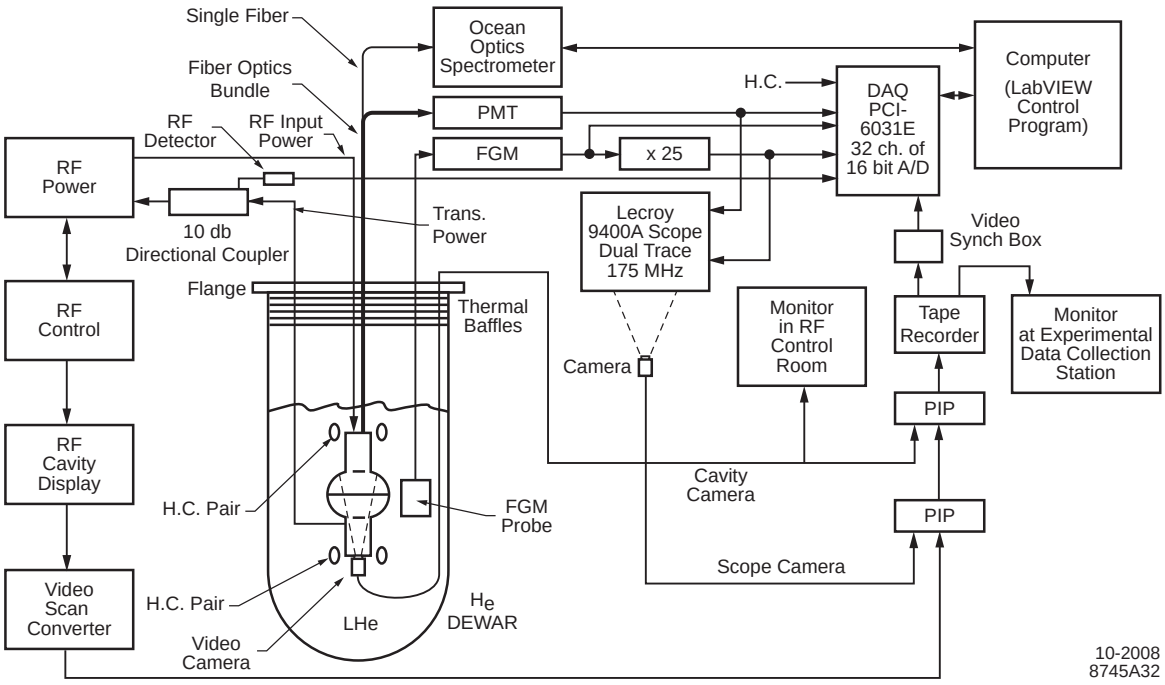

Figure 33. Block diagram of experimental configuration for Run 7, including the data feeds to the DAQ System. Note that the RF detector rectifies the 1.5 GHz TP signal and supplies the DAQ with a negative voltage proportional to the TP signal envelope. (For simplicity, only one cavity is shown in the dewar.) The H. C. input to the DAQ is the voltage across the Helmholtz coils. The wiring to the Helmholtz coils, the H. C. power supply, and the audio circuitry, as described in the text, are not shown.

6.5 Short summaries of additional runs

Some runs turned out to be unproductive. However, even negative results can be useful, and we include them here for the sake of completeness. For example, Run 3 was our first effort to (try to) reproduce the earlier results, but no results were obtained. We suspected that this might have resulted from the particularly fastidious cleaning (which included a high-pressure rinse) of the cavity prior to installation. (The cavities used in this series of runs were processed using variations of the standard JLAB cleaning procedures, but without any bake cycles.) The fastidious cleaning would be expected to lead to a paucity of field emission sites. The null result tended to confirm our suspicions that field emission and/or field emission sites might be a factor in the cavity lights phenomena, and we decided henceforth to omit the high-pressure rinse step.

In Run 4 we roughened a spot in the cavity interior near the iris to try to enhance field emission. However, there was a problem with the control software for the cavity RF. Power could not be fed to the cavity and no results were obtained.

In Run 5 we tried to reproduce earlier results, but with no cavity enhancements for field emission. We got one diagonal track and a one cycle orbit. In Frame 57807 we recorded a flash event with a PMT pulse (estimated to be 135 mV) and a possible small associated magnetic field signal. This flash event saturated the video field and is visible in only one frame (not shown). No MLO activity followed the flash. Seven frames subsequent to that containing the flash, we observed in the oscilloscope PIP insert the onset of the image displaying the PMT and FGM traces associated with the flash. The 7-frame time delay (233 ms) furnished time for the digital scope to (finish processing and) display the PMT and FGM time waveforms that accompanied the flash. We reproduce in Fig. 34 a frame displaying the PMT and FGM traces associated with the flash.

This flash event of Run 5 furnished two important pieces of information. First, it indicated that the duration of the flash is on the order of one or two ms. (It is difficult to be precise using the video record of a single event displayed at 20 ms/div; there is a more detailed discussion of flashes in *Sec. 7.2.3.*) And second, it indicated that there (probably) was an external magnetic effect associated with the flash phenomenon. These conclusions were confirmed by the DAQ data collected in Run 7.

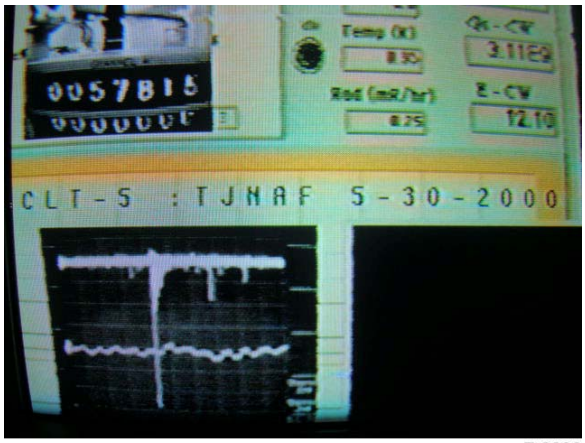

7-2008
8745A26

Figure 34. Frame 57815 of Run 5. The cavity camera output is displayed in the PIP insert in the lower right hand corner. (The flash in Frame 57807 is well over by this time, hence the insert is dark; subsequent to Run 2, no external light was introduced into the cavity during the data taking.) The oscilloscope camera output is in the PIP insert in the lower left hand corner, which here displays the PMT and FGM traces relevant to the prior flash (see text). The scope sweep time scale is 20 ms/div., the sensitivity of the PMT (upper trace) is 20 mV/div., and the FGM (lower trace) is 10 mV/div. (4×10^{-5} G/div.).

In Run 6 we applied near the cavity iris a small drop of slurry of 1μ tungsten powder[13] to enhance field emission. We got a few SPL's, much field emission, several episodes of CID's, several saturating flashes, a few quick tracks, and many cavity quenches, but no major MLO activity. In short, there was essentially nothing new to be found in this data.

[13] Accumet Materials Co.

(It also should be added that the cavity Q for this run was quite low: 1.3×10^9.) This result indicated that too many field emission sites were undesirable. It might also be concluded that 1μ tungsten powder does not furnish the right kind of field emission sites.

In Run 7 we set up a two-cavity test with no special field emission enhancements. This run was the occasion of the initial use of DAQ system. Since the PMT pulses appear to have the shortest time constant of the phenomena under study, and based upon the PMT waveform obtained in Run 5, we concluded that 1000 samples/s was fast enough to acquire the PMT pulses associated with the flash. Hence, the sampling rate was set to be 1000/s for the set of A/D inputs. The reason not to choose a higher sampling rate was to keep the memory requirements for data storage within reason. An extremely interesting and extended MLO episode (which is further described below) was observed in the new cavity (P4-1311). We should also mention here that the trigger function of PMT signal was mislabeled in the LabVIEW program so that no optical spectra were taken in Run 7. However, the DAQ still sampled and recorded the PMT signal.

After the test of the new cavity, we then tested the original cavity (HP1-9105), but nothing of significant interest was observed. Hence we omit further discussion of that part of Run 7, except to note that it is not clear why two cavities similarly prepared and similarly installed should exhibit such different behavior. One hypothesis is that one cavity (P4-1311) had a helium leak (see below) and the other did not. Also, the test on HP1-9105 took place after the test on P4-1311, allowing more time for the excess helium to be pumped out.

Run 8 used the same cavity configuration as Run 7, but with no additional cavity work. The purpose of this run was to see if, with no changes in configuration, the results of Run 7 could be reproduced. In fact, the cavity configuration was maintained under vacuum for the period between these two runs. As we were setting up for the run, we discovered that the camera viewing HP1-9105 no longer functioned. We suspected that this was due, in part at least, to radiation damage. Thus, in Run 8 we tested only P4-1311, which in any case was the cavity of interest.

As we started the run, there was evidence that we still had a helium leak into the cavity; we had to supplement the cavity ion pump with a turbopump to maintain the cavity vacuum. No flashes or MLO's were observed; we attribute the lack of flashes to the prior processing done in Run 7a. However, we observed some SPL's in the same locations as they were at the end of Run 7a, indicating the continued presence of field emission sites. In addition, there were extensive periods of CID's. These CID's gave rise to a number of spectrometer triggers in which we saw in the spectra a narrow peak centered at ~694 nm, which we discuss further below.

In Run 9 the new cavity was prepared in the usual way (without the high-pressure rinse). During the data taking part of the run we observed a number of flashes but no MLO's. Toward the end of the run, the cavity began to glow. This CID was seen first in the iris regions, and then more generally. These CID's imply the existence of some helium in the cavity, but maybe there wasn't enough to stimulate MLO activity.

Again, during this CID activity, we collected a number of spectra that exhibited the 694 line (but nothing else above background). We show in Fig. 35 a typical spectrum. 694 nm is commonly recognized as the ruby laser line. We should also note that evidence for the 694 ruby line has been observed in experimental studies of surface breakdown of

microwave windows [14, 15]. In those experiments, this line was attributed to radiation from a small amount of chromium contamination in the sapphire window material. Similarly, our observed 694 line could be caused, for example, by vacuum ultraviolet radiation associated with the CID stimulating a chromium impurity in our sapphire window material. A simplified picture, then, has helium atoms entering the cavity through a small leak (or maybe they derive from the desorption of helium monolayers); these atoms are ionized by field emission electrons; and the recombination of ions and electrons yields vacuum ultraviolet radiation, which stimulates the ruby line in the sapphire window material. The original helium lines are presumably not seen because most of their energy falls below the lower limit (350 nm) of the wavelength range of spectrometer sensitivity.

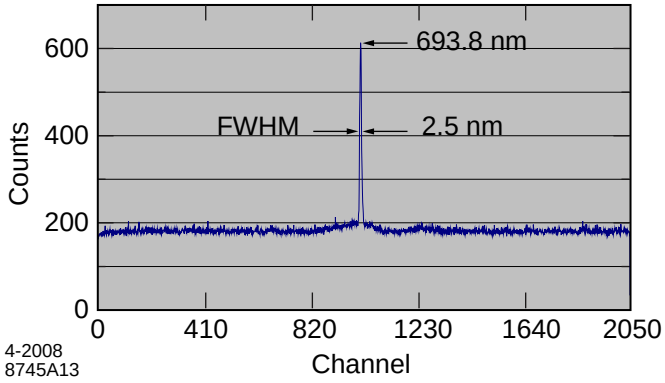

Figure 35. USB2000 spectrum ($350 \leq \lambda \leq 1000$ nm) taken during a fairly intense CID toward the end of Run 9. The peak is in Channel 1013 at $\lambda =$ 693.8 nm with a FWHM of 2.5 nm.

7. Run 7

7.1 Helium leak

Before describing the cavity lights data of Run 7, we describe an occurrence that happened during the cool down from 4 K to 2 K, before the run actually started. The control valve through which the dewar helium gas returns to suction temporarily froze up, causing the pressure inside the dewar to rise to about 15 psig. At the same time the cavity vacuum went bad, requiring the employment of a turbo-pump to supplement the ion pump. After judicious application of heat to the suction valve, the helium system got back on track and both vacua recovered.

As an explanation of the loss of the cavity vacuum, one supposes that there was a small helium leak from the dewar helium space (through a flange seal?) into one of the cavities, and that the high pressure in the dewar forced additional helium into the cavity vacuum, degrading the cavity vacuum. When the dewar pressure was brought down again, this leak was presumably still there, but of a smaller magnitude. Hence, a certain amount of helium must have continued to leak into the cavity. We mention this because it may have a bearing on the understanding of MLO activity. That is, this occurrence strongly suggests the presence of a small helium leak into the cavity vacuum for this run, and, in view of the results of Run 7, it offers substantiation for the hypothesis that a certain amount of helium in the cavity may be an important contributing factor to the production of the various anomalous luminous phenomena, and MLO's, in particular.

7.2 DAQ data analysis

Table V lists the DAQ inputs for Run 7 with the standard deviations of the intrinsic channel noise that were obtained from the DAQ data in the first two minutes of the run before the RF power was applied. No-signal (mean) reference voltages, also found in this period, were for the PMT +(0.0780±0.0006) mV and for the Transmitted Power (TP) –(2.64±0.01) mV. (N. B., we use the traditional designation of TP for the Ch. 6 signal, although as a directly collected voltage, it is actually proportional to the cavity accelerating gradient.) Both the PMT and the TP signals are negative-going voltages; that is, a larger signal puts a more negative voltage into the DAQ input. Consistent with this fact, the PMT and TP signal traces will (generally) be plotted in the figures as negative going voltages, just as they come out of the DAQ LabVIEW control program. In the discussions in the text, we will refer to the PMT and TP signal levels as magnitudes, meaning that larger negative signals ° larger magnitudes. The LabVIEW program also recorded in the DAQ data file the sample number *N*. *N*, which denotes milliseconds, is the primary time base for the experimental data.

To facilitate the analysis, we divided the 20.7 min run ($0 \le N \le 1239499$) into 21 one-minute pieces of 60,000 samples each. (An Excel spreadsheet contains a maximum of $2^{16} = 65{,}536$ rows.) To furnish a general overview of Run 7, we have constructed Fig. 36 (It is not actual data.) as a depiction of the DAQ data (TP, PMT, and FGM) for the full run. (For convenience of layout, in this figure, we have reversed the sign of the TP signal and have plotted it as a positive voltage.)

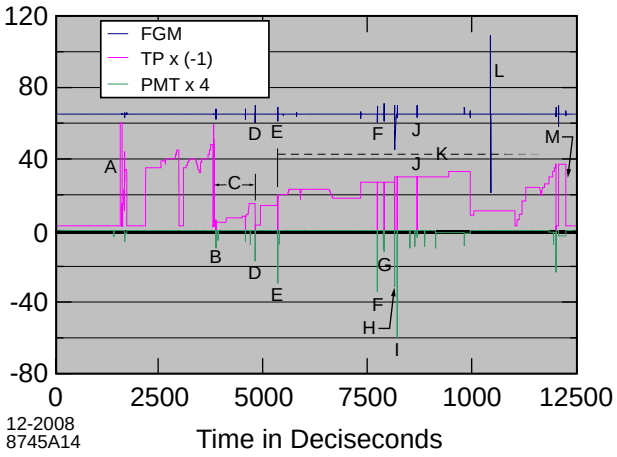

Figure 36. Overview of the FGM, TP, and PMT data for Run 7. For convenient plot layout, the FGM signal is located at +65 mV (and without the slow drifts), and the TP signal is plotted as a positive going signal with its power-off level set at +2.6 mV. (The mean power-off level in the actual DAQ data is measured to be –2.6 mV.) The TP undershoots seen in the figure represent actual undershoots in the data (associated with flashes and TP signal losses). The PMT signals are plotted as negative going signals, but multiplied by four. Correlations between these traces, as described in the text, are evident, and a number of events of interest are indicated. A: First power to the cavity at 152.8 s; B First track seen in video (Frame 11105); C:Interval of extensive Mode II behavior, terminated by Flash No. 3 (D) at 4784.1 s;E: Flash No. 4, initiating another interval of (Mode II) MLO's in the cavity; F: FlashNo. 5; G: Flash No. 6; H: Flash No. 7; I: Flash No. 8; J: Flash No. 9; K: Mode IIMLO's (episodically) visible; L: Pulse to Helmholtz coils; M: Power turned off at1213.5 s.

7.2.1 FGM corrections

One of the first things we noticed in looking at the DAQ data was that the FGM signal in Ch. 2, which is a very low level signal, had in the A/D picked up some crosstalk from the adjacent video square wave in Ch. 1. The magnitude of the crosstalk amplitude in the FGM channel is ~ 2 % of the video square wave amplitude. This problem is illustrated in Fig. 37, where one can see that the crosstalk signal is actually a square wave with rounded corners. Hence, to obtain an improved first order correction quantity, we decided to reduce the square wave subtraction and to supplement it with a suitable sine wave component of the same phase and frequency. To obtain the desired sine wave, we compared the expression

$$0.07 \sin\left(2\pi f_{vid} \frac{N - N_0}{1000} \right) \tag{11}$$

to the (symmetrized) square wave amplitude (±0.0625 V), where f_{vid} and N_0 were chosen to enable a match to the frequency and phase respectively. We found that N_0 = (6.5 ±0.5) ms and f_{vid} = (29.97062 ±0.00001) Hz provided this match, as illustrated in Fig. 38. The long-term stability of the 1000/s sampling rate was verified by spot checks of this relationship throughout the run data set, which indicated that the zero crossings of the square wave and the sine wave (with these parameters) did not exceed a millisecond.

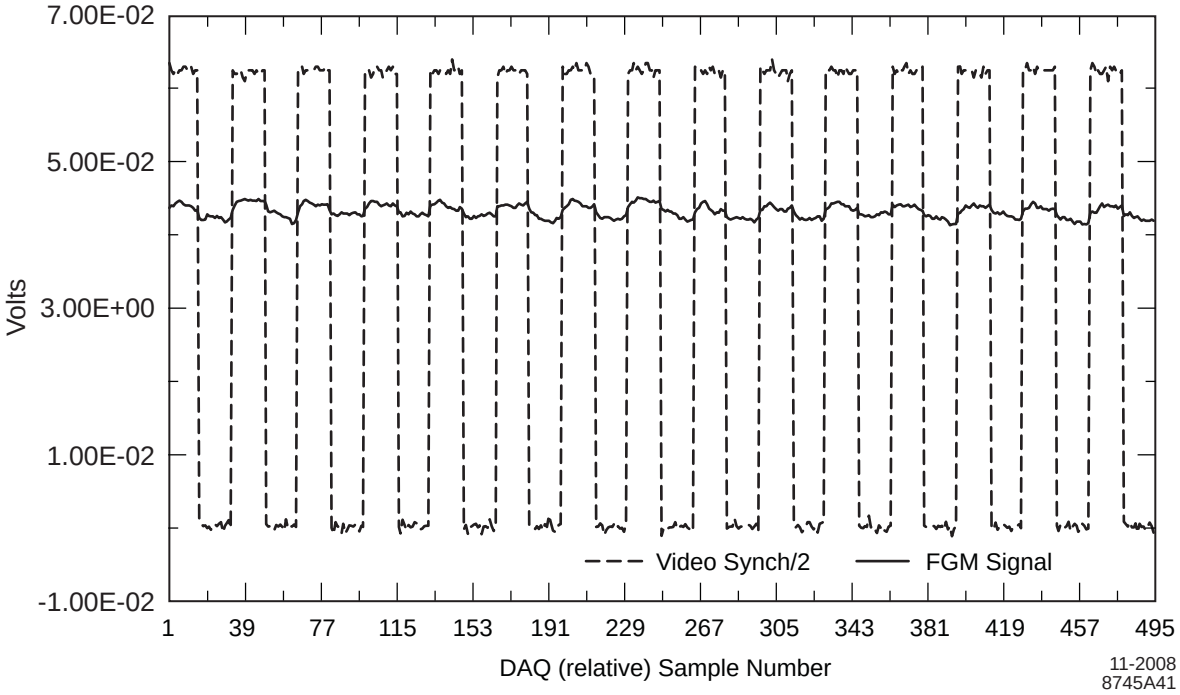

Figure 37. Evidence of cross talk from the video square wave (Ch. 1) into the FGM signal (Ch. 2).

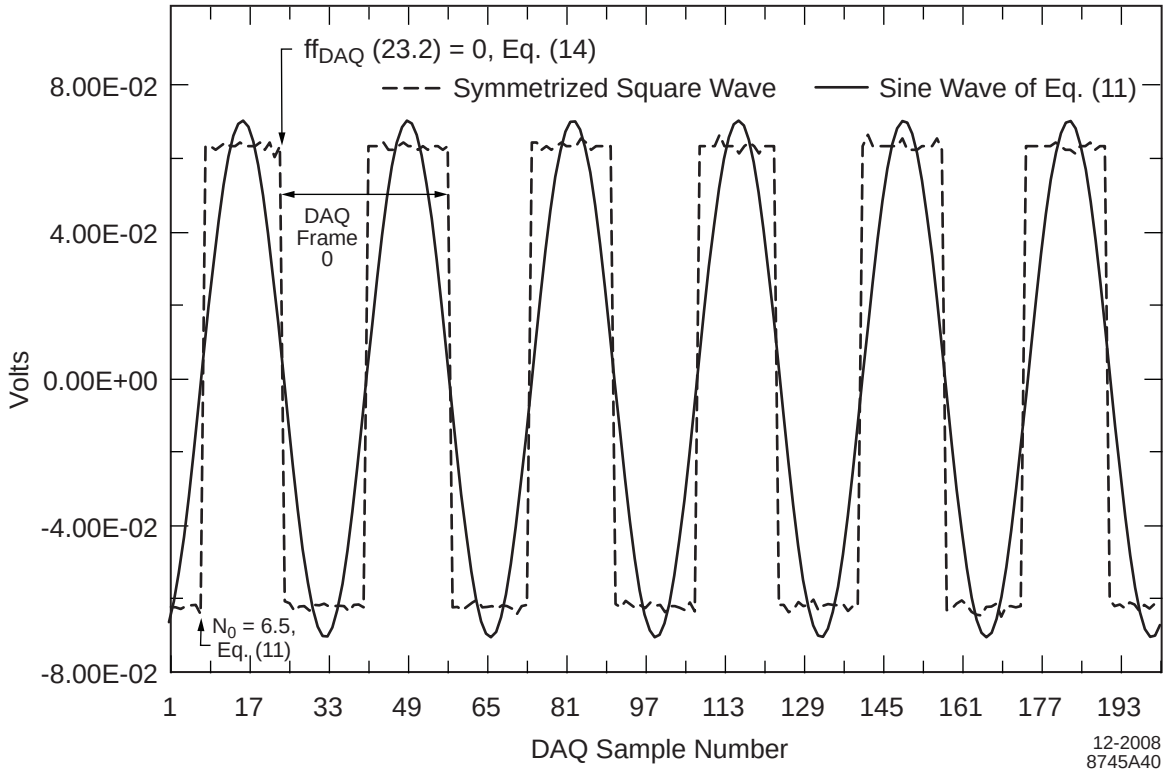

Figure 38. Comparison of the sine wave of Eq. (11) to the video square wave in the first few cycles of the run. The initial DAQ frame, as defined by Eq. (14), is indicated. The negative excursion of the (symmetrized) square wave represents Field 1, and the positive excursion, Field 2.

We thus formulated a (first order) corrected FGM signal: *FGMc*. That is,

$$FGMc = FGM_{raw} - 0.00065 \sin\left(2\pi f_{vid} \frac{N - N_0}{1000}\right) - \frac{Video\,SW}{125}. \qquad (12)$$

This correction reduces the σ of the DAQ FGM signal from 0.94 mV to 0.51 mV (2×10^{-6} G), while retaining the full frequency range of the FGM sensitivity.

As we will see below, the FGM transients associated with the DAQ events appear to be of fairly low frequency. (Their typical duration is ~100 ms, implying a maximum Fourier frequency component of ~10 Hz.) Hence, to enhance the visibility and measurement precision of these FGM transients, we formed a 15-point moving average function,

$$\langle FGMc(N)\rangle_{15} \equiv \frac{1}{15}\sum_{n=-7}^{+7} FGMc(N+n), \qquad (13)$$

which smoothes the data in the time domain and imposes a (sin *x*)/*x* envelope in the frequency domain. Eq. (13) diminishes a 10 Hz sine wave component by < 4% and reduces a 60 Hz component by an order of magnitude; its 3 db point in the frequency domain is at $f \cong 30$ Hz. The efficacy of these corrections is illustrated in Fig. 39. The FGM data in all subsequent figures has been corrected by Eq. (12) and smoothed using Eq. (13). (N. B. For plotting convenience, the $\langle FGMc\rangle_{15}$ traces may be displaced vertically in the various figures. The dc level of this signal is not significant.)

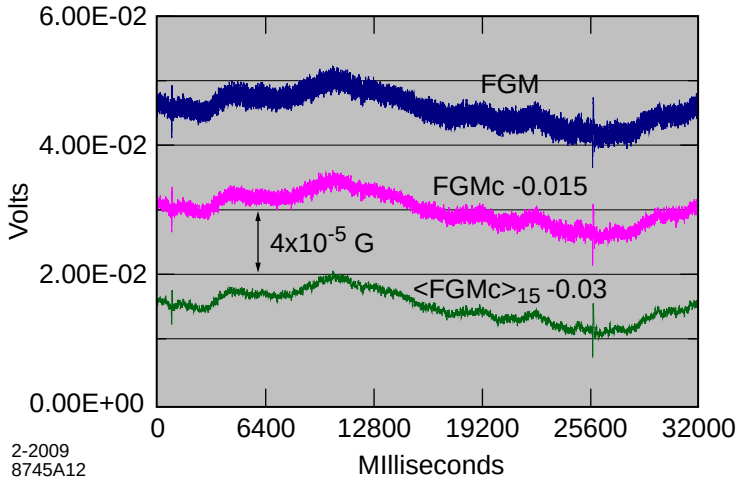

Figure 39. A 30 s stream, stating at N = 450000, of FGM points. As denoted, the *FGMc* curve is displaced by −0.015 V, and the $\langle FGMc \rangle_{15}$ by −0.03 V, below the raw data. The perturbations in the FGM signal associated with Flashes 1 and 2 are evident in all three traces.

7.2.2 Continuous interior discharge (CID)

In this run, some kind of stable discharge mechanism produced extended intervals of a significant amount of visible light in the cavity. At the beginning of the run, shortly after the application of RF power to the cavity, a period of ~5 s of a steady level of interior illumination was observed in the video data (Frames 4589 through 4741, which span 163203<*N*<168308). This 5 s period of illumination occurred shortly after point A as indicated in Fig. 36; note the small excursion in the PMT trace. (See also Fig. 41, below.) Fig. 40 gives a typical frame from this sequence. (To eliminate unnecessary detail, we have cropped this figure to show only the PIP insert of the cavity camera video frame. Since this cropping removes the PIP insert containing the frame number, we have reinserted the relevant frame number into each image. Also, we note that to improve visibility, these video fields from Run 7, except for Fig. 55, have been enhanced as described above re Fig. 25.)

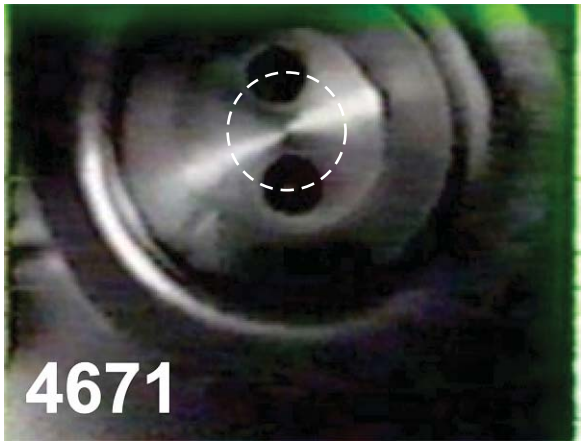

Figure 40. Frame 4671, at N = 165907, which shows the general interior illumination of the cavity by an unknown but stable CID. The wedge shaped form of the reflections seen in the far flange probably derives from the concentric circular ridgesthat remain on the interior flange surface from the original machining process. The dotted circle added to the image of the cavity indicates the

location of >20 s circulating orbit of the brighter of the two MLO's (MLO_1) described in *Sec.7.3.5*. It can be seen that this circle passes directly in front of the two (darkened images of the) ports in the far flange. Using as a reference the ID of the beamtube (7 cm) at the far flange, and assuming that the orbit is in the equatorial plane leads to the estimate of 1.9 cm as the diameter of this orbit. (**8745A52**)

As one can see, the illumination was bright enough for one to discern some interior details of the cavity, e. g., portions of the far iris, the far flange, and the darkened images of its two ports (for the RF feed and the optical window). This CID is quite different in appearance from the earlier ones (e. g., Fig. 12b) in that there appears to be no light emanating from the vacuum volume itself. No obvious source for this light is apparent. However, interior reflections indicate that more light was coming from either the 2 o'clock or the 8 o'clock azimuthal direction. It is also of interest to note that no SPL's can be seen in this video field. This initial period of luminosity indicated that the video recording started at about 10 s after the initiation of the DAQ data taking.

Complementary to the video data, the PMT signal furnishes an illumination (and flash) monitor but with more precise timing and intensity information. To initiate this analysis, it was useful to juxtapose the PMT signal and the TP signal in this time interval. Fig. 41 displays the PMT and the TP signals for a 30 s period starting at $N = 150000$. The TP signal began to rise at $N = 152816$, building up to a magnitude of ~60 mV (the highest level in the run) at $N = 153075$. It continued (for ~4 s) at this level until a loss of TP signal (See *Sec. 7.2.4*, below.) occurred at $N = 157180$. The PMT signal (and the video) indicated that there was no interior illumination during this period. However, as indicated by the PMT signal (and confirming the video data of Frame 4589 et seq.), there was some interior illumination a few seconds later. This period of interior cavity illumination was terminated by another loss of TP signal at $N = 168306$. It is interesting to observe that during this period of interior illumination, Fig. 41 indicates that the TP voltage level was roughly half of that of the above mentioned 4 s dark period. During this period of interior illumination (the same 5 s interval mentioned above), the mean of the PMT signal shifted by (0.282±0.004) mV. (Although the shift is only about twice the σ for the distribution of the independent PMT pulses, averaging over many samples enables a reasonably precise estimate of the displacement of the mean due to continuous light production.)

Finally, there was an extended period of general interior illumination from Frame 6092 through Frame 7196 (which span $213352<N<250222$). As indicated in Fig. 36, this period was initiated when the TP signal went from null to ~35 mV. However, while the TP signal continued at a fairly steady level, it is interesting to observe that the video and the mean PMT signal dropped significantly at Frame 6808. (The TP signal actually increased slightly at that point.) Ultimately, the video rasters went dark (confirmed by a coincident drop in the mean PMT signal) at Frame 7197. The fact that the TP signal continued on at essentially the same (or greater) level for >40 s beyond Frame 7197 indicates that while an accelerating gradient may be necessary for the production of this type of CID, it is not sufficient. Furthermore, when there is an interior illumination level present, it is not necessarily a monotonic function of the TP signal.

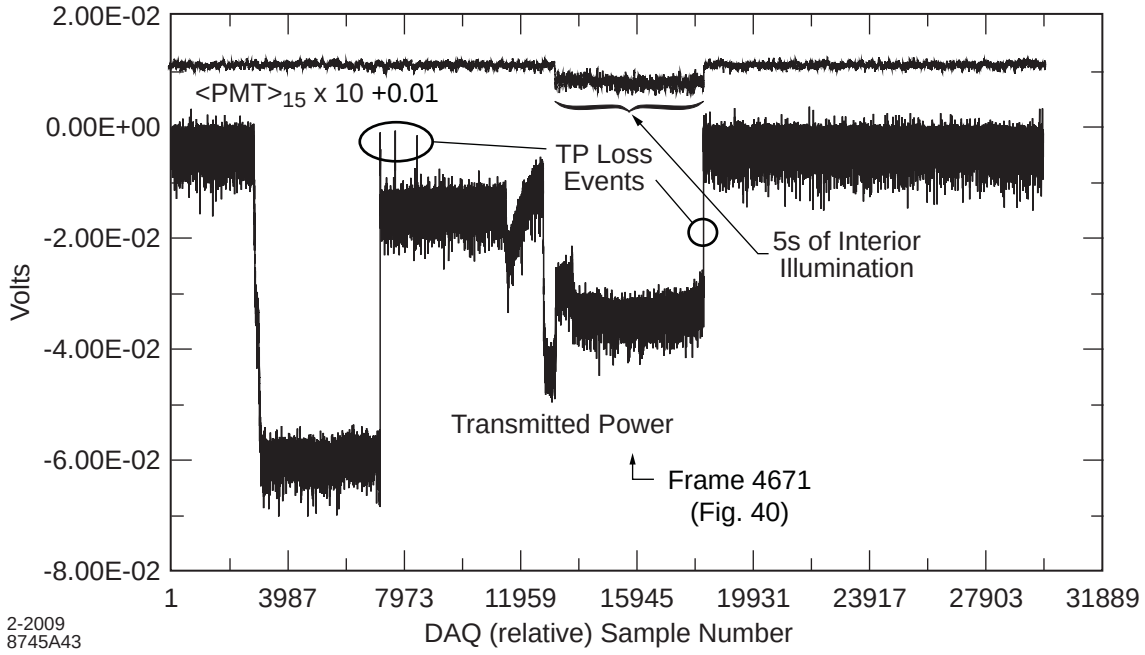

Figure 41. A 30 s stream of the TP and PMT signals starting at N =150000. [The PMT plot is a 15 point moving average, as defined by Eq. (13), multiplied by a factor 10, and raised by 10 mV to be clear of the TP plot.] The location of the 5 s general illumination in the cavity, which includes Frame 4671 (Fig. 40), is indicated. Also, the location of four loss-of-TP events are indicated.

Throughout the run, illumination from various CID's appeared to be the rule rather than the exception. However, it should be said that the character of the CID's later in the run appeared to be different from that seen in this earlier portion, e. g., in Fig. 40. Again, as in Run 2, toward the end of this run, the CID luminosity appeared to emanate from the vacuum volume itself (See Fig. 12b.). The light from this CID posed an additional problem in that it caused the auto-iris to close down, thus reducing the visibility of other light sources, e. g., MLO's, in the cavity.

7.2.3 Flashes

As with earlier runs, in particular Run 1, flashes are in clear evidence in this run, and, as before, they varied considerably in intensity. But now, having DAQ data, it is possible to identify them more reliably and quantify their signature. The first step in this process was to survey the entire PMT sample set looking for large PMT pulses. (As a point of reference, we note that the largest RF-off PMT pulse was 0.95 mV.) The largest of these is located at N = 812216 and has an uncorrected peak magnitude of 14.9 mV. (We note that this amplitude is much less than that seen in Run 5. One factor contributing to this reduction is that we had divided the optical bundle to accommodate two cavities for Run 7. Another factor could be an intrinsic variability in the flash phenomenon itself. (See a more detailed discussion in *Sec. 8.3.*) The DAQ data points for this pulse are shown in Fig. 42. With the expanded time scale, we see that the pulse rise time is < 1 ms and the 1/*e* decay time is ~2.2 ms. (The decay does not appear to be exponential, however.) These data points are consistent with the estimated flash duration obtained from the video of the oscilloscope trace in Run 5 (Fig. 34).

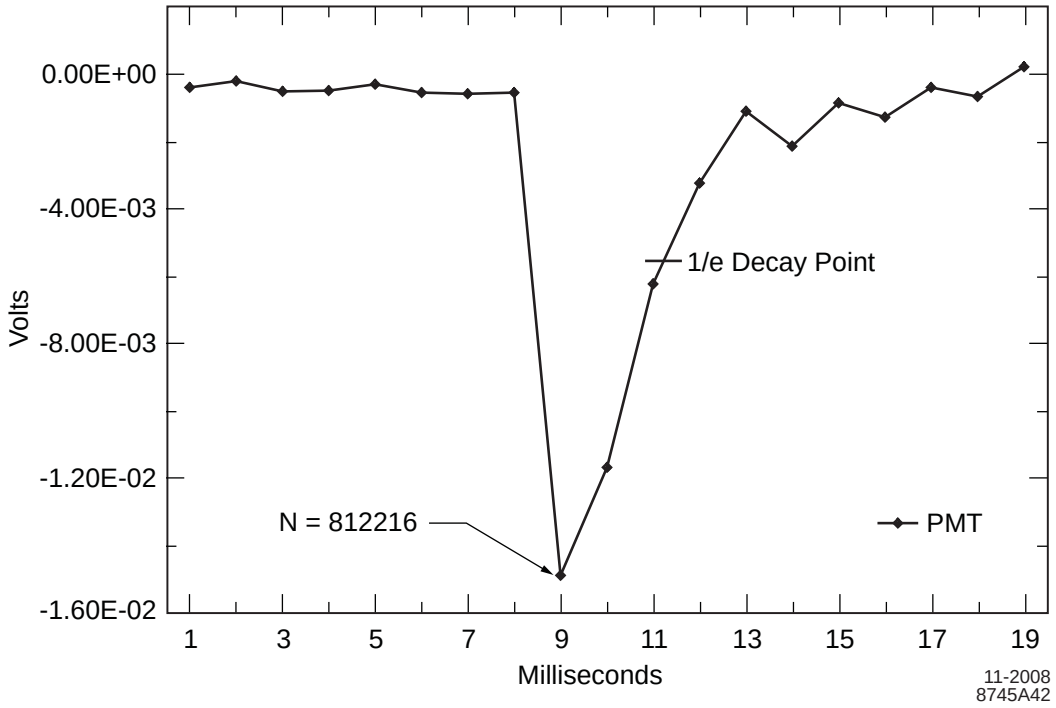

Figure 42. The largest PMT pulse in Run 7. The peak sample point of 14.9 mV occurs at N = 812216 as indicated. The 1/e decay point, which implies a decay time of ~2.2 ms, is also shown.

The next step was to compare for this event the contemporaneous TP and FGM data to the PMT data, which is done in Fig. 43. These data show that the flash drains all of the RF energy from the cavity. Consequently, we define the flash, as observed in Run 7, as an event characterized by the observation of a significant and brief pulse in the PMT signal and a correlated abrupt and complete loss of the TP signal. By "abrupt" we mean within one or two ms. (To help contrast the nature of this event with the TP-loss events discussed below, we have drawn in an exponential recovery rise time τ_{TP} = 23 ms in Fig. 43.) This event is listed (in its chronological location) as Flash 8 in Table VI. In addition, this flash appears to be associated with a small transient in the magnetic field, which, taken directly from the plot, is estimated to be ~2½×10^{-5} G in (peak-to-peak) magnitude. (We do not assign errors to the values for these FGM transients, but estimate that they are on the order of 10% or less.) Since the physics reasons for the magnetic transient are not clear, we deemed it inappropriate to include it in the criteria for defining the flash. (But it turned out that this FGM transient is present in all of the flash events found in Run 7. And their onset appears to be roughly coincident with the flash pulse timing, although evidently somewhat delayed.)

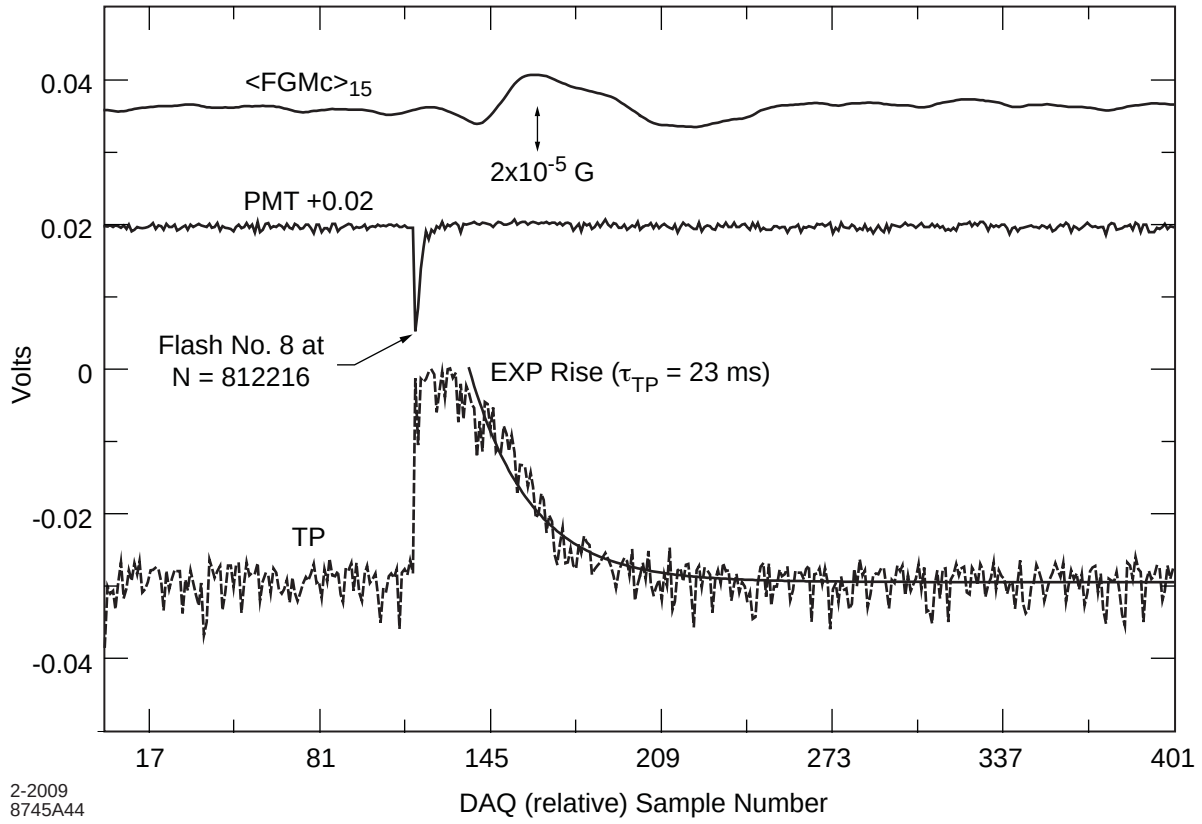

Figure 43. DAQ signals associated with the flash at N = 812216. As a qualitative reference, a recovery rise time exponential characterized by a of τ_{TP} = 23 ms is included in the TP plot. (N. B., the PMT trace has been shifted by 20 mV.)

We found six more flash candidates having peak PMT pulses of ≥ 3 mV for which the above criteria are conclusive. We list these events in chronological order in Table VI. (During some of the intervals of continuous light production, there were a number of PMT pulses that exceeded 3 or even 4 mV, but they were not accompanied by the requisite ΔTP signature, and hence were not considered to be valid flash candidates.) In addition to these events, we also list the events at N = 450809 and 859472 because of their clear ΔTP signatures and because their peak PMT magnitudes, though small (1.6 and 1.4 mV, respectively), stand out significantly above the local background pulses.

In addition to the above nine flash events, there is a region of interest (during which the TP signal level is rather small) that exhibits several small but statistically significant PMT pulses. The largest PMT pulse has a magnitude of 2.5 mV at N = 380674. As before, we plot (in Fig. 44) the three DAQ signals for this region. In order to enhance the visibility of the ΔTP signature, we have formed the 5-point moving average $\langle TP(N)\rangle_5$ and have plotted it (rather than the TP raw data) in Fig. 44. The resulting trace indicates that the most significant ΔTP signature spans N = 380557 to 380568 (The abrupt drop in the TP level has been stretched by the averaging process.), evidently matching with the timing of the PMT pulse (of magnitude 0.7 mV) at N = 380565. (It is perhaps also relevant that the onset of the contemporaneous FGM perturbation appears to align better with this earlier but smaller PMT pulse.) Because there are several PMT pulses in this region, and also because the FGM transient appears to be of longer duration (perhaps 300 ms) than typical, one might make the argument that more than one flash is present in this

region. However, assigning significant weight to the ΔTP signature evident in Fig. 44, we label the earlier PMT pulse at N = 380565 as the best flash candidate, and include this event in Table VI as Flash 1. Also listed for each flash event in Table VI is τ_{TP}, the estimated recovery time constant of the TP signal. A curve with an exponential rise of time constant τ_{TP} is drawn into Figs. 43 (23 ms) and 44 (30 ms), respectively.

The DAQ data displayed in Fig. 44 assumes special interest because it spans the time location of the first (series of) PMT pulses in the run, the first flash of the run, and also the first tracks observed in the run (as discussed below in *Sec. 7.3.2*). Using Eq. (17), below, the location of Frame 11098 (which contains the initial PMT pulse) and of Frames 11103 to 11108 (which contain the first tracks of the run) are also indicated in Fig. 44.

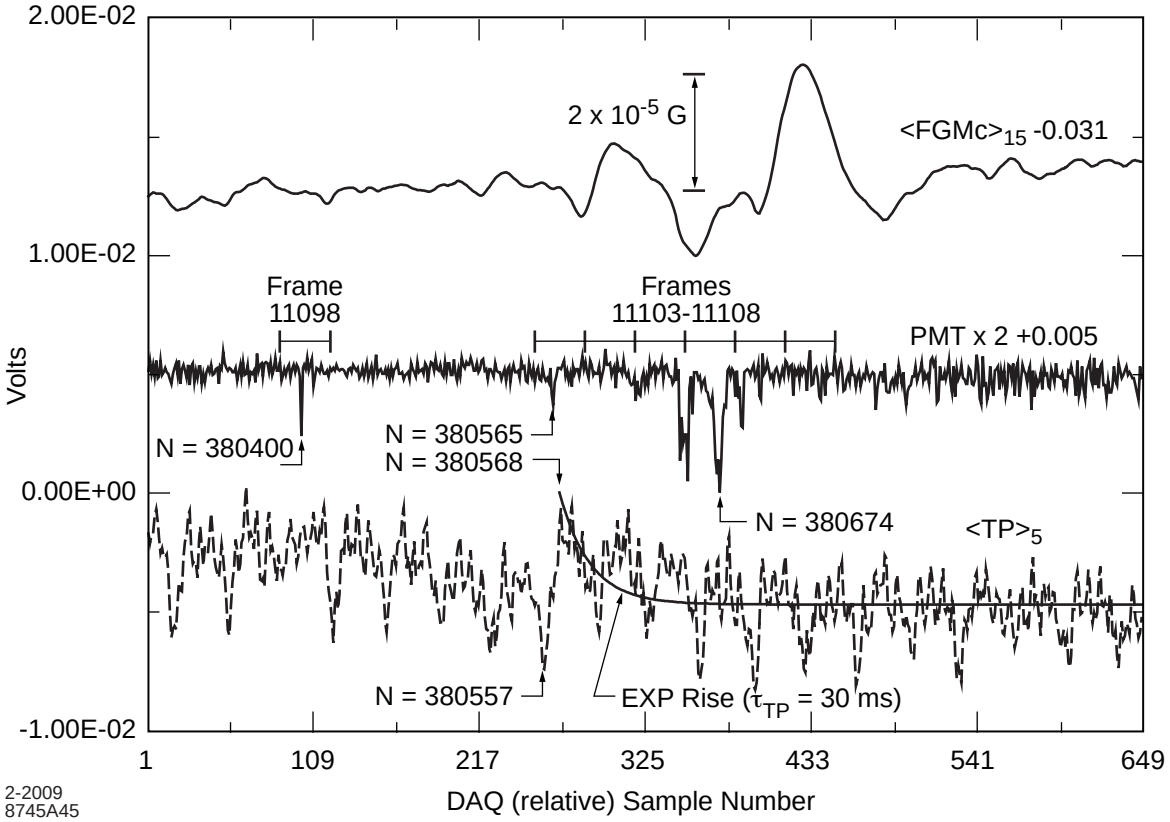

Figure 44. The DAQ signals in the Region of Interest starting at N = 380300. The location of Frame 11098 and of Frames of 11103 through 11108 (Fig. 48) are indicated. For more clarity in the graph, the PMT and FGM traces have shifted baselines, and the PMT signal has been multiplied by a factor 2.

7.2.4 Loss of TP signal

In Run 7 we found eight events characterized by the total loss of the TP signal (including the two mentioned above in *Sec. 7.2.2*), which, unlike the flash events discussed in *Sec. 7.2.3*, exhibited neither a significant PMT pulse (All PMT levels remained < 0.5 mV.) nor any significant evidence of an accompanying FGM transient. (Possible FGM transients were $<10^{-5}$ G.) We have not labeled these events as quenches, however, because they do not appear to be representative of the classical loss of cavity excitation through the process of thermal breakdown, as discussed by Padamsee, et al [Ref. 8, p. 199 et seq.]. The salient departure from "classical" behavior is the rapid and non-

exponential recovery of the TP signal; the observed recovery times are considerably shorter than those defined by the τ_{TP} of the flash events (which are mainly governed by the cavity Q). We list these TP-loss events in Table VII. (The locations of the first four have already been indicated in Fig. 41.)

We illustrate a typical TP-loss event, located at N = 375672, in Fig. 45, where the very short duration of the TP signal loss (~ 9 ms) is evident. The signal level, after the rapid (though partial) recovery, indicates that about half of the resonant energy was still in the cavity at this point. The "slow" recovery from that point on manifests a τ_{TP} consistent with other such (Q governed) time constants observed in this run. A plausible explanation for these TP-loss events, then, could be some kind of brief discharge, in the vicinity of the TP or RF input probe, say.

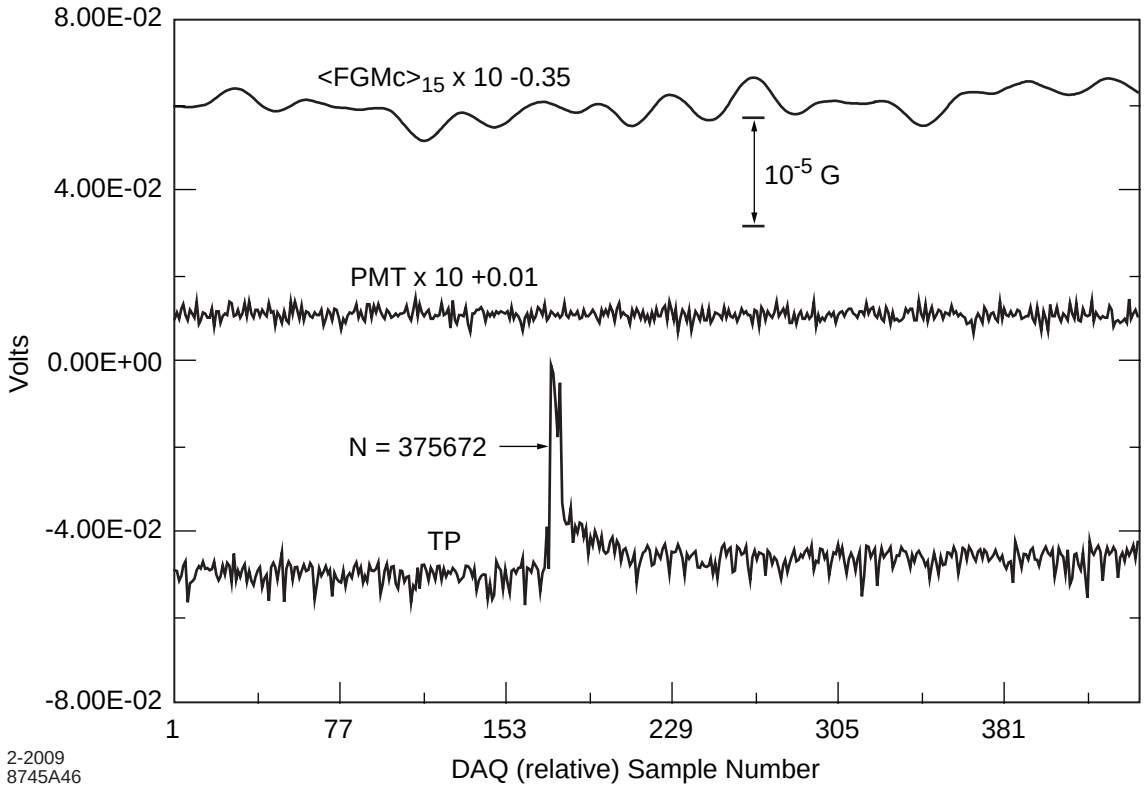

Figure 45. The DAQ signals associated with the loss of TP signal at N = 375672. (The PMT and FGM signals have been modified as indicated.)

No TP-loss events were evident after the interesting video data started at N = 380565. Hence, they do not appear to have a significant bearing on the phenomena observed in the video data in that region, and we do not discuss them further.

7.2.5 FGM signature

As one can see from Fig. 39, it is easy to scan the FGM data for significant magnetic transients. While all of the flashes were found to carry an obvious magnetic perturbation, the non-flash events characterized by an abrupt loss of TP signal do not (e. g., Fig. 45). But, more importantly, there were non-flash events in which a FGM signature was observed, usually coincident with a slow change in the acceleration gradient. In these cases, the FGM signatures were usually smaller that those associated with the flashes, but

not always; one such event, associated with a change in the TP magnitude of +30 mV, exhibited an FGM signature of 4.5×10^{-5} G. We illustrate a non-flash example of an FGM transient in Fig. 46, when the RF power was turned off at the end of the run; in this instance the ΔTP was –31 mV and the FGM signature was ~1.2×10^{-5} G. A curve with the decay time constant τ_{TP} = 38 ms has been drawn into the TP data plot. And finally, there is at least one case of an FGM signature (~2×10^{-5} G) for which there appears to be no significant activity in either the PMT (no excursions >1 mV) or the TP signal. (The possibility of a very small transient in the TP signal, of ΔTP ~ 3 mV, is indicated, however.) We illustrate this event in Fig. 47.

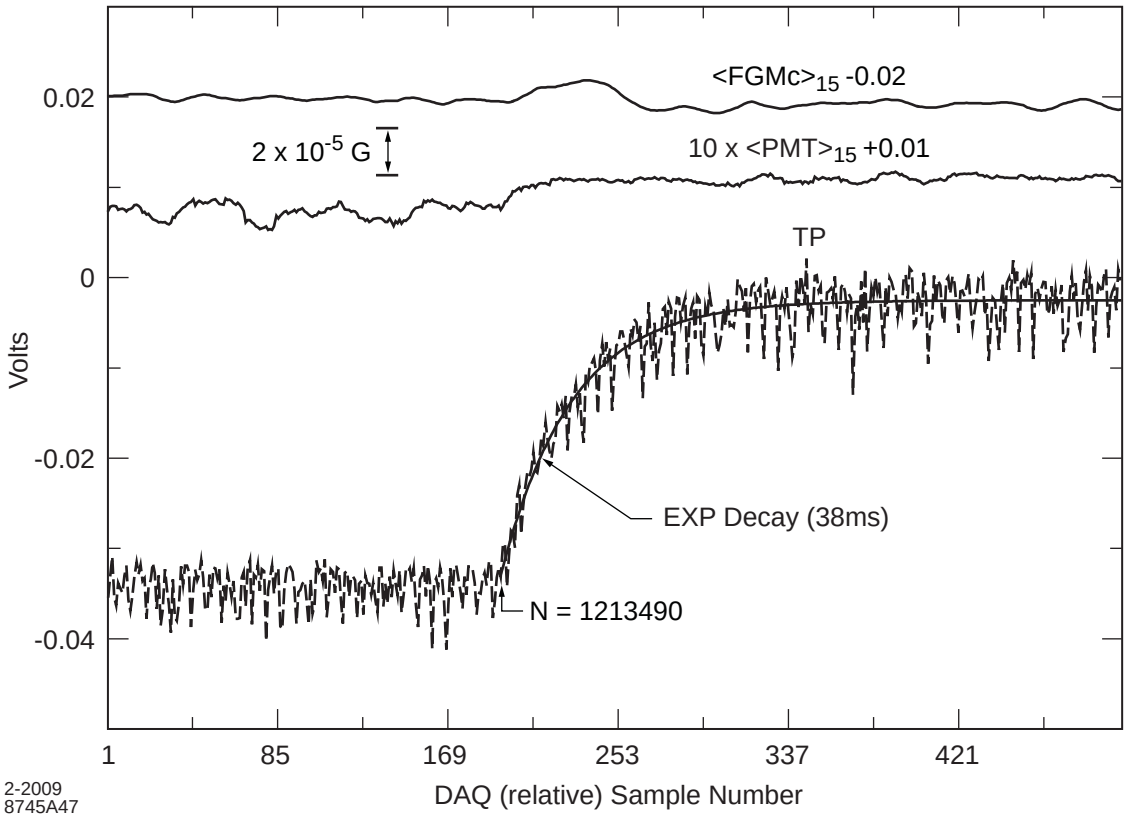

Figure 46. The DAQ signals associated with the final RF power down at N = 1213490. As a qualitative reference, an exponential decay of 38 ms is included with the TP signal. Note that when the power to the cavity is turned off, the mean PMT voltage returns to its quiescent average value.

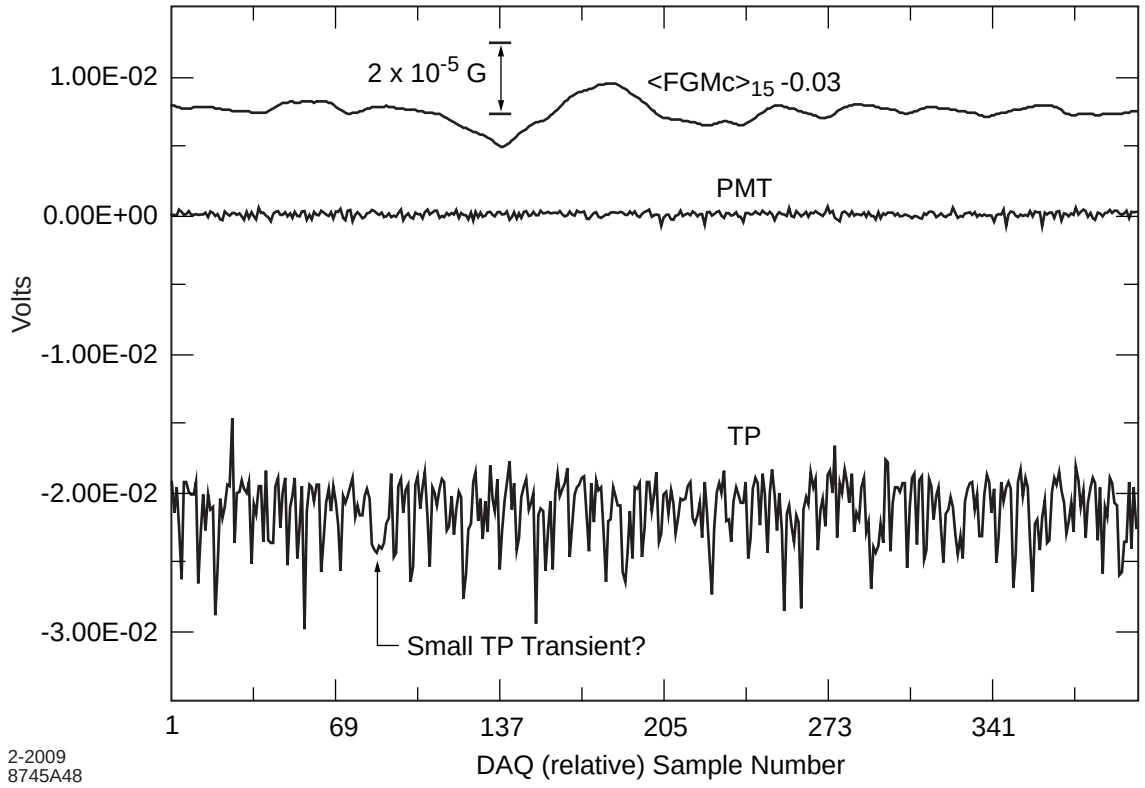

Figure 47. A 4 s stream, starting at N = 572500, of the DAQ signals associated with an FGM transient having no obvious associated PMT or TP activity.

The evidence for the presence of a low frequency perturbation in the FGM signal, evidently associated with specific events in the cavity, is incontrovertible. However, the physics process that generates this perturbation is obscure. Although it accompanies all of the flashes recorded in Run 7, its magnitude does not correlate well with that of the PMT signal magnitude nor with the associated ΔTP drop. Similarly, this FGM transient accompanies some, but not all, shifts in TP signal magnitude. And in those cases when the FGM transient does accompany a TP shift, again, there is only a weak correlation with the magnitude of ΔTP. It is plausible to hypothesize that the observed FGM transients are an artifact of some voltage associated with the RF power supply. In any case, however, further study of this phenomenon will have to wait for future runs with more experimentally recorded parameters (e. g., the incident power and the reflected power).

It is appropriate to remark here that late in the run a pulse of current (¾ s long: 1034099 < N < 1034851) was applied to the Helmholtz coils (see *Sec. 6.2.2*); the location of this pulse has been indicated in Fig. 36. We estimate that this current generated an internal (transverse) magnetic field of 10^{-6} G in the equatorial plane at the center of the cavity. No effect on the then visible MLO's was observed on the video monitors.

7.2.6 Relationship between N and the VCR frame number F_{VCR}

Eq. (11) above gives the proper phase and frequency to correlate the value of N with the recorded video square wave. To develop further this analysis, we define a continuous DAQ timeline frame function $ff_{DAQ}(N)$ to equal 0 at N = 6.5 + 33.37/2 = 23.2, which

point specifies the beginning of the initial DAQ Frame 0, as shown in Fig 38. (Recall that Field 1 of the recorded video spans the Δt when the symmetrized square wave V = –0.0625 V.) That is:

$$ff_{DAQ}(N) = f_{vid}\,\frac{N-23.2}{1000}. \tag{14}$$

We now partition $ff_{DAQ}(N_{obs})$ for an event located at N_{obs}, as follows:

$$ff_{DAQ}(N_{obs}) = F_{DAQ}(N_{obs}) + d_{DAQ}(N_{obs}), \tag{15}$$

where the DAQ Frame Number F_{DAQ} is the largest integer $\leq ff_{DAQ}$ and the decimal part d_{DAQ} indicates how far into the DAQ frame that that event resides. Field 1 is associated with $0 < d < 0.5$ and Field 2 with $0.5 < d < 1.0$.

At this point, the flash events can be used to determine the increment $\Delta F_{D\text{-}V}$ between F_{DAQ} and F_{VCR}, the frame number inserted into the (copy of the) video data tape. That is,

$$\Delta F_{D-V} = F_{DAQ} - F_{VCR}. \tag{16}$$

As mentioned above, a preliminary comparison of the DAQ data and the video data revealed that the $F_{VCR} = 0$ frame is about 10 s later than that for the DAQ (or $\Delta F_{D\text{-}V} \sim 300$). This observation enabled us to locate the video flashes to match the DAQ flashes listed in Table VI. In two cases (noted in Table VI) the flashes fully saturated the video field. In other cases, the flash was much less intense. And finally, there were cases in which there was no evidence of a flash in the (Field 1) frame-by-frame scan. In this last category, however, the existence of a flash was deduced from the dark frame that typically follows a flash. In considering all of the flashes, we determined that $\Delta F_{D\text{-}V} = 301.6$ gave consistency between the video data and the DAQ data. ($\Delta F_{D\text{-}V}$ is not an integer because of the digital delay in the PIP circuitry.) N. B. For $F_{VCR} \geq 23622$ (or $N \geq 798258$), $\Delta F_{D\text{-}V} = 300.6$ because frame number 23622 is missing from the frame-numbered video data tape.

From the above analysis, then, the equation to proceed from the video frame number F_{VCR} to an estimate for N_{DAQ} is

$$N_{DAQ} = \frac{1000}{f_{vid}}\left(F_{VCR} + \Delta F_{D-V} + d_{VCR}\right) + 23.2, \tag{17}$$

where d_{VCR} is a decimal (from 0 to 1) to indicate which part of the frame one wishes to identify; $d_{VCR} = 0.5$ will specify (to ± 5 ms) the N_{DAQ} corresponding to the center of the frame, between Field 1 and Field 2. If we invert Eq. (17), we obtain

$$F_{VCR} + d_{VCR} = ff_{VCR} = \frac{f_{vid}}{1000}(N_{obs} - 23.2) - \Delta F_{D-V}, \tag{18}$$

where the frame function ff_{VCR} is partitioned in analogy to Eq.(15), above.

7.3 Video data analysis

In looking at the video data, prior to Run 7, the behavior of the MLO's might be described as ballistic. That is, the MLO's may be characterized as (essentially) single independent objects of finite size with good self-coherence, carrying a certain mass, engaging in various interactions, and obeying Newton's laws of motion. The lowest order interaction of the MLO's in this mode, which we shall call Mode I, appears to be that associated with the potential well derived from the SPM. There is ample evidence for some kind of short range contact interaction as well. Mode I behavior, then, includes the orbits, the mid-vacuum collision, and wall-bounce events, as were seen in Runs 1 and 2.

As described below, Mode I behavior was also seen (briefly) in Run 7. But in Run 7 we also observed a qualitatively different type of MLO behavior, which we shall call Mode II behavior. A salient feature of Mode II behavior is that two or more MLO's can be seen acting as a coherent assembly, which we describe as a macromolecule. The MLO's as elements of a macromolecule also appear to carry a certain mass and engage in various interactions. It is also important to observe that the existence of a macromolecular configuration supports the earlier mentioned hypothesis (see *Sec. 5.10.2*) that there is an MLO-MLO interaction whose range exceeds the apparent size of the MLO's. It appears possible that a suitable analogy to the Mode I-Mode II dichotomy would be atomic versus molecular behavior. If this should be the case, it would be likely that the intrinsic character of the MLO's engaging in these two modes of behavior is the same. One expects that Newton's laws of motion are still primary, but the coupled equations that would be required to properly describe the multi-element macromolecule would be at an additional level of complexity, possibly including an as yet unknown force.

Another feature of Mode II behavior is that the putative SPM force is evidently not the major force for (radial) orbital stability (a further extension of the above line of argument). This fact is in clear evidence in the circulation sequence described below; the orbit is circular yet exhibits large variations in angular velocity. (See Figs. 54 and 55, below.) And it is even more striking when one observes that the macromolecules find states of stable equilibrium at rest in the cavity volume for extended periods of time. We point out that the MLO's in these resting equilibrium states are generally not on the cavity axis (The at-rest equilibrium location for the SPM force is on the axis.) and at the same time do not appear to be in contact with the cavity walls.

We give in Table VIII a chronological series of significant reference points to provide a framework for our discussion and analysis of the video data of Run 7. The essence of this discussion starts with the first PMT pulse of the run, which has been shown above to reside in the Region of Interest (Fig. 44).

7.3.1 The first PMT pulse (Frame 11098)

The video data contains only dark rasters from Frame 7197 (see *Sec. 7.2.2*) to Frame 11100 (although, as seen in Fig. 36, the TP voltage was relatively large for most of this time span). Near the end of this time span we find the first PMT pulse, which was recorded at $N = 380400$, and which, by Eq. (18), is expected to be found at $ff_{VCR}(380400) = 11098.53$, i. e., in Field 2 of Frame 11098. However, the fact that Frame 11098 is dark is still consistent with the recorded DAQ data because, as noted in *Sec. 6.3* above, the PIP circuitry has discarded the Field 2 video data, recording Field 1 twice. In Frame 11101

one can begin to see a low level amount of general illumination on the cavity irises. There is more illumination in Frame 11102, but still no SPL's.

7.3.2 Flash No. 1 (Frame 11103)

Eq. (18) indicates that the event (at N = 380565), which we have designated as Flash No. 1, is to be found in (the first field of) Frame 11103. In that frame there is some interior illumination, much stronger than that in Frame 11102 but weaker though not qualitatively different in appearance from that in Frame 4671 (Fig. 40). While there are no observable SPL's in Frame 11103, there is a streak of light that appears to be either an MLO track or optics artifact. With the data we already have in hand, this particular streak is not an important element in the central arguments about the MLO hypothesis, but if an MLO, it could be a look at an MLO in an early stage of its formation. Until we have additional data, we shall take the MLO interpretation as a working hypothesis, keeping the optics artifact possibility under advisement. (It is appropriate to note that we have not found any evidence of such optics artifacts in the other data we have.)

This track is somewhat different in appearance from the typical Mode I tracks seen in the earlier runs, in that it varies significantly in width and brightness along its trajectory. (We should also keep in mind that, if a track, its variation in brightness could be due to a time variation in the strength of the cavity excitation, rather than an intrinsic variation in the MLO itself.) If we assume that the weaker part of the trajectory is the earlier part (as was the case in some of the MLO tracks in Runs 1 and 2), this track is moving from left to right and has a CCW motion. As with many later tracks in this run, this initial trajectory passes, without perturbation, directly in front of the one of the darkened port images in the far flange. It then passes in front of the far iris and subsequently appears to execute a wall bounce (Mode I behavior) in the vicinity of the near iris. (This possible wall bounce at the end of the streak tends to support the MLO interpretation.) We reproduce this flash and track (Frame 11103) in Fig. 48a. We have included arrows to indicate the (most probable) direction of motion.

In considering the z location of this track, it is clear that it is closer to the camera than the far iris. And the wall bounce evidently places it in the vicinity of the near iris, but not actually inside the near beamtube. The several track segments seen in the next few frames, discussed in the next section, appear to be similarly placed in z.

This pair of events (flash and track) in the same frame tends to support the notion that the flash phenomenon may have something to do with the creation of the unexplained freely moving luminous objects that we refer to as MLO's. Other possible factors of relevance include the earlier PMT pulse at N = 380400 (see Fig. 44) and the earlier seen CID.

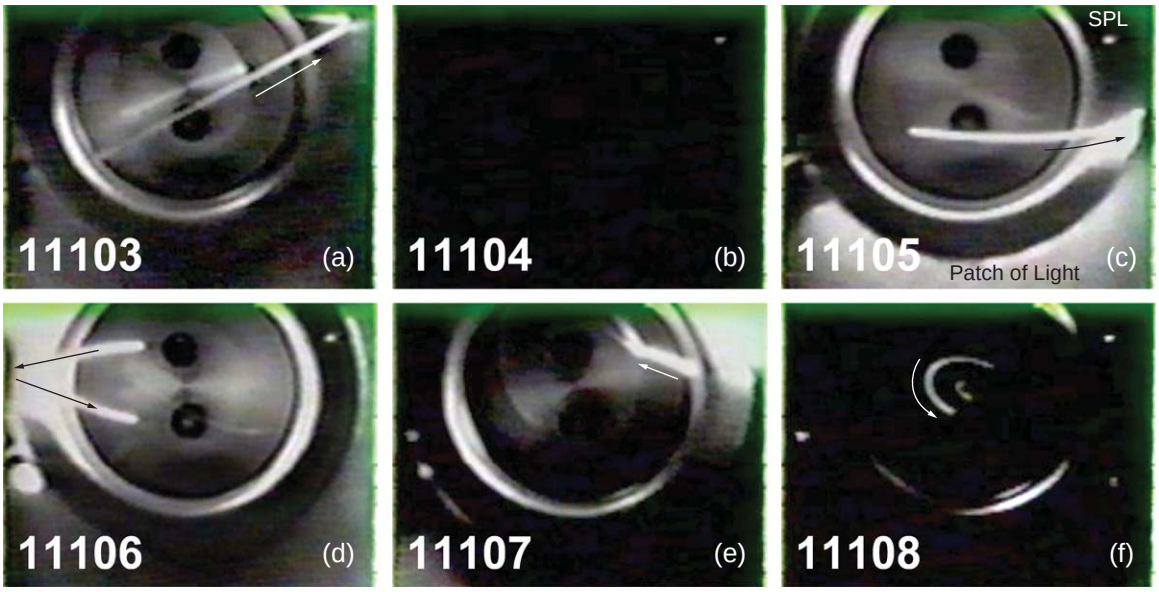

12-2008
8745A53

Figure 48. A sequence of six frames (a, b, c, d, e, f: 11103-11108) detailing the track segments of the first MLO seen in Run 7. (Again, we have cropped the monitor rasters to the size of the cavity video insert, and the appropriate frame numbers have been reinserted into the frames.) Note the presence of an SPL in all but the first of these frames. We have indicated the time location of these frames in Fig. 44.

7.3.3 Typical MLO tracks (Frame 11105, et seq.)

Frame 11104 (Fig. 48b) was dark (except for a very dim SPL near the putative wall bounce location of the initial streak). Examining the relative positions of this SPL and the streak, one concludes that the SPL was not obscured by the light of the streak in Frame 11103. This SPL was seen to brighten in subsequent frames. The track in Frame 11105 (Fig. 48c) is followed by a sequence of MLO tracks. We reproduce the rest of this initial this sequence in Fig. 48d and e. Although they appear more robust, these tracks are otherwise unremarkable in that they appear to be consistent with those already seen in Runs 1 and 2. (It is curious, however, that the patch of light emanating from the near beamtube in Frame 11105 does not appear to be consistent with the specular reflection of a track; cf. Fig. 27.) The track in Frame 11106 is a V shaped pair of segments, presumably joined by a wall bounce in the region of the near iris. The track in Frame 11107 may be exiting from a wall bounce. Also, it is somewhat more diffuse, injecting an uncertainty into its interpretation. All of these tracks are slightly curved, as one would expect from the radial force deriving from the SPM [13]. (Was the track in Fig. 48a moving too rapidly to see its curvature? Or was the cavity excitation too low at that point?) But their curvature does not appear to be congruent with a (section of a) plausible closed elliptical orbit, i. e., one that will fit within the confines of the cavity. Thus, the wall bounce interpretations are reasonable and consistent. And assuming that there was an unseen track in Fig. 48b, they could all be the tracks of the same MLO, and moving in a CCW direction.

Unfortunately, because of the deficiency of the PIP circuitry, mentioned above, we are unable to view the missing fields with their track segments, which (we presume) would

demonstrate the continuity of these MLO tracks (e. g., as was done in Fig. 10). But we believe it is fair to say that these track segments are manifestations of Mode I behavior. The more diffuse character of the track in Frame 11107 may be evidence that the original MLO, after a number of wall bounces, is breaking up, leading to the multiple MLO's described in the next section. That is, this track may actually be a part of a transition between Mode I and Mode II behavior.

7.3.4 First track of first dancing sequence (Frame 11108)

Frame 11108 (Fig. 48f) displays a much thinner track with much more curvature. (This thinner track clearly indicates that the track widths of the prior MLO tracks significantly exceed the (best) camera resolution, and hence can be viewed as having a finite size, possibly on the order of a millimeter, or more, in diameter.) This is the first frame in the first of the two "dancing sequences" seen in this run. (Consistent with the tentative conclusion of the prior sequence, we presume that this track is moving in a CCW direction about the cavity axis.) These dancing sequences involve two or more MLO's in a rapid and chaotic motion, which appears to be more or less centered on the cavity axis. In Fig. 49 we reproduce a representative sequence of four frames (Frames 11164 through 11167). This sequence manifests essentially no evidence for significant correlations between successive frames, hence confirming the rapidity and chaotic nature of the dance. The video format, the PIP problem, and the rapidity of the oscillations (estimated to be some 10's of Hz) make it impossible to unambiguously count the objects (As can be seen, the number of regions of luminosity seems to vary from frame to frame.) or follow the details of their tracks. (A stationary region of luminosity in Fig. 49 is specifically noted in Frame 11165; it appears to be a reflection in the far flange of light from an unseen SPL. There are better examples of such reflections in later figures, e. g., Fig. 70.) This dancing activity continued for >200 frames, at which time the action settled down to a pair of MLO's at rest not too far from the axis of the cavity. (The extended period of dancing evidently dissipated the original angular momentum associated with the initial CCW track motion.) We illustrate this state of repose in Fig. 50. Fig. 50 is evidence for what we call Mode II behavior. In this instance, we have two spatially separated MLO's at rest in the cavity, evidently not in wall contact, for an extended period of time (> 400 frames).

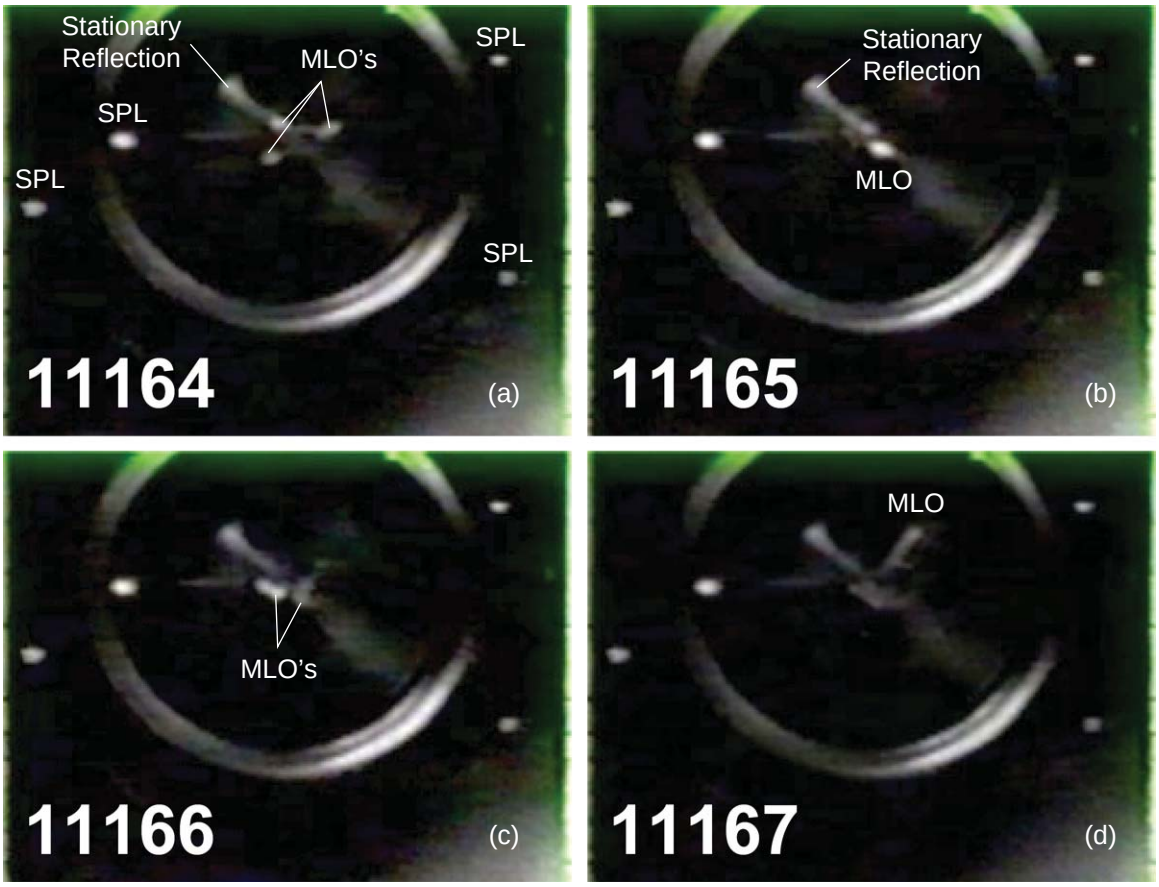

12-2008
8745A54

Figure 49. We show four sequential frames (11164 through 11167) in the first MLO dancing sequence. The dance tracks are indicated. Also indicated is a stationary reflection (evidently from the far flange) that does not participate in the dance. Also indicated (in Frame 11164) are 4 SPL's, which images persist in these locations to Frame 13207 (and beyond)?

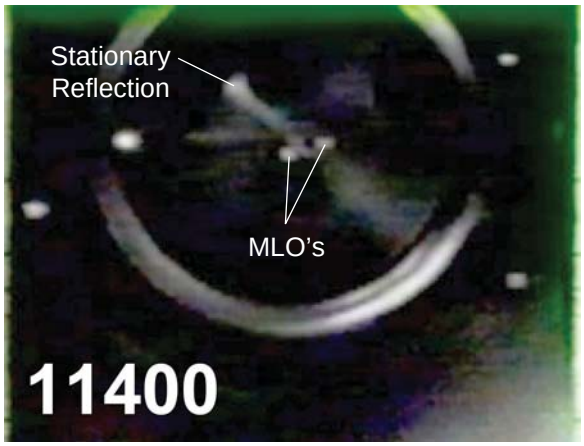

2-2009
8745A55

Figure 50. Frame 11400, at N = 390461: a pair of MLO's at rest. This pair emerged from the first dancing sequence. A stationary reflection is indicated.

As before, we do not have proper data on the *z* region of the above activity, but it would appear reasonable to assume that it would be the same as for the circulation episode, which we discuss in the next section.

7.3.5 Two MLO's merge (Frame 11839)

At the end of this period of repose (>400 frames), the two MLO's moved slowly towards each other until they merged, as is shown in the 9-frame sequence given in Fig. 51. The final frame of that sequence (11841) is dark. In Fig. 52 we show an 8 s plot of the TP and PMT signals, where one can see that at Frame 11840 the PMT signal indicates a reduction in the light level and the TP signal indicates an increase in the cavity excitation level. (To reduce the effects of the high frequency noise in these signals, we have used 15 point moving averages in these plots.) One can suppose that the power required for the light generation prior to Frame 11840 was loading down the cavity, and the excitation level rose when the cavity load factor due to that illumination was reduced. But what caused the reduction in the interior illumination in the first place? (The merger?) More runs with more data will be needed in order to answer this kind of question.

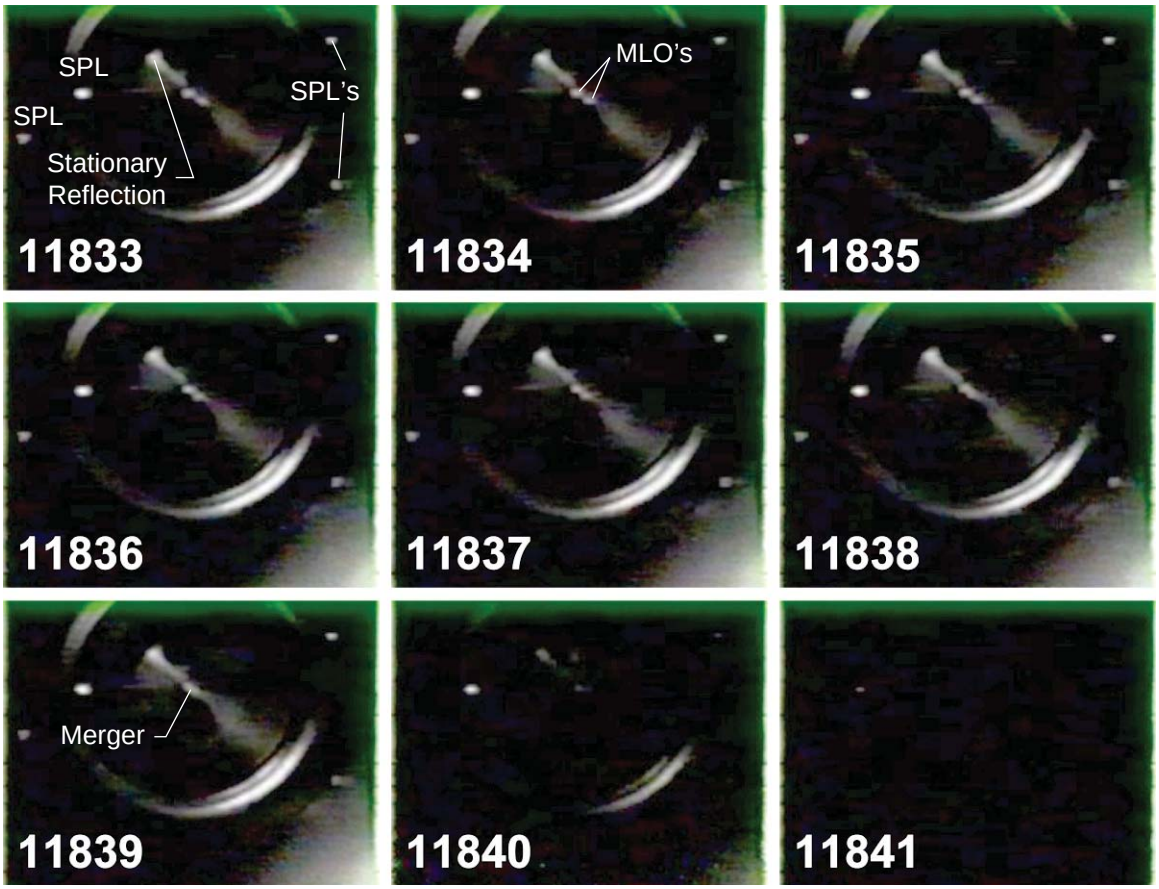

2-2009
8745A56

Figure 51. A sequence of 9 frames that tracks a pair of MLO's moving slowly toward each other. Four SPL's and a stationary reflection are also indicated (in Frame 11833). This motion culminates with their merger in the 7th frame (11839), which is then followed by dark frames. Note that in Fig. 52, after the merger in Frame 11839, we see that the PMT signal drops to zero, consistent with the dark frames, but the TP signal (after a brief dip) actually rises.

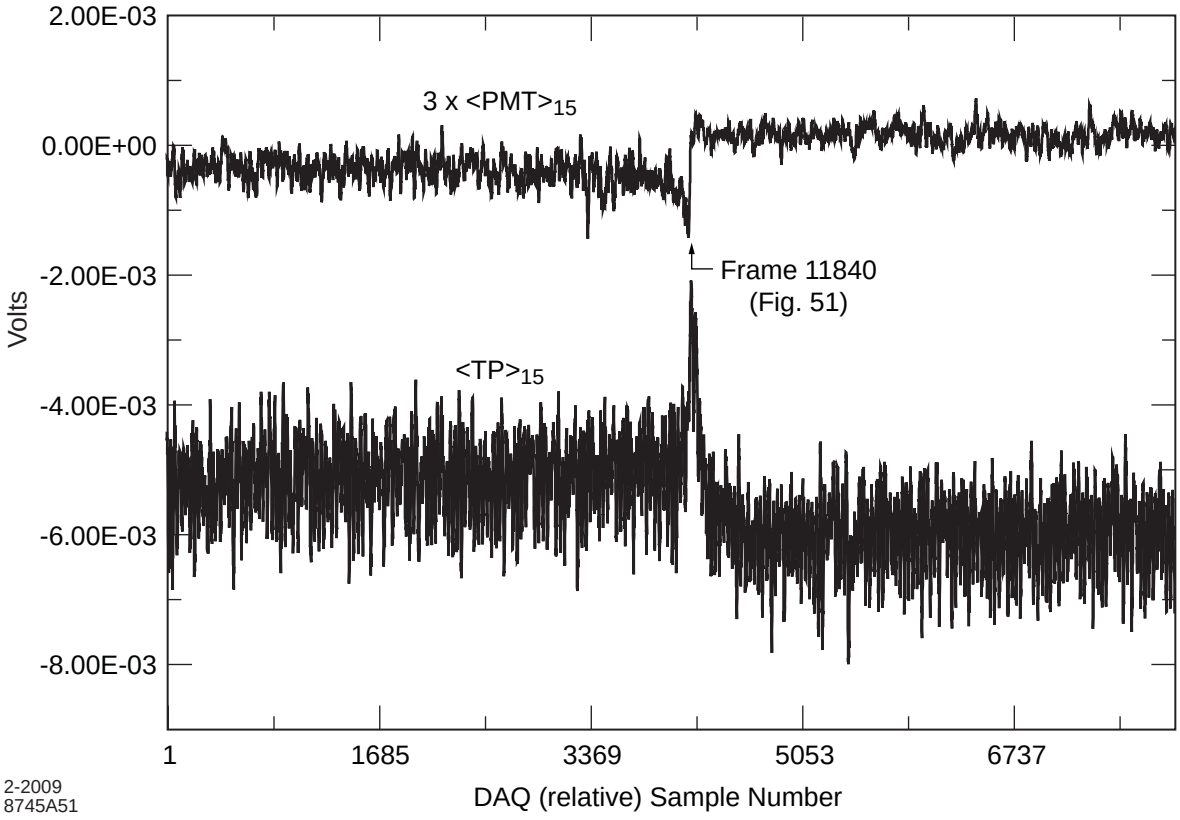

Figure 52. An 8 s stream, starting at N = 401000, of the $\langle TP(N)\rangle_{15}$ and $\langle PMT(N)\rangle_{15}$ signals. The location of Frame 11840 is indicated (cf. Fig 51); its span (33 ms) is too short to be easily seen in this graph.

About 100 ms after the merger, an MLO is again visible. The motion of the image is then seen (for about 20 frames) to progressively increase in velocity and distance from the axis. For the next ~120 frames, this agitation can be reasonably described (again) as a chaotic dance (involving two or more images). This (second) dancing sequence then smoothly evolves into a CW circulation around the cavity axis. Fig. 53 shows a frame as this circulation is beginning, in which one can see a faint image near the axis and a pair of MLO's (which are circulating). The brighter of the pair is at a radius of ~1 cm (assuming that they are in the equatorial plane, see below); the dimmer one is at a slightly larger radius. They are separated by an azimuthal angle of ~35°. The circulation orbits of these two MLO's are well approximated by circles, each of which remains of roughly constant radius during the full extent of this episode. The orbit of the brighter of the two MLO's is indicated (to scale) by a (dashed) circle in Fig. 40, which clearly shows that these MLO's pass directly in front of the images of the two ports in the far flange.

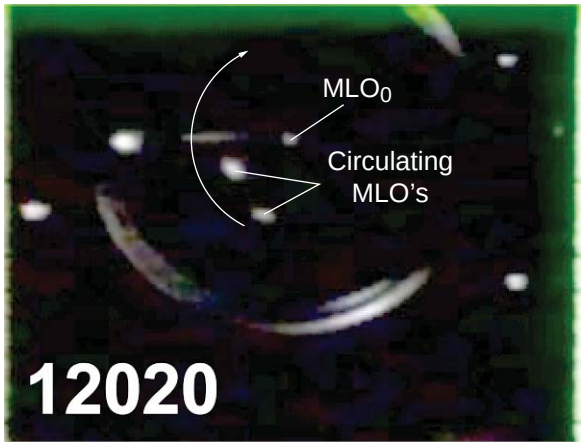

2-2009
8745A57

Figure 53. Frame 12020, at N = 411147: MLO's early in the beginning of the circulation sequence. MLO_1 and MLO_2 are circulating in the direction of the arrow. MLO_0, on the cavity axis, is (essentially) stationary during this circulation episode. The four SPL's indicated earlier are still visible in their same locations.

This circulation continued for >650 frames. During this episode, we counted 30 full rotations in the interval between Frame 12039 and 12463, which yields an average circulation frequency of 2.1 Hz. However, the instantaneous $d\phi/dt$ was not a constant. By measuring in a 5 s interval the $\Delta\phi$ motion between frames, we have calculated the instantaneous circulation frequency $f_c = (\Delta\phi/\Delta t)/2\pi$, which is plotted in Fig. 54a as a function of (relative) frame number. (As technical details, we remark that $\Delta\phi$ is measured from the trailing edge of a track segment forward to the trailing edge of the track in the next frame, cf. Fig. 55. The number of the frame containing the luminous track segment in this span of $\Delta\phi$ is used to plot the resultant f_c data point. An estimated measurement error, $\delta\phi \sim 1°$, leads to a frequency error of $\delta f_c \sim 0.1$ Hz, approximately the size of the diamonds that denote the data points.) One notes that the regions of rapid rotation come in spurts of >4 Hz above a baseline low of <2 Hz. This rather large and irregular variation in f_c is representative of the ~20 s circulation of this episode. In Fig. 54b is plotted the azimuthal angle separating the two MLO's. The dimmer, i. e., outer image (MLO_2) always trails the brighter one (MLO_1) by a separation angle that varies within a finite range, but which is also characterized by large, abrupt peaks.

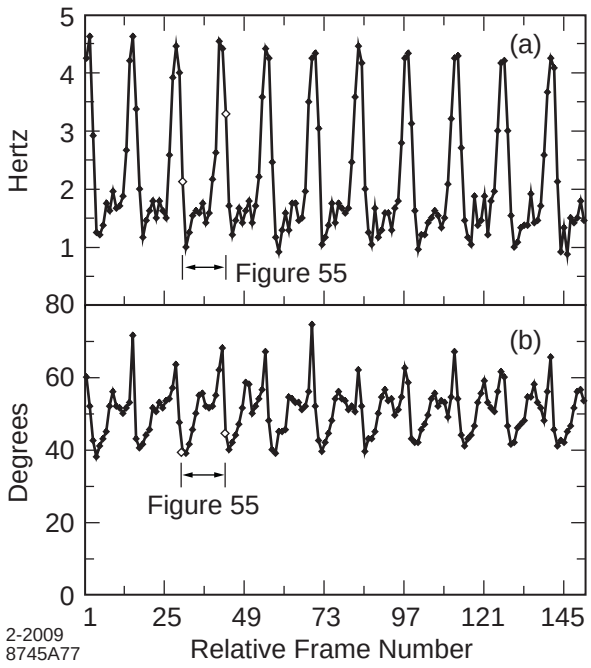

Figure 54. a. Plot of f_c versus (relative) frame number in a 5 s interval starting at Frame 12199. b. Plot of ($\phi_1 - \phi_2$) in the same interval. The span of Fig. 55 is indicated. Open diamonds indicate the first and last frames of Fig. 55.

Looking in more detail, we see that the azimuthal angle between the two MLO's varies from a maximum of >70° (in near coincidence with the rapid portion of the rotation) to a minimum of <40° (during the slow portion). It is as though MLO_1 is subjected to a brief impulse of force that propels the configuration to continue its circulation about the *z*-axis. Under the influence of this impetus, the configuration is distorted, as is evident from the (correlated) peaks seen in the azimuthal angle plot shown in Fig. 54b. A possible mechanical model for this behavior would be that these MLO's represent mass points that are connected together by springs, and that the springs stretch under the force impulses, and then recover again, each cycle. It even appears that there may be some overshoot in the azimuthal recovery phase of each cycle. But if so, this aspect of the motion is highly damped.

In Fig. 55 we show a stacked image (using AutoStack 3, version 3.3) of 14 frames in this circulation sequence (about one full cycle). The location of these frames is indicated in Fig. 54. One notes a larger spacing of MLO_1 at ~ 12 o'clock and a closer spacing at ~ 6 o'clock, consistent with the f_c variations seen in Fig. 54a. The azimuthal separation of these two MLO's is seen to shift the recorded azimuthal location of the rapid motion and slow motion of MLO_2. For example, the maximum velocity in this latter case appears to be near 10 o'clock.

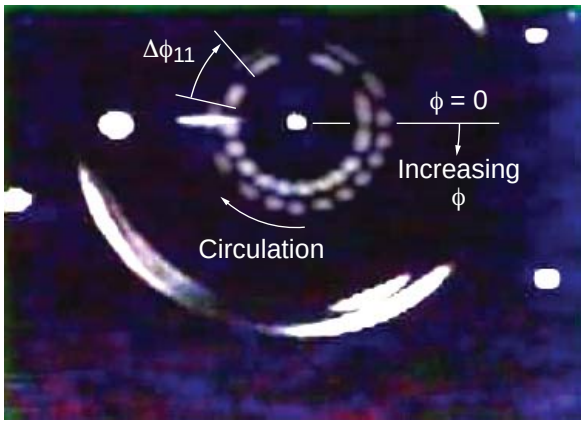

2-2009
8745A72

Figure 55. A stacked image of 14 frames (12228 through 12241) in the circulation sequence. An arrow indicates the direction of circulation (the 11th frame in the stack). The direction of $\phi = 0$ (the positive x-axis), relevant to the plots in Fig. 54b, etc., is indicated. (ϕ increases in the CW direction.) A typical measurement of $\Delta\phi$ is also indicated. The frame stacking caused the 4 SPL's and the central MLO to saturate and bloom to larger diameters. (No enhancement was used in this figure.) The separation between sequential MLO images is due to the fact that only Field 1 is represented in the video field (cf., Figs. 7 and 10).

Fig. 54 shows that the abrupt peaks in the two distributions are correlated in time. It is interesting to observe that these peaks are also correlated to the cavity geometry. Fig. 56, which is a plot of f_c vs ϕ_1 (MLO_1) for the 14 frames of Fig. 55, shows that f_c is a maximum near 270° (12 o'clock in Fig. 55). In Fig. 57 we show a scatter plot of f_c vs ϕ_1 throughout the entire episode. Since δf_c is small, the scatter in this distribution is mainly due to variations in the orbits of the many circulations. Thus, Fig. 57 confirms the rather broad peak of high f_c around ~270°. And it is present at that location in each circulation.

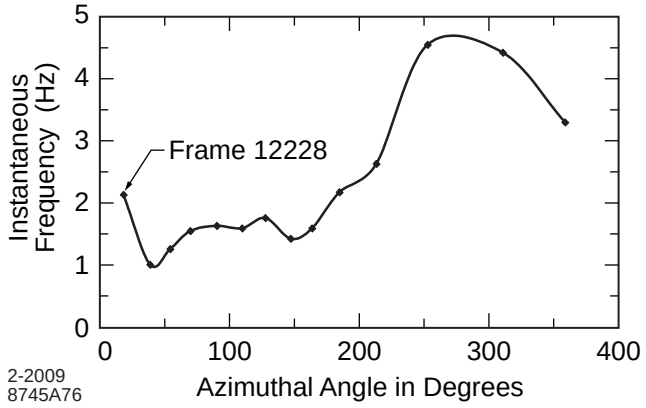

2-2009
8745A76

Figure 56. Plot of f_c versus ϕ_1 for the stacked frames shown in Fig. 55.

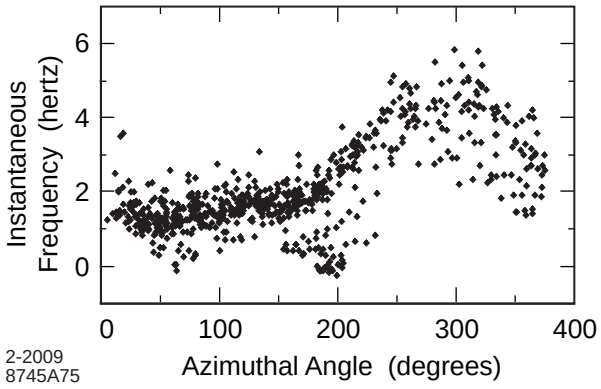

Figure 57. Scatter plot of f_c versus ϕ_1 for the entire circulation episode.

In reviewing the entire episode, we find that the mean (as well as the peak) f_c initially showed a general trend of slow reduction with time. This trend continued until near the end of this episode at which time the mean f_c rapidly diminished and then went to zero. (The collection of $f_c \sim 0$ points near 190° in Fig. 57 are from those frames at the end of this circulation episode.) We show in Fig. 58 the MLO's after they have come to rest. (The orientation of this configuration is consistent with the final data points in Fig. 57.) It is particularly noteworthy to observe that the MLO's are again in a kind of macromolecular formation (nearly identical to the one seen in Fig. 53) with MLO_0 near the *z*-axis and two others on radial lines about 55° apart, straddling the 7 o'clock azimuth. While it appears that the azimuthal separation angle was somewhat stretched during this episode, we observe that the final angle was within the range shown in Fig. 54b. We also note that the final resting azimuth of the configuration was near the low points of f_c, as seen in Fig. 57. Thus, the macromolecular configuration was topologically invariant throughout the circulation period. MLO_0 near the cavity axis remained near the axis, and the other two (roughly) maintained their relative separation while moving in (essentially) circular orbits about the axis. This observed long-lived stability of the macromolecular configuration of several MLO's throughout the course of a rather complicated motion is indeed quite remarkable.

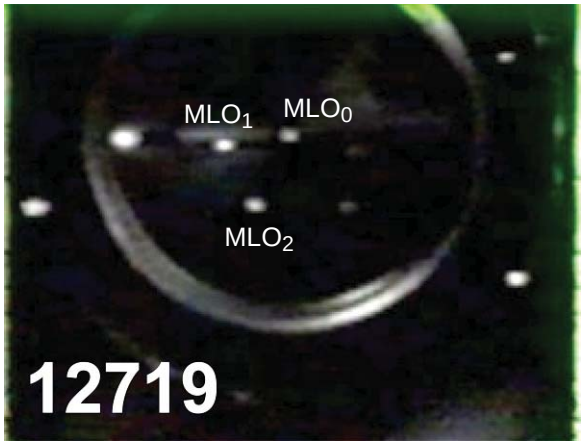

Figure 58. Frame 12719, at N = 434470, after the circulation has stopped. We see the macromolecular formation of three MLO's at rest in the cavity, and the same four SPL's.

In considering the *z* location of this circulation motion (as well as the chaotic dance described in the prior section), we make the following observations. Toward this end, it is useful to visualize a line of sight from the camera lens that traverses an MLO image. Only two physical surfaces intersect this sight line: 1) the camera viewport and 2) the far flange; the cavity vacuum resides between these two surfaces. In the course of the many circulation cycles, the images of the MLO's (which can be easily followed in contrast to those of the dancing sequences, which cannot) always move smoothly across the locations of the ports in the far flange without any acknowledgement of the existence of those ports. Thus, they cannot be located on the far flange. As an aside, this detail of the circulation motion also precludes the notion that these tracks are the result of an image reflected off of the surface of the far flange. On the other hand, if the images were due to a discharge on the camera viewport window, being only a few cm from the camera, these images would be completely out of focus, which is inconsistent with the data. Therefore, we argue that these moving images cannot be due to some kind of surface discharge or reflection. By logical extension, then, this line of argument leads to the conclusion that, as we averred for the orbits of Run 1, the activity described herein is due to a number of luminous objects freely moving around in the vacuum space of the central region of the cavity without any wall contact. Invoking a symmetry argument, one expects these motions to be in or near the equatorial plane of the cavity. One avenue for this symmetry argument to be valid would be that the MLO's experience a long-range repulsion force from the cavity walls. For example, it is well known that a magnet is repelled by a superconducting surface [16]. (Magnetic poles are repelled by their images while electric charges are attracted by theirs.)

In addition to the MLO motion without wall contact, it is striking to note that this macromolecule of MLO's can settle into long-lived stable locations at rest in the central volume of the cavity, e. g., as is shown in Fig. 58 (as well as additional figures illustrated below). And we emphasize that these configurations are evidently not in direct contact with any interior surface of the cavity. Again, the acronym MLO appears to be appropriate.

7.3.6 Abrupt CW jump of ~90° (Frame 12784)

The data briefly described in this section shows that the angular orientation of the equilibrium position of the macromolecular formation can vary as a function of unknown and changeable conditions in the cavity. For example, after remaining for 65 frames in the stable equilibrium orientation seen in Fig. 58 (Frame 12719), an abrupt CW jump of ~90° occurred in Frame 12784. This jump was followed by a slow CW rotation of ~1½ turns. The rotation stopped at Frame 12836 and then slowly regressed ~ 45° in ϕ. The macromolecular configuration is shown at rest in its new equilibrium orientation in Fig. 59. Subsequently, there were several more small jumps and rotations, but no full rotations. The macromolecular configuration then established another new equilibrium orientation where it remained until Frame 13208, which we show in Fig. 60. In addition to the original two MLO's off-axis and the one on-axis, one can now see two additional weaker off-axis images. The MLO's represented by these weaker images were probably also extant in the previous frames, but below the threshold of visibility, given the level of cavity excitation at the time of those frames. The macromolecule at this juncture thus contains (at least) 5 MLO's.

At the time of Frame 13208, the (brighter) MLO's had been continuously visible in the video data for ~2100 frames or ~70 s, a considerable increase in longevity over that of the initial two runs.

2-2009
8745A59

Figure 59. Frame 12860, at N = 439175: the 3-MLO macromolecular formation, at rest in a new equilibrium orientation. Note that the angular separation between the MLO_1 and MLO_2 has increased somewhat. The four SPL's are still visible.

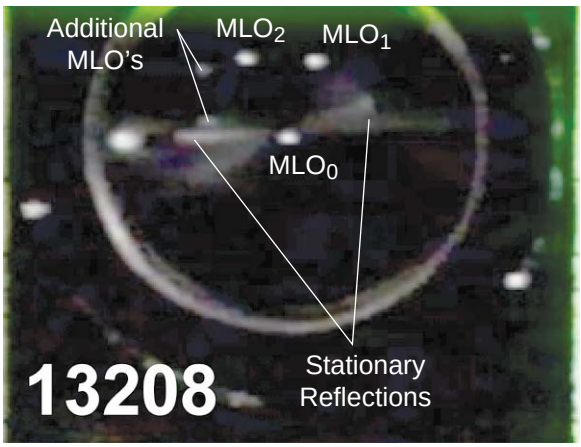

2-2009
8745A60

Figure 60. Frame 13208, at N = 450786: The final frame before Flash No. 2. The three (bright) MLO's (seen above in Figs. 53, 58, and 59) are now accompanied by two weaker images, which are indicated. All five MLO's are at rest in this frame.

7.3.7 Flash No. 2 (Frame 13208)

Eq. (18) indicates that Flash No. 2, at N = 450809, has an ff_{VCR} = 13208.73; that is, it is in Field 2 of Frame 13208. Consistent with this calculation, we have already seen the unperturbed macromolecule at rest in (Field 1 of) Frame 13208 (Fig. 60); the flash, being in Field 2 of that frame, is unobserved. As expected, Frame 13209 is dark. In Frame 13210, one can see only a single SPL. Then in Frame 13211 (Fig. 61), one can see (in addition to the SPL) a pair of faint luminous images. This was followed by ~ 20 frames of what might be described as a rapid jiggle (of shorter duration and less chaotic than what we described above as dances), which involved more limited spatial motion and which, in the end, preserved the general macromolecular form and orientation. The limited extent of the spatial motion and its rapidity is manifest in the blurred images as

seen Frame 13220, which we reproduce in Fig. 62. It should also be mentioned that towards the end of the jiggle motion, when the amplitude of the motion was smaller, the images appear to be moving in a coordinated way, much as though they were imbedded in an elastic solid characterized by a lowest order mode frequency in the ELF band (3 to 30 Hz). For this jiggle motion, one could model the MLO configuration as a collection of mass points joined in pairs by springs, a straightforward extension of the mechanical model mentioned above. In this model, the quiescent lengths of the springs would serve to maintain an equilibrium separation of the mass points.

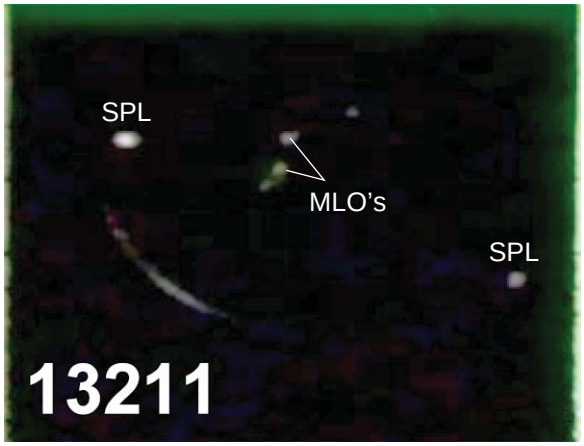

2-2009
8745A61

Figure 61. Frame 13211, at N = 450886: a pair of faint images are again visible. These images are indicated, as well as a pair of SPL's.

2-2009
8745A62

Figure 62. Frame 13220, at N = 451187: one can see three MLO images. Two of them are blurred due to the motion described in the text as a rapid jiggle.

In Fig. 63 we show Frame 13228 (N = 451454), at which time the jiggling motion has subsided. It is interesting to compare the pattern of the 5 MLO's in Fig. 63 to that in Fig. 60. In doing this, we see that the brighter and weaker images on the periphery are in a reordered configuration; evidently the configuration underwent a modification during the jiggle episode. But we don't know if the MLO's stayed put in the configuration and changed their luminosity, or if the (substance of the) MLO's actually changed positions while maintaining (roughly) the same brightness.

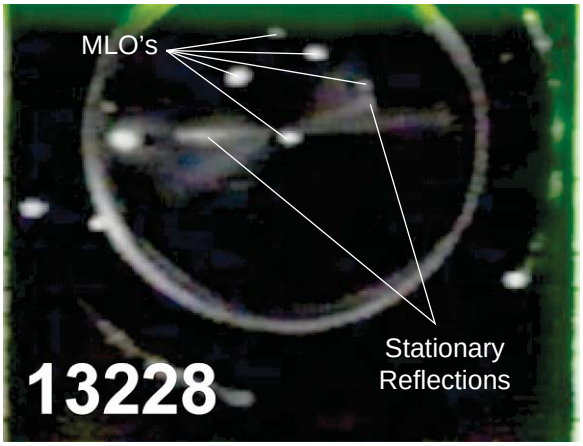

1-2009
8745A63

Figure 63. Frame 13228, at N = 451454: the macromolecule in a new equilibrium orientation after the jiggling motion of the MLO's has subsided. There are again 5 MLO's visible in Frame 13228. Stationary reflections are indicated.

As supporting data for this and the next section, we show in Fig. 64 a 12 s stream of $\langle FGMc(N) \rangle_{15}$ (shifted by +5 mV), $\langle TP(N) \rangle_{15}$ and $\langle PMT(N) \rangle_{15}$ starting at N = 450000. The use of the 15-point moving averages serves to reduce the high frequency noise present in these data streams, affording a clearer picture of the variations in the average values. We note that even though significantly attenuated by the smoothing formula, the TP and PMT transients associated with Flash No. 2 at N = 450809 are still quite obvious in the figure. (There is also a coincident signal in the FGM data.) It is also interesting to observe that the amount of light in the cavity, as indicated by the PMT signal, is not proportional to the level of cavity excitation. In fact, it is not even in a monotonic relationship to the excitation.

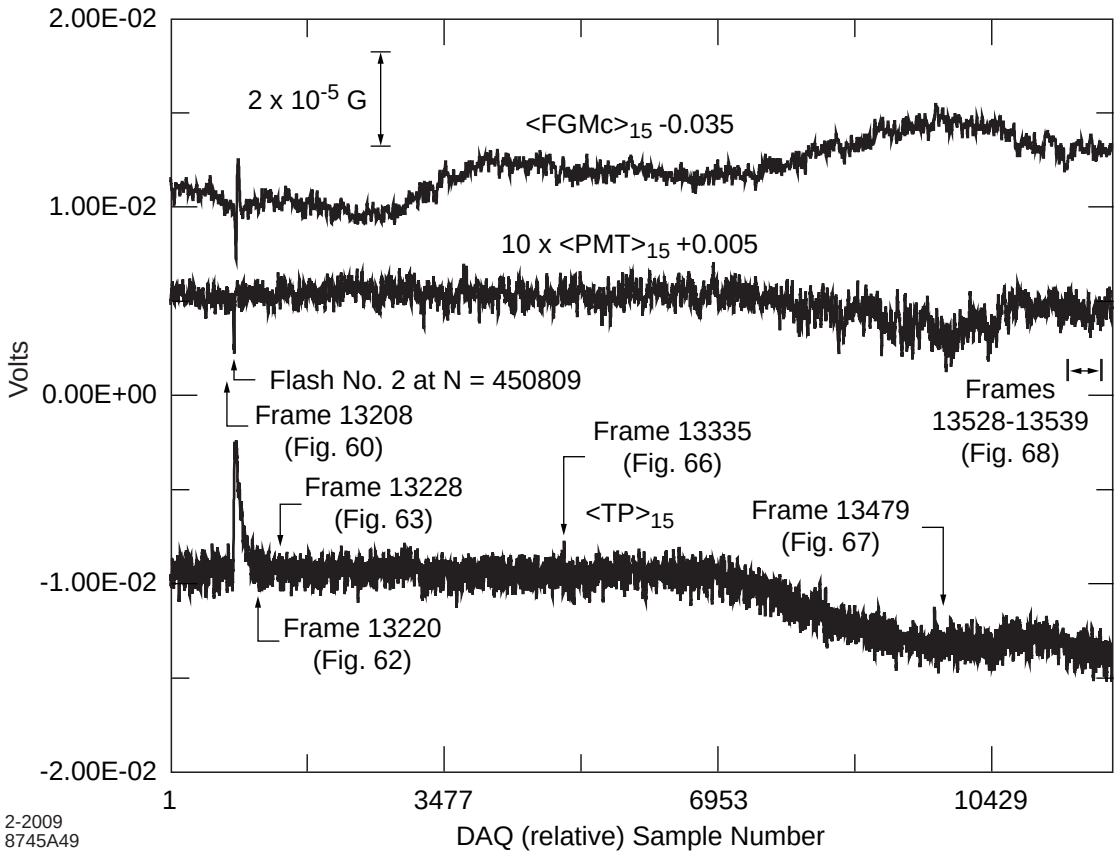

Figure 64. Twelve s plot of $\langle FGMc \rangle_{15}$, $\langle TP(N) \rangle_{15}$, and $10 \langle PMT(N) \rangle_{15}$ starting at N = 450000. As indicated, this interval includes the location of Frames 13208, 13220, 13228, Flash No. 2, the increase in the cavity excitation from Frames 13335 to 13477, Frame 13479, and the span of frames shown in Fig. 68. As per the criteria defining a flash, Flash No. 2 does drain the energy from the cavity: $TP(450814) = 5.19 \times 10^{-4}$ V. However, as is evident in the figure, the 15 point moving average rounds off this brief zero in the data.

At this point, one might also wonder if the MLO's seen after this flash are the same as the ones that are seen before the flash. Since there were two dark frames following the flash, we cannot answer this question with full certainty. (Hence, we discontinued the MLO subscripts, 0, 1 and 2.) However, when the video tape is viewed at the standard 30 frames/s, in the interval between Frames 12719 and 13228 one has the distinct impression that there is "MLO-continuity" through the flash event. If this, in fact, is the case, then the flash and the concomitant loss of cavity excitation does not necessarily cause the demise of the MLO's. (Recall that the flash appeared to terminate some orbits in Run 1, but we presume that that result would be a consequence of the momentary loss of the SPM harmonic oscillator potential well rather than a direct action on the character of the MLO itself.)

7.3.8 Abrupt CW jump of ~75° (Frame 13259)

The ~75° jump in Frame 13259, shown in Fig. 65, initiated an oscillatory motion in ϕ that had a maximum peak-to-peak amplitude of ~120°, a period of ~4 frames (or a frequency of ~7 Hz), and a duration of about 10 frames. We show Frame 13335 in Fig. 66, which displays the equilibrium position somewhat after the ϕ-oscillation had subsided. In this frame, we now see a macromolecular configuration totaling 6 MLO's. The additional

MLO is on the periphery. In considering the results described below, it seems quite likely that the newly visible MLO was in the configuration all along, but became visible due to an increase in the level of cavity excitation (cf. Fig. 64). In Fig 67 we show Frame 13479, which is after a further increase in excitation. Here we see the same 6 MLO's, but they are somewhat more luminous than in Fig. 66. We can also see a pair of bright SPL's with clear reflections of their light from the far flange. (As before, we attribute the form of these reflections to the concentric circles left over from the machining of the inner flange surface. It is therefore logical that these reflections form a line that aligns with the azimuthal angle of the source SLS and passes through the center point of the flange.) While it is not evident in these single frame images, we point out that these SPL's and their reflections do not move during the jiggle and oscillation episodes.

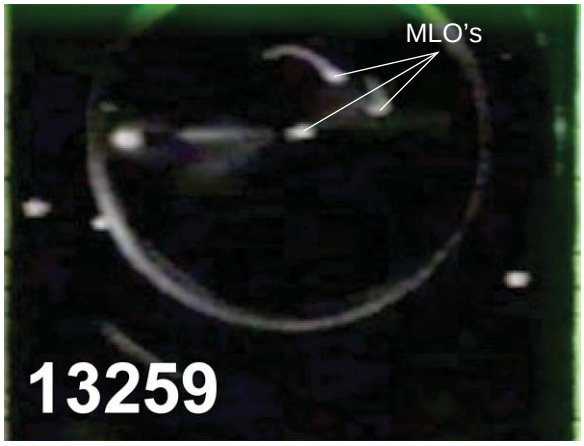

1-2009
8745A64

Figure 65. The 75° CW jump in Frame 13259 at N = 452586. We see a blurring of the (indicated) off-axis MLO images due to the ϕ-motion.

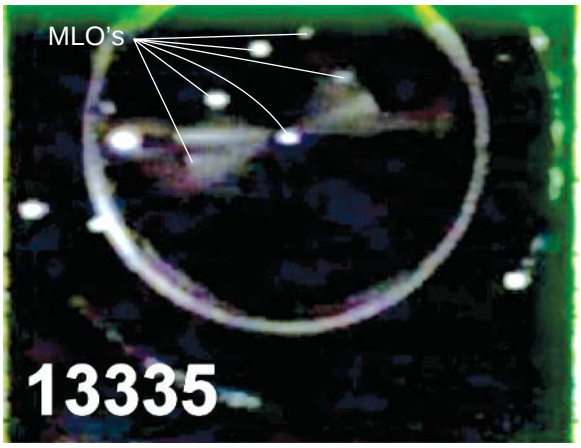

2-2009
8745A65

Figure 66. Frame 13335, at N = 455022, shows the macromolecule somewhat after the ϕ-oscillation initiated in Frame 13259 has subsided. Six MLO's are now visible.

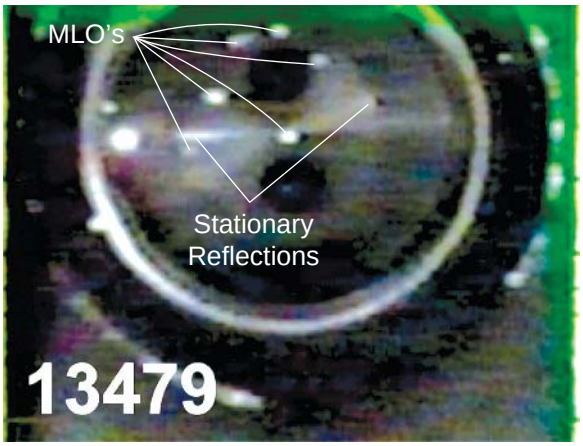

2-2009
8745A66

Figure 67. Frame 13479, at N = 459828, shows the macromolecular configuration in which 6 MLO's are visible, but in a somewhat different arrangement than that in Fig. 64. Note also the bright SPL at the 9 o'clock azimuth and its reflection in the far flange.

One of the most intriguing sequences of this run is shown in Fig. 68, which exhibits a 12-frame sequence (Frames 13528 through 13539), in which two MLO images (A and B) are seen to exchange places (and then re-exchange places) while the other four images retain their original spatial relationships in the 6-MLO macromolecular configuration. We illustrate another perspective of this exchange motion in the azimuthal plot given in Fig. 69. This plot, of course, is a projection, and, as is clear from Fig. 68, the MLO's in question do not actually come in contact.

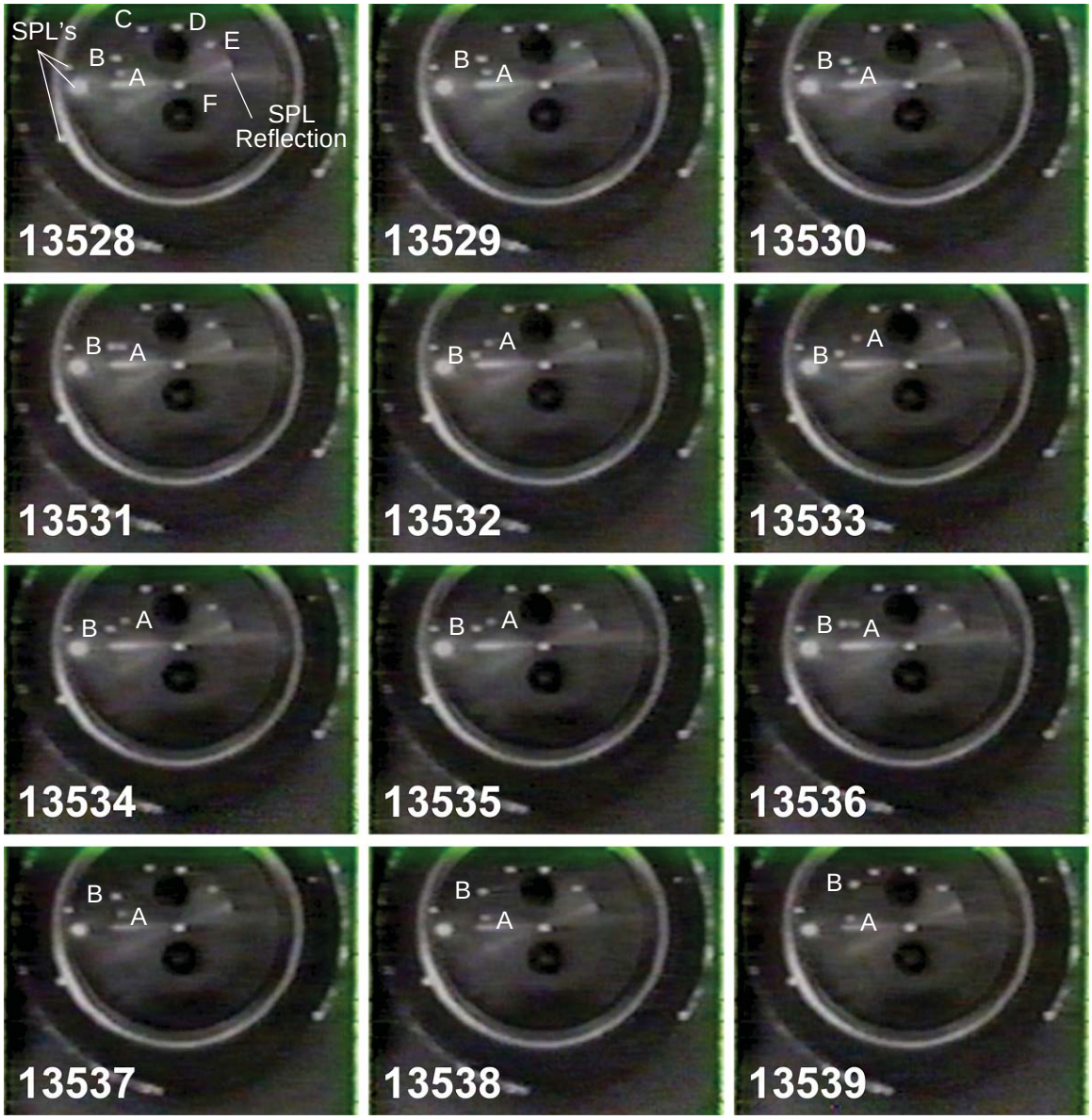

1-2009
8745A67

Figure 68. A 12 frame sequence (Frames 13528 through 13539: 461328 < *N* < 461845) tracing through the motion of two MLO's (A and B) exchanging, and then re-exchanging, their locations in the 6-MLO macromolecular configuration (A through F).

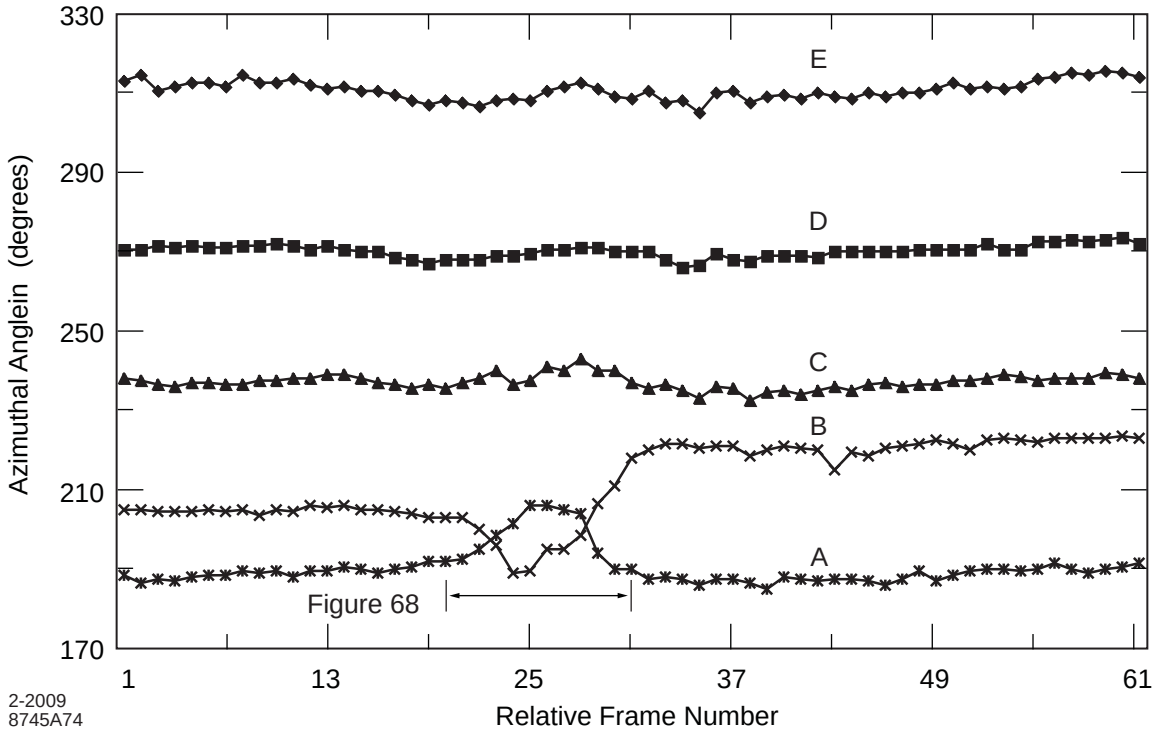

Figure 69. Two s plot, starting at Frame 13509, of the azimuth angles of the five peripheral MLO's, clearly showing that MLO_A and MLO_B briefly exchange places. The data points for the frames of Fig. 68 are indicated. Although the traces cross, the MLO's do not actually contact because, as can be seen in Fig. 68, they are at different radii, MLO_A being at the smaller radius.

This motion appears to be a response to an adiabatic motion of the equilibrium locations of the MLO's rather than a dynamic motion of the MLO's about their equilibrium points. While MLO_A and MLO_B pass in close proximity in the two-dimensional projection afforded by the video frames, since one is unsure of their relative *z*-locations, there is some uncertainty in the knowledge of the actual spatial 3-dimensional separation of the two MLO's. This uncertainty obscures the implications of this episode on the forces that will be required to furnish a proper description of the macromolecular MLO-MLO dynamics. Nevertheless, it is interesting to contrast the MLO-MLO avoidance maneuver exhibited here with the MLO-MLO merger shown in Fig. 51.

Finally, we show Frame 13872 in Fig. 70, in which, with somewhat increased cavity excitation, one can see that the macromolecular configuration has grown to 7 visible MLO's. (As with the other figures, we have taken care to choose frames in which the MLO images do not blend with the SPL reflections; the frame-to-frame motion of the MLO's enables us to easily do this.) Not only are the ports in the far flange visible in this figure, but we also see that the location of the far iris is limned by a full ring of light. The uniformity of this light implies that the source is (probably) of large area, and probably not on the iris itself. The near iris can be located by another ring of light, which is much more irregular in brightness and is not a full circle. It appears that this light is comprised by a combination of SPL's and reflections. The "original" SPL's and their reflections are still visible in their same locations. It is particularly interesting to note that the very bright SPL actually appears to be beyond the far iris and located on the far beamtube near the iris weld seam. This SPL appears to be quite large, perhaps as much as a couple of mm. However, as was discussed above, it is quite possible that most, or all, of the large

apparent diameter of this image could be due to optical effects associated with the camera lens. (It is known that small bright images can bloom to a representation that far exceeds their actual sizes.) Hence, the interpretation that the SPL could be point-like remains plausible. Such a conclusion would be consistent with data on the size of field emission sites, which indicate that they measure 20 μm at most [Ref. 8, p. 245].

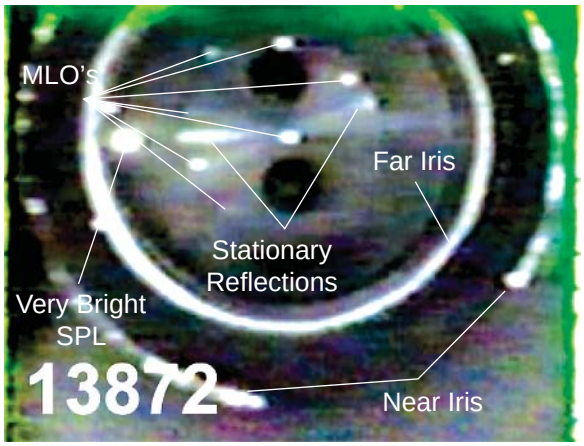

2-2009
8745A68

Figure 70. Frame 13872 at N = 472940, in which we now see seven visible MLO's. Some stationary reflections are also indicated.

7.3.9 Flash No. 3 (Frame 13907)

This flash knocked the RF power off resonance, causing a full loss of the TP signal for ~12.5 s. The return of power (TP jumps to ~15 mV at N = 486621) is captured in Frame 14283, in which one can see a single SPL. In the next frame, one can see a pair of SLS's, and in the frame after that, three (these frames are not illustrated). These images then brighten to a steady state in Frame 14289, which we reproduce in Fig. 71. In this frame we also see at least four SPL's, as indicated in the figure. (There is not yet enough interior light to be able to discern the outlines of the ports in the far flange.) This steady state persists until Frame 15481, or for about 40 s. At this juncture the cavity excitation began to increase. We show this increase in Fig. 72, which is a four s stream of $\langle FGMc(N) \rangle_{15}$, $\langle TP(N) \rangle_{15}$, and $\langle PMT(N) \rangle_{15}$ starting at N = 525000. In Fig 73, we reproduce Frame 15490, which shows the general increase in light level that accompanies the increase in the TP and PMT signal. (The location of Frame 15490 is also indicated in Fig. 72.) In Fig. 73, we can observe that the CID is again sufficient to enable one to see the outlines of the ports in the far flange. There are a number of SPL's seen in Fig. 73. But note that there are no visible MLO's in Fig. 73; they have been absent since Flash No. 3.

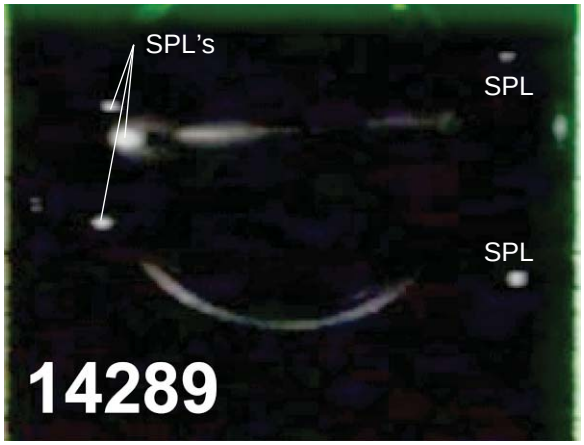

1-2009
8745A69

Figure 71. Frame 14289 at N = 486583, in which the SPL's are much brighter. (The MLO's have not been visible since Flash No. 3 at Frame 13907.)

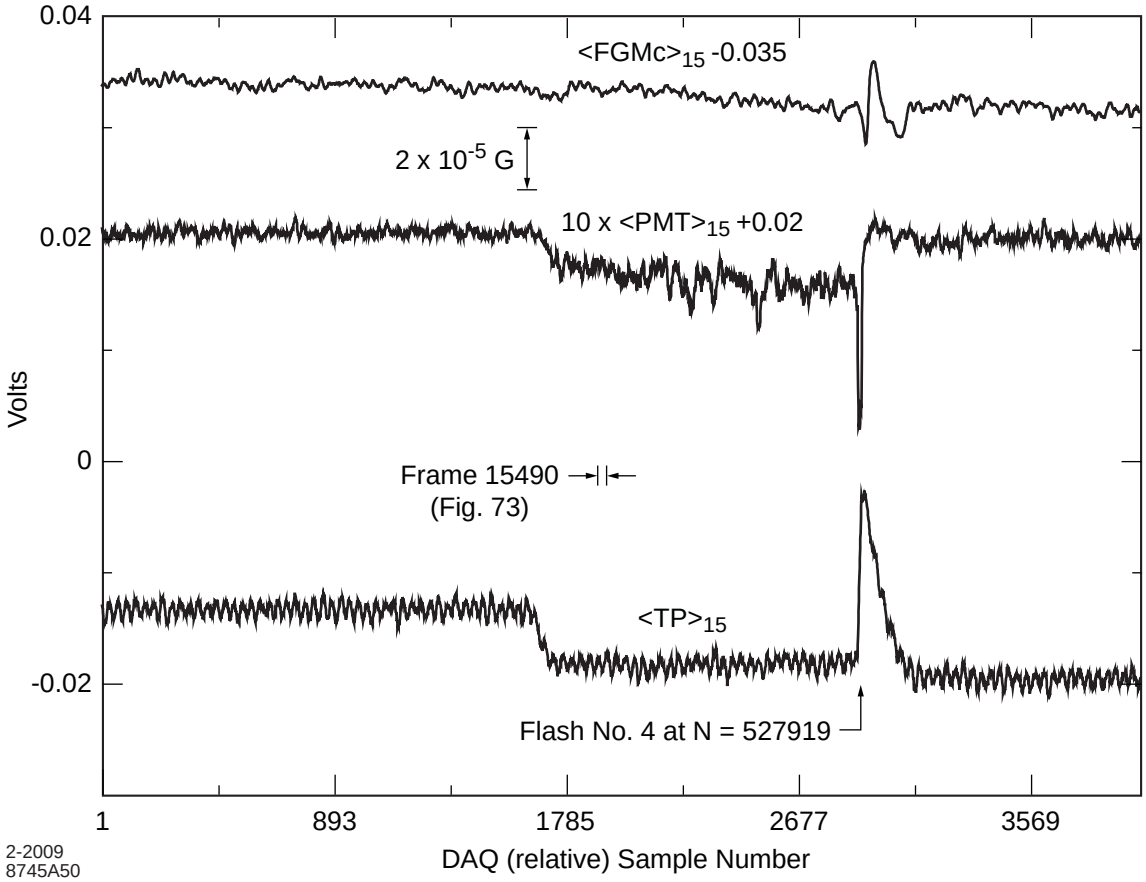

2-2009
8745A50

Figure 72. A 4 s stream of $\langle FGM(N)\rangle_{15}$, $\langle TP(N)\rangle_{15}$, and $\langle PMT(N)\rangle_{15}$ data starting at N = 525000. This interval shows the transition into the region of general interior illumination, discussed in the text, and also includes Flash No. 4 at N = 527919.

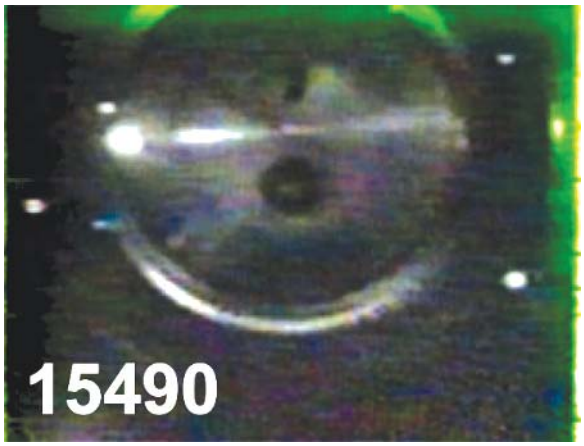

2-2009
8745A70

Figure 73. Frame 15490 at N = 526928, in which we have in addition to the SPL's, a considerable amount of light from a continuous interior discharge.

In Fig. 74 we display a scatter plot of selected data points of the (locally averaged) TP excitation vs the simultaneous (averaged) PMT signal. The various points are annotated with relevant (video) figure numbers. (Figs. 61, 62, and 63, which fall in close proximity in this plot, are represented by one point.) The number in parentheses following the video frame number refers to the figures containing the relevant DAQ data streams. The plotted TP and PMT data points were obtained by taking time averages from 1 to 10 seconds in length; longer intervals were used when the TP signal remained sufficiently flat. As a result the standard deviations appropriate to the data points are equal to or smaller than the actual size of the actual data point representations in the plot. The scatter plot points are corrected for the initial quiescent TP and PMT levels before the power is turned on. (By subtracting, e. g. $\langle TP_i \rangle$ from $\langle TP_0 \rangle$, the data points are displayed as positive signals.) One sees that the point labeled "Finish" (after the cavity power was turned off), by returning to the origin of the plot, is consistent with the initial values.

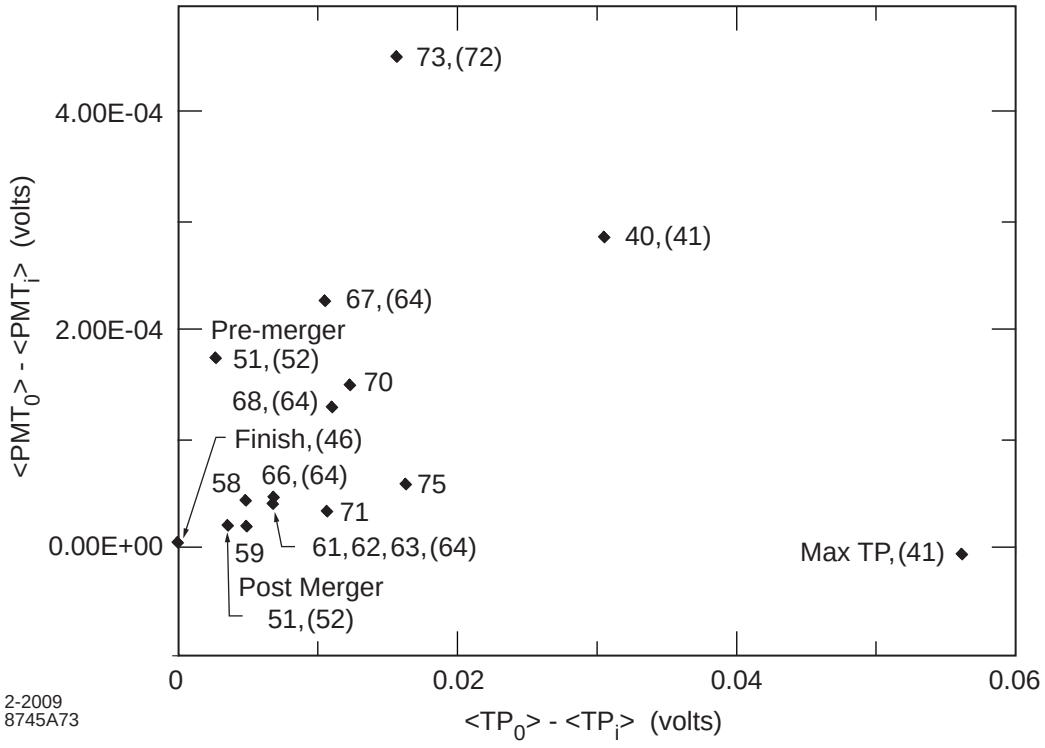

Figure 74. Scatter plot of the correlations between the DAQ values of the TP and PMT signals averaged about selected points. The relevant figures associated with these points are indicated.

7.3.10 Flash No. 4 (Frame 15519)

The Flash No. 4 signature in the TP and PMT signals is easily visible (at $N = 527919$) in Fig. 72. (There is also the characteristic pulse in the $\langle FGMc(N) \rangle_{15}$ plot.) The subsequent frame (15520) is dark. Shortly thereafter, the MLO's can again be seen, but they are more difficult to discern. As an example, in Fig. 75 (also included in the Fig. 74 plot) we show Frame 16090, which exhibits three visible MLO's as well as some SPL's.

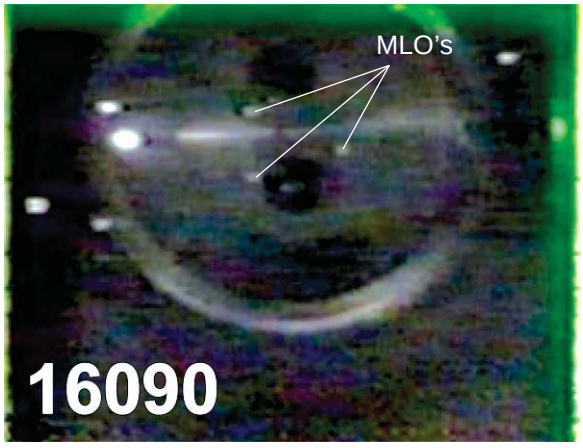

Figure 75. Frame 16090 at $N = 546947$, in which one can see 3 MLO's and several SPL's.

It should be mentioned that from this point forward, the MLO and SPL visibility was episodic. At least two factors are relevant: 1) the MLO's and SPL's may have been, in some absolute sense, less luminous, and 2) there was a discharge in the cavity, which, as we have argued above, causes the auto-iris to close down. Obviously such an action would render less visible any MLO's or SPL's still active in the cavity. In this portion of the video data, when the MLO's were visible, it appeared that there were several present in Mode II configuration. They were generally at rest or moving relatively slowly (much slower than in the circulation episode described above) in a circular orbit (CW), which motion made it easier to pick them out. As with Flash No. 2, which only briefly zeroed the TP signal, the MLO's also appeared to remain in the cavity vacuum after Flashes 5 through 8. Thus, it may be that the Mode II MLO configuration is more robust than that of Mode I. Beyond that, from a qualitative point of view we found nothing new in this portion of the data, and hence we do not review it in detail.

7.3.11 Flash No. 8 (Frame 24041)

In the data following Flash No. 8, the general sense of rotation of the macromolecular MLO configuration appeared to reverse and was predominantly in a CCW direction. It should also be mentioned that after their reappearance subsequent to Flash No. 4, the MLO's were visible off and on for a period of more than 10 min. Of course, because of significant intervals of invisibility and also because of the intervening flashes, confirmation of an MLO longevity of this duration must await further data runs.

8. Discussion

From the data of the nine runs described above, we have drawn specific attention to five types of light emission phenomena, to wit: 1) CID's, 2) SPL's, 3) the flash, 4) the semi-flash, and 5) MLO's, and have shown that there may be a physics relationship between them. Some aspects of our data appear to cover new ground, and some aspects are reasonably well known. While it is well known that high frequency electromagnetic fields can stimulate discharges in gases at modest to high pressures [17-19], our data were taken at pressures well below those in Refs. [17-19]; except for short-term problems like the one in Run 7, mentioned above, our cavity ion pump generally indicated a pressure $<10^{-7}$ torr. The ion pump is, of course, assisted by the interior surfaces of the cavity (at 2 K), which act as a cryopump. It is relevant to note that all common gases at 2 K (except for helium) have vapor pressures $<10^{-11}$ torr [20]. Therefore, one expects that there are far too few atoms in a (clean) cryogenic cavity to support any luminous phenomena originating from atomic (or molecular) transitions. Of course, once a discharge mechanism is initiated, it can desorb gases that were frozen onto the cavity walls. And in this circumstance, one expects that there could be plenty of energetic field emission electrons to ionize the desorped gases. In such cases, with suitable apparatus one would expect to be able to detect appropriate line emissions.

At the present time we are unable to specify a possible mechanism for the stable and continuous generation of light (in particular, CID's and SPL's) in a relatively hard vacuum at cryogenic temperatures; field emission electrons and ionic currents probably play a role, but do not appear adequate to offer a full explanation. In the case of flashes, electrons and ions would be available in copious quantities from avalanches formed at field emission sites, as described in detail in Refs. [7 and 8]. In the following sections we

make some observations based upon our data, point out some challenges to a proper physics understanding, and offer a few remarks about possible theoretical avenues.

8.1 Continuous interior discharge (CID)

In Run 7 we observed a CID that appeared to have a source that is out of the camera view; cf. Fig. 40. Nevertheless, it was bright enough to enable one to clearly discern (by reflected light) the interior construction details of the cavity (e. g., flanges, irises, weld seams, etc.). (It also should be mentioned here that this initial CID did not manifest the general illumination character attributed to ruby fluorescence.) In those intervals in which this CID was active, a larger cavity excitation (larger TP) led to more interior light. However, the relationship of this type of CID to TP is more complicated: early in the run we observed no CID at TP levels that significantly exceeded TP levels that later in the run, in fact, supported a CID.

While acknowledging that the mechanism for light emission in the case of the out-of-view CID is not clear, one possible trail to pursue could be two-point multipacting, which is known to take place in the cavity volume driven by electron trajectories cyclically moving across the equator, generally in regions of low electric gradient, but of larger magnetic fields (i. e., near the equator weld seam) [8, p. 189]. Also, multipacting does not necessarily depend upon field emission electrons for its initiation [7, 8]. We remark that it may be relevant that this CID type was the first of these luminous phenomena to appear in Run 7.

Later in the runs, bright CID's (At times, there was evidence that the amount of light was sufficient to activate the auto-electronic iris of the camera.) appeared in which the light itself was fairly uniformly distributed over the video raster, giving the illusion that it was being generated in the interior (gas) volume (cf. Fig. 12c). This illusion derives from the fact that the light field appeared to overlay the much darker image of the far flange behind it. While it is difficult to imagine how reflected light in the cavity (even from a very bright source) could cause this effect, there is a straightforward explanation that, in our view, should be a primary hypothesis. This is that the illumination seen by the video camera could be ruby fluorescence induced (by vacuum ultraviolet radiation) in the sapphire viewport. As mentioned in *Sec. 6.5*, such ruby fluorescence was specifically observed in Runs 8 and 9, and has been seen in other experiments [14, 15] as well.

8.2 SPL's

We also observed numerous SPL's, and, as mentioned above, it seems appropriate to associate these stationary point-light sources with specific field emission sites; they appear to be on or very near the irises, where one finds the highest electric field gradients in the cavity. And it is clearly germane that such points of light, spatially correlated with field emission electrons, have been observed in high vacuum DC experiments [6], as well as in RF cavities [5]. It is important to note, however, that a large gradient is not the only factor involved. Early in Run 7, we saw periods of large TP voltages but no observed SPL's. The point of interest here is that these large TP magnitudes, with no SPL's, significantly exceeded those TP magnitudes later in the run that nevertheless were adequate to support SPL's.

Finally, there remains the interesting question of how SPL's generate a significant amount of light in a high vacuum environment. The authors of Ref. [5] suggest two possibilities for the luminescence: 1) electroluminescence and 2) thermal radiation from a thermally insulated surface protuberance on the cavity surface. But they go on to say that neither explanation is fully consistent with their data. Possibility 1) does not have the anticipated spectral peaks (or line structure) of electroluminescent transitions, and Possibility 2) does not have the expected shifts in the spectral (black body) peak with varying RF gradients. We also point out that the spectral shapes observed in Ref. [5] are too narrow to be comfortably attributed to black body radiation. (It should also be mentioned that the lack of spectral line structure also militates against luminosity deriving from electronic transitions in excited gas atoms in the vacuum space.)

8.3 Flash of light (FoL)

We have introduced the acronym FoL to include the flash and the semi-flash as subcategories. While (as we argue below) they appear to initially stem from different physical phenomena, there must be an overlap in their physics because, as shown by the analysis above, they both appear to be contributory factors in the appearance of MLO's. A most intriguing aspect of the FoL-MLO correlation is the delay (MOL formation time?) between the (precursor) FoL and the appearance of the MLO (cf. *Sec. 5.7.4*).

8.3.1 The flash

At this juncture, it appears reasonable to take as a working hypothesis that an integral component of the flash phenomenon is the explosive demolition of a field emission site [7, 8]. From the data of Run 1 we showed two examples (Figs. 13 and 14) that indicate the existence of a physics relationship between the SPL and the flash. (And we have argued above that SPL's are located at field emission sites.) That is, the two SPL's in question disappeared at the time of a flash, and remained optically inactive thereafter. Further support for this notion is the fact that well-cleaned cavities exhibit fewer flashes. (Well-cleaned cavities have fewer field emission sites.) And RF processing is also a factor; Fig. 17 shows that the incidence of flashes is very low beyond ~40 min into the run. (By 40 min into the run, one presumes that RF processing has significantly reduced the number of "vulnerable" field emission sites.)

In considering further details, there are (at least) three relevant characteristic times associated with the flash phenomenon. The shortest (as calculated in Ref. [7]) is the initial avalanche build-up time of a few RF cycles, that is, several ns. The next is the energy draining time (by field emission electrons), which the X ray and TP data in Ref. [4] indicate is a few μs. (We should note that with our experimental sample rate of 1000/s, possible large but short spikes of light might fall between successive PMT samples, and thus not have been recorded.) And finally there is the time duration of the visible light emission. In Ref. [15] the light emission duration was seen to be as long as several hundred μs. Our data from Run 7 indicated that this duration can be as long as two ms (see Fig. 42).

The flash phenomenon, as seen in our data, was manifest in a wide range of intensities, from scarcely observable in the video to a fully saturated video field. In these examples of various flash intensities, as with the CID's, it seemed, at times, that the light from the flash was emanating from the (gas) volume itself. (Could ruby fluorescence explain this

aspect of the data?) However, even though it is obvious that there is plenty of energy available, it is a challenge to specify a detailed mechanism for the generation of the light and to understand the ~2 ms duration of the light pulse.

8.3.2 The semi-flash

Eighty semi-flash events were tabulated in Run 1. As a matter of differentiation from the flash, the semi-flash does not drain all of the energy from the cavity; the continued visibility of the SPL's was applied as the operational criterion here. The fact that the semi-flash does not drain the energy from the cavity argues that they do not derive from an avalanche of field emission electrons from an exploding field emission site. (Once such an avalanche starts, it is virtually certain that it will continue until the RF energy is gone.) Another aspect of the semi-flash that differs from the flash is that while there were no semi-flash events early (<30 min) in the run, they continued to appear at significant rates even to the end of the run (see Fig. 17), further supporting the argument against the involvement of explosive demolition of field emission sites.

Semi-flashes appeared to be amorphous in shape, generally not filling the video field. And similar to some flashes, they appeared to emanate from the (gas) volume itself (cf. Fig. 16). However, the fact that the intensity of the semi-flash is not at all uniform in the video field argues against the ruby fluorescence hypothesis as an explanation for this aspect of the apparent source location of the semi-flash luminosity. And if it is true that the source of the luminosity of the semi-flash resides in the vacuum volume of the cavity, a proper physics explanation is indeed a challenge.

8.4 MLO's

Run 1 was the most prolific in the production of MLO's (245). A variety of behaviors of these MLO's were observed. As a general remark, in Runs 1 and 2 MLO motion could be characterized as ballistic (Mode I behavior, see *Sec. 7.3*), that is, moving freely about the vacuum space, subject to various interaction forces, generally without wall contact. Occasionally, however the MLO's were observed colliding with and rebounding from the cavity walls. Reflections of the MLO tracks enabled us to be certain of the wall contact (and in the case of the orbits, the lack of wall contact). In Runs 1 and 2, 13 (closed) orbits were tabulated, four of which persisted in the vacuum space for >10 s. In one of these, the orbiting MLO executed an abrupt kink (in mid-vacuum, so to speak; see Fig. 31), which one presumes was the result of a collision of the MLO with an object below the level of (luminous) visibility.

8.4.1 Long-lived closed orbits and the SPM

The observations in the preceding section support the view that MLO's are discrete objects with a certain long-lived self-coherence and that carry a certain mass, energy, and momentum. As such, one expects that Newton's equations are appropriate for a (mathematical) description of their (ballistic) behavior. Of the data we have in hand, the long-lived closed orbits are the most amenable feature for ballistic study. One approach would be to treat the MLO in the cavity RF field as an electromechanical system. Such a study (the Small Particle Model or SPM) has been published [13]. In the SPM, the MLO is modeled as a small conducting sphere (of radius a) immersed in the (resonant) TM_{010} RF electromagnetic field in a superconducting cavity. (Cylindrical coordinates ρ, ϕ, z are used for the cavity and its fields.) From this model it is shown how a symmetric two-

dimensional radial potential well obtains. In short, (in Gaussian units) the cavity $\boldsymbol{E}$ field induces an oscillating electric dipole moment $\boldsymbol{\mu} = \boldsymbol{E}a^3$ in the sphere, and the $\boldsymbol{\mu}$ interacts with the (oscillating) cavity $\boldsymbol{B}$ field to yield a Lorentz force

$$\boldsymbol{F} = \frac{\dot{\boldsymbol{\mu}}}{c} \times \boldsymbol{B}. \tag{19}$$

Thus, one sees that $\boldsymbol{F}$ is perpendicular to both $\boldsymbol{E}$ and $\boldsymbol{B}$. In the equatorial plane of the cavity Eq. (19) becomes

$$\boldsymbol{F} = -k\rho \mathbf{1}_{\rho}, \tag{20}$$

where k is an equivalent spring constant, and $\mathbf{1}_{\rho}$ is the unit vector in the radial (or ρ) direction. In the center of the cavity, the small amplitude (low frequency) spring constant k_0 was shown to be is

$$k_0 = \frac{E_0^2 \omega_a^2 a^3}{2c^2} \sin^2 \omega_a t = \frac{E_0^2 \omega_a^2 a^3}{4c^2}, \tag{21}$$

where E_0 is the maximum magnitude of the RF accelerating gradient at the center of the cavity, ω_a is the (angular) frequency of the cavity accelerating gradient, and c is the velocity of light. One sine factor comes from the $\dot{\boldsymbol{\mu}}$ and one from the $\boldsymbol{B}$; $\langle \sin^2 \omega_a t \rangle = \frac{1}{2}$.

Radially stable (ballistic) elliptical orbits about the cavity axis are natural solutions (for the orbital projection into the equatorial plane) in this potential well, thus furnishing a straightforward explanation of a major feature of our observed MLO orbits. The ellipse shown in Fig. 1 is a nice example of such an orbit.

The (harmonic oscillator) frequency f_o of such an orbit is given by

$$f_o = \frac{\omega_o}{2\pi} = \frac{1}{2\pi}\sqrt{\frac{k}{M}}\ , \tag{22}$$

where M is the mass of the sphere. As is seen in Table IV, $5 \le f_o \le 80$ Hz. Table IV also indicates that most of the orbits exhibit a measurable orbital precession. And in Run 1 in all cases where the sense of both orbital motion and precession was determined, one finds a specific correlation (i.e., CW & CW or CCW & CCW). In some cases, both senses are exhibited in the same orbit, but upon the reversals of sense, the correlation remained an invariant of the motion.

Both the precession of the orbits and this correlation find a straightforward (qualitative) explanation in the SPM. This follows from the fact that as one moves in the equatorial plane away from the axis of the cavity $\boldsymbol{E}$ is a (weak) function of ρ, to first approximation diminishing by a small coefficient times ρ^2 as ρ increases. Thus, we augment Eq. (21) by writing

$$k = k_0(1 + \eta\rho^2), \tag{23}$$

where η is a small parameter. Since $\eta < 0$ for the SPM in the CEBAF cavity, we find that the frequency of the large amplitude oscillation (along the major axis of the ellipse) is somewhat less than that along the minor axis. It is easy to convince oneself that this correction, deriving from Eq. (23), will lead to the correlated rotation and precession motions that were found in Run 1. (We have verified this assertion by computer simulation.)

N. B. It is appropriate to mention here that there is another force acting on a small conducting sphere that is induced by the resonant electromagnetic fields in the cavity [21]. Qualitatively, this force is due to the interaction of the cavity ***B*** field with the dynamically induced diamagnetic moment of the sphere (also proportional to ***B***). Quantitatively, analysis shows that if the skin depth of the sphere at ω_a is negligible in comparison to the radius of the sphere, this interaction yields a spring constant of the same sign and form as Eq. (21), but one half the magnitude. Similarly, this radially stabilizing force is accompanied by an axially destabilizing force. While this force was not included in the analysis of Ref. [13], its inclusion, which would increase the k_0 of Eq. (21) by (a maximum of) 50%, does not alter the general conclusions developed there and carried forward below.

We summarize the aspects of ballistic or Mode I MLO behavior that appear to be amenable to an SPM description:

- Radially stable elliptical orbits centered on the cavity axis,
- Precession of the elliptical orbits, and
- Correlation between the sense of the orbital rotation and precession.

The above successes support the argument that the SPM affords a credible first step to an understanding of MLO's. However, having detailed some successes of the SPM, it is important to also point out some of its deficiencies. For example, the orbital correlations in Run 2 do not conform to the SPM prediction and thus will require additional physics to be understood. More generally, it is obvious that the numerous manifestations of distortions from elliptical orbits are prima facie evidence for the presence of other forces.

A more significant deficiency is that the SPM does not furnish an explanation for the evident *z* stability of the MLO orbits; in fact, the SPM *z* force (due to the spatial curvature of the off-axis ***E*** field) that is concomitant with the stabilizing SPM radial force was shown to be axially destabilizing. In Ref. [13] it was estimated that a 20 Hz orbit (e. g., Orbit 12) has ~125 *e*-folds of SPM induced axial instability in a 10 s orbital lifetime: the observed >10 s lifetime without another force to render *z* stability is too improbable for plausibility. Again, we see that the SPM is incomplete. Ref. [13] made the argument that there was no obvious physics source for the requisite *z*-stabilizing force that could dominate the axial instability inherent in the SPM.

N. B. If we consider the magnetic dipole image force mentioned in *Sec. 7.3.5* (but not in Ref. [13]) as a possible axially stabilizing force, we observe that (neglecting factors involving orientation angles) this force goes like $Q^2\ell^2/r^4$, where Q is the equivalent magnetic pole charge and ℓ is the length of the dipole [22]. Hence, this force will be

suppressed by a factor $(\ell/r)^2$ in comparison to the standard Coulomb image force. This is a large suppression factor: for an observed MLO ($\ell \sim 1$ mm, say) in (the center of) a cavity ($r \sim 10$ cm), it is $\sim 10^{-4}$. Thus, this suppression factor will tend to reduce the relevance of this force for $h \gg \ell$, where h is the distance of the MLO from the nearest superconducting surface. As a consequence, it appears most unlikely that this dipole image force offers a viable solution to the axial instability problem of the SPM analysis.

Another result of the SPM that appears to be inconsistent with known physics is the derivation of the (mean) mass density ρ_M of the orbiting MLO's. Noting that the mass of a sphere goes like $\rho_M a^3$, we can substitute for M in Eq. (22) and, using Eq. (21), obtain

$$\rho_M = \frac{3E_0^2 \omega_a^2}{64\pi^3 c^2 f_o^2}, \tag{24}$$

in terms of known or measurable quantities. An estimate, made in Ref. [13] for the 80 Hz orbit, yielded $\rho_M \sim 0.0017$ g/cm^3, about the density of air at STP. The point is that at our experimental values for E_0 the SPM force is relatively weak and is insufficient to hold in (a 80 Hz) closed orbit any known solid or liquid material. (Other possibilities to ameliorate this problem, including very low density materials or special geometric shapes, were explored in Ref. [13], but no satisfactory solution was found.) But if we turn to a gas or plasma as a basic structural model for the MLO, serious difficulties in explaining the relatively long-lived self-coherence and stability arise. Perhaps the most stringent of these is to satisfy the requirements of the virial theorem [23, 24], which states that there must exist some force (with a significant inward radial component) to stably contain an energetic collection of particles in a specified volume; the larger the contained energy, the larger the required force. For example, in gaseous stars, gravitation working against the expansion pressure of the thermal energy of the stellar constituents furnishes such a force.

8.4.2 Mode II behavior

The SPM is evidently not able to explain any of the major features of Mode II behavior, as observed in Run 7. While one would expect the SPM forces to still be present (Their derivation was based upon well-established electromagnetic principles.), it is clear that in this run they must be dominated by some new force(s): 1) groups of MLO's found stable equilibrium positions (more or less at rest) in the cavity vacuum, not on the walls (where one could invoke electric image forces) and not on the cavity axis (the location of the minimum of the SPM radial potential well), and 2) these long-lived stable equilibrium positions are once again clear evidence for an axial stabilizing force.

N. B. We remark here that the Mode II behavior of MLO's reveals another problem for a magnetic dipole model for an MLO, should its magnetic moment image force be postulated to be large enough to afford axial stability. In particular, consider the sequence seen in Fig. 68: at their point of closest approach (significantly less than their distance to the nearest cavity wall) the two dipoles (A and B), seeking a state of lowest (mutual) potential energy, would tend to align their moments into the orientation of maximum mutual attraction. In this situation, one would expect the MLO's to move to a common center rather than to separate again, as was actually observed.

These equilibrium formations of MLO's (up to 7 in our data) are in conceptual analogy to molecules – hence our use of the descriptor macromolecular. In pursuing this analogy, we note that the molecular bond and the associated bond length can be viewed as resulting from simple basic (monotonic) forces acting in opposition. While there are several classifications of molecular bonds [25], the one most amenable to a (quasi) classical description is the ionic bond, in which the long-range Coulomb attraction of the ions (e. g., Na^+ and Cl^-) is balanced in equilibrium (at ~2.5×10^{-8} cm) by the short-range repulsion of the (partially shielded) nuclei [26]. This simple picture is consistent with the fact that the lengths of molecular bonds are typically found to be small multiples of the Bohr radius (0.529×10^{-8} cm), which sets the scale of atomic sizes.

However, there are important limitations to the molecular analogy; a notable feature of the observed stable multi-MLO formations is that the constituent MLO's are separated by distances that significantly exceed their luminous diameters. And the MLO bonding lengths are seen to have the capability to (slowly) vary over a considerable range in a continuous and (evidently) adiabatic fashion. In addition, the concept of valence (which derives from a proper quantum mechanical description of the orbiting molecular electrons) appears to play no role.

9. Assessment

At its inception, the goals of the ALE collaboration were two fold: 1) to determine the conditions that are conducive to the experimental production of cavity lights phenomena, and 2) to understand the underlying physics. We believe that some progress has been made on both fronts, but of course many significant questions remain.

9.1 Conducive conditions

The data in hand are very suggestive that two experimental conditions, which in practice the accelerator physicist seeks to minimize, are significant. In fact, both appear to be necessary for the successful experimental production of cavity lights. These are the existence of vulnerable field emission sites that lead to the flash phenomenon (Run 1 in particular) and the presence of a small amount of helium in the cavity (Run 7 in particular). It is interesting to note that in Run 8 there was clear evidence that the helium leak of Run 7 was still active, and CID's (some of which were accompanied by the ruby line in our spectrometer) and SPL's were observed. The fact that no MLO's were observed in Run 8 supports the argument that vulnerable field emission sites are a necessary, but probably not a sufficient, condition. In Run 9 we observed some flashes. We also observed CID's with evidence for ruby fluorescence, implying the presence of some ionized helium (the presumed source of vacuum ultraviolet radiation) in the cavity. Could it be that helium is a required condition, but that there must be "enough," but not too much, helium?

It is clear that it is desirable to try to confirm these hypotheses with additional experimental runs with a more explicit design and better instrumentation. We hope to then be in a position to make more progress on understanding the underlying physics. In this regard, however, it is clear that at this point our data already presents numerous challenges to the goal of a proper formulation of the underlying physics.

9.2 Physics challenges

In the course of this paper we have noted various difficulties in formulating a physics explanation of the luminosity associated with five luminous phenomena: SPL's, CID's, the flash, the semi-flash, and MLO's. (Possible avenues for explanation have also been indicated.) Of these five phenomena, MLO's appear to be the most complicated and the most perplexing. Not only do they emit light, but they also appear to be small discrete stable objects, capable of independent motion in the cavity vacuum for extended periods of time. We have observed two distinct modes of their behavior: Mode I, or ballistic, and Mode II, or macromolecular. (We make the tacit assumption that the internal structure and composition of the MLO's in these two modes are the same, or very nearly so.) While there are numerous questions of detail, in overview, salient general questions include: How are MLO's related to SPL's and FoL's? How are MLO's formed? What are they made of? What is their mechanism for light emission? What forces give them their self-coherence and internal stability? What are the long-range forces that enable them to move for long periods of time without wall contact in stable closed orbits in the vacuum space of the superconducting cavities? What forces enable them to maintain the observed quasi-stable (centimeter sized) multi-MLO macromolecular configurations away from the cavity walls, which configurations can settle into quasi-stable at-rest locations away from the cavity walls? And we have seen that there can be several such locations (orientations) available for a given MLO configuration. Is it possible that we are seeing a new dynamical force regime?

9.3 An intriguing question

A review of the literature reveals that the MLO's observed in these data do not at all resemble the usual low pressure gas discharges. (See also Ref. [1].) On the other hand, several important qualitative features of the observed MLO's are similar to those of ball lightning (BL). Could it be that the MLO is a "little brother" to BL? That is, are MLO's and BL governed in general by the same physics principles, but at significantly different spatial scales? (BL varies in size from a cm to >1 m [27], in contrast to the ≤ 1.5 mm for MLO's.) The similarities are striking. BL forms stable, relatively long-lived balls of luminosity that move about in air (implying that they are of low density) without any apparent source for the radiated energy (actually the MLO has an obvious source: the cavity RF field, but the mechanism for the conversion of that energy into radiation is not clear) and are often devoid of any contact with nearby material objects [27, 28]. And more interestingly, multi-BL formations have been observed [27, p. 36; 29] that resemble the Mode II MLO behavior. (It is also relevant to observe that both phenomena appear to elude a proper physics explanation within the realm of established physics.) Hence, it would seem appropriate to consider looking into BL for a possible explanation of the cavity lights phenomena. Along these lines, Ref. [30] discusses a BL model based upon a kind of electromagnetic monopole that offers the possibility to explain many of these perplexing questions, e.g., the essential nature of the orbiting objects, their interactions, their internal stability, their orbital stability, and their ability to form quasi-stable macromolecular formations. Based upon this model, some experimental predictions can be made, which we plan to explore in future runs.

10. Future plans

10.1 Helium leak

Since there were significant indications that there were helium leaks into the cavities in several of these runs (the evidence in Runs 1 and 2 was not as clear as that in Run 7), it is important that this question be experimentally addressed. In fact, it is appropriate to mention here that a device for the injection into the cavity of a small and controllable amount of helium has been designed and tested. The details of this design will be reported elsewhere. In addition, an experimental run (Run 10) using this device has been carried out. In the course of this run, after a certain amount of helium injection and subsequent to a couple of FoL's, we observed a stable long-lived (~40 s) rocking elliptical orbit. The analysis of this data is not yet complete and will be reported in a later publication. It is planned to verify the efficacy of this device for use in future runs.

10.2 Field emission sites

For cavity preparation prior to a run, we plan to continue using the standard cleaning procedure without the high-pressure rinse. There is good evidence that this approach will yield enough field emission sites remaining in the cavity for adequate production of cavity lights; for example, we recorded 10 flashes in Run 7. At some future date, explicit efforts to enhance field emission sites may be undertaken.

10.3 Optical spectra

It is obvious that to aid any theoretical analysis, it is of primary importance to acquire proper spectral information. In this regard, it would be interesting to go to fused silica viewports to see if the putative ruby fluorescence effects disappear. A next step in this area is to look to improve our USB2000 fiber optics system and its PMT trigger. (The plastic fiber optics cable bundle used to conduct the light from the 2K cavity window to the 300K PMT and the optical spectrometer transmits very poorly for wavelengths >700 nm. However, we have found that standard fused silica optical fibers do not function at all in this application.) This system should yield data applicable to CID's and FoL's, which are large area and often intense sources of light. Another useful step would be to test a transmission grating in front of the video camera, which should yield spectra of localized sources of light, i. e., SPL's and MLO's. Finally, it might be desirable to convey the light out of the dewar by vacuum path directly into a spectrometer, similar to the arrangement used in Ref. [5].

10.4 Video

There are a number of possible steps to be taken in the video area. Obvious possibilities include the use of two cameras for stereo information, and the use of color cameras for elementary spectral data. Cameras with higher scan rates and with more lines per frame are also possibilities. Based on our experience, it appears to be straightforward to accurately coordinate in time the video data from more than one camera with the DAQ data.

10.5 Sampling rate

While it is clear that we can increase the DAQ sample rate above the nominal 1000/s that we used, a more significant improvement would be to set up a triggered fast scan system to better study the time (and spectral) structure of the FoL's.

10.6 Helmholtz coils

An obvious upgrade for the Helmholtz coils would be to significantly increase the number of turns/coil. Additional increases could subsequently be made if it appeared warranted.

10.7 SQUID magnetometer

As part of an effort to improve our sensitivity for the detection of magnetic fields, we are working to develop a magnetometer based upon a DC SQUID, which, unlike the RF SQUID mentioned above, has the capability to operate in the 2 K helium bath used for the CEBAF cavity. The improvement in sensitivity relative to a fluxgate magnetometer is expected to be several orders of magnitude. We anticipate that our major experimental challenge here will be to adequately shield the SQUID and its electronics from the 1.5 GHz cavity excitation power.

10.8 Cavity Q

And finally, if a reliable procedure for producing these phenomena can be developed, it would be useful to follow up the *Q* studies reported in Ref. [1] to see in more detail what effects the cavity lights phenomena have on the *Q* of the cavity.

Acknowledgements

We are indebted to many people for generous assistance with this series of experiments. From SLAC these include T. Anderson for assistance and counsel on the figures; A. Angelov for engineering assistance on the DAQ; R. Badger and A. Kacharovsky for advice and electronic technical skills; G. Bower for numerous discussions and some useful references; J. Hodgson for important numerical calculations; G. Howell, M. Neibel, and M. Racine for counsel and significant technical skills in mechanical construction; A. Novokhatski for useful discussions on MLO equilibrium forces; and especially M. Sullivan for many discussions and significant analysis skills relating to the video data. From JLAB these include G. Ciovati for useful discussions; T. Goodman and L. King for technical skills; P. Kneisel and L. Phillips for useful discussions and some important references; and R. Rimmer for useful discussions on MLO equilibrium forces. One of us (DF) also wishes to thank I. Wieder for many useful discussions and some important references, and J. Sherman for important data concerning Watec video micro cameras.

References

[1] J.R. Delayen, J. Mammosser, Proceedings of the Particle Accelerator Conference, New York, 1999, p. 925.

[2] A.F. Inglis and A.C. Luther, Video Engineering, 2nd Ed., McGraw Hill, New York, 1996.

[3] L. Phillips, C. Reece, T. Powers, and V. Nguyen-Tuong, in Proc. of PAC, Washington, May 1993, Vol. 2, pp. 1007 to 1009, CEBAF-PR-93-044.

[4] G. C. Holst, CCD Arrays, Cameras, and Displays, JCD Publishing, Winter Park, FL, 1998, p. 219.

[5] S. Maïssa, T. Junquera, M. Fauaidy, A. Le Goff, M. Luong, J. Tan, B. Bounin, H. Safa, RF Superconducting Conference, Saclay, 1995, p. 513.

[6] R.E. Hurley, Jour. Phys. D: Appl. Phys. 12 (1979) 2247.

[7] J. Knobloch, "Advanced Thermometry Studies of Superconducting Radio-Frequency Cavities," Ph.D. Thesis for Cornell University, 1997.

[8] H. Padamsee, J. Knobloch, T. Hays, RF Superconductivity for Accelerators, John Wiley & Sons, Inc., New York, 1998, Chapter 12.

[9] W. Feller, An Introduction to Probability Theory and Its Applications, Vol. I, 2nd Ed., John Wiley & Sons, Inc., New York and London, 1957, Chapter VI.

[10] Particle Data Group, Phys. Rev. D66 (2002), p. 229.

[11] L.B.W. Jolley, Summation of Series, Dover Publications, New York, 1961, Eq. (7), p. 2.

[12] H.W. Reddick, F. H. Miller, Advanced Mathematics for Engineers, 2nd Ed., John Wiley & Sons, Inc., New York, 1947, p. 122.

[13] D. Fryberger, Nucl. Instr. and Meth. A459 (2001) 29. [We note that due to a typographic error, a minus sign was omitted from the right hand side of Eq. (2).]

[14] Y. Saito, N. Matuda, S. Anami, A. Kinbara, G. Horikoshi, and J. Tanaka, IEEE Trans. on Electrical Insulation, 24 (1989) 1029.

[15] T. Powers, P. Kneisel, M. Vaidya, Proc. of PAC, Washington, May 1993, Vol. 2, pp. 1010 to 1012, CEBAF-PR-93-045.

[16] K. Mendelssohn, Cryophysics, Interscience Publishers, Inc., New York, 1960, Plate I; D Shoenberg, Superconductiviey, 2nd Ed., Cambridge University Press, Cambridge, 1962, p. 20, and Plate I.

[17] A.D. MacDonald, Microwave Breakdown in Gases, John Wiley & Sons, Inc., New York, London, 1966.

[18] P.L. Kapitza, Soviet Physics JETP, 30 (1970) 973.

[19] Y.P. Raizer, Gas Discharge Physics, Springer-Verlag, Berlin, Heidelberg, New York, 1991.

[20] M.H. Hablanian, High-Vacuum Technology: A Practical Guide, 2nd Ed., Taylor & Francis Group, Boca Raton, London, New York, 1997, p. 130.

[21] A. Novokhatski, private communication to one of us (DF).

[22] W. R. Smythe, Static and Dynamic Electricity, 2nd Ed., McGraw-Hill Book Co., Inc., New York, 1950, Eq. (4); We note that there is a typographical error in Eq. (4); using Eq. (3), it is easy to verify that the r^3 factor in the denominator should actually be r^4.

[23] H. Goldstein, Classical Mechanics, Addison-Wesley Publishing Co., Reading, MA and London, 1950, p. 69.

[24] C.L. Langmuir, Elementary Plasma Physics, Interscience Publishers, New York, 1963, p. 68.

[25] L. Pauling, The Nature of the Chemical Bond, Cornell Univ. Press, Ithaca, 1960.

[26] R.B. Leighton, Principles of Modern Physics, McGraw Hill Book Co., Inc., New York, 1959, p. 295 et seq.

[27] S. Singer, The Nature of Ball Lightning, Plenum Press, New York, 1971.

[28] M. Stenhoff, Ball Lightning, An Unsolved Problem in Atmospheric Physics, Klewer Academic/Plenum Publishers, New York and Boston, 1999.

[29] W.R. Corliss, Remarkable Luminous Phenomena in Nature, The Sourcebook Project, Glen Arm MD, 2001, p. 121.

[30] D. Fryberger, A Ball Lightning Model as a Possible Explanation of Recently Reported Cavity Lights, SLAC-PUB-13583.

Table 1. Overview of Experimental Runs

Run No.	Cavity	Length (min)	Comments
1.	HP1-9105	90	To investigate field emission phenomena. A most prolific run entailing many surprises. Saw numerous MLO's* (many in orbit), SPL's*, FoL's* (both flashes* and semi-flashes*), and CID's*.
2.	5-Cell	53	To further investigate field emission phenomena. Saw SPL's, some CID's, a couple of flashes, and some long-lived MLO's in orbit.
3.	P4-1311	72	Fastidiously cleaned cavity. No MLO's seen✦.
4.	P4-1311	---	Problem with computer control of RF power. No results.
5.	P4-1311	93	No field emission enhancements. Saw a CID, a flash and some MLO's. Determined flash duration to be 1 or 2 ms.
6.	P4-1311	120	Applied a small drop of a slurry of 1μ tungsten powder to iris region of cavity. Saw some SPL's. several CID episodes, some flashes, an MLO, and a surfeit of field emission. Cavity had a low *Q*.
7a.	P4-1311	70	No field emission enhancements. Saw many seconds of a CID with source out of the camera view field, SPL's, flashes, and MLO's. Some of the MLO's exhibited a qualitatively new behavior. Suspect helium leak.
7b.	HP1-9105	37	No field emission enhancements. Paucity of results. Saw some SPL's, CID's, and flashes. Nothing qualitatively new.
8.	P4-1311	72	Same setup as Run 7a. Saw some SPL's (in same locations as in Run 7a), but no MLO's. Saw some CID's accompanied by the 694 nm ruby line.
9.	P4-1311	145	No field emission enhancements. Saw some flashes and large scale CID's accompanied by the ruby line.

* For brief description of various luminous phenomena, see Table II. (More in text.)

✦ After Run 3 we decided to omit the high-pressure rinse step from the cavity preparation procedure to permit the possibility of more field emission sites.

Table 2. Various Luminous Phenomena seen in the Cavity Lights Experiments

Type	Salient Characteristics
MLO:	**M**obile **L**uminous **O**bject: Small size (but apparent sizes differ); manifests self-coherence; long-lived (up to many seconds); significant variations in luminous intensity; moves about in vacuum space for extended periods without wall contact; existence of MLO's in long-lived stable orbits indicates that they carry a certain mass and that Newton's laws of motion are relevant. It is possible that there is more than one type of MLO.
SPL:	**S**tationary **P**oint of **L**ight: Fixed location, generally at or near cavity iris small size (but sizes appear to differ); very long-lived (often for much of the run duration); different intensities, from barely discernable to quite bright; individual SPL intensity varies with cavity excitation; have been observed to disappear at the time of a flash event; presumed to be associated with field emission sites.
FoL:	**F**lash **o**f **L**ight; Includes both the Flash and the Semi-flash, below: statistically found to be a precursor to MLO's.
Flash:	Spatially extended (but not necessarily spatially uniform) production of light; short duration (measured to be 1 or 2 ms); varies significantly in peak intensity, sometimes saturating all of the pixels in the CCD camera; drains all of the RF energy from the cavity; presumed to be associated with the explosive destruction of field emission sites.
Semi-flash:	Spatially extended (but not necessarily spatially uniform) production of light; often region of high luminosity is amorphous in shape and appears to be located in the vacuum space of the cavity; short duration; varies significantly in peak intensity; often saturates a large number of CCD pixels in the video camera; does not drain all of the RF energy from the cavity.
CID:	**C**ontinuous **I**nterior **D**ischarge: covers a large, but not necessarily uniform, area; lasts many frames or even as long as many seconds; the nature of the source of light is uncertain. Sometimes appears to be out of the camera view field; sometimes the light appears to emanate from some kind of gas discharge in the volume of the cavity. Thus, this category probably includes more than one type of discharge.

Table 3. Asymmetry of the two wings of the $\Delta F^{(\pm)}_{(F-M)}$ distribution of Eq. (8**)**

n_b	$N^{(-)}$	$N^{(+)}$	$\mathcal{A}$	$\sigma_{\mathcal{A}}$	$\mathcal{R}$
3	10	9	0.05	0.23	0.23
5	27	11	0.42	0.15	2.86
10	70	17	0.61	0.09	7.17
20	99	27	0.57	0.07	7.82
50	139	55	0.43	0.07	6.54
100	167	81	0.35	0.06	5.82

Table 4. Orbit Summary for Runs 1 and 2

No.	A	B	C	D	E	F	G	H	I
1.	32332	29(f)	54	5	CW	CW	0.15	>9	~ 0.93
2.	51279	33(f)	63↙	~50	CCW	CCW	0.5 to 1.5	4	0.8 to 0.98
3.	53790	5(sf)	22	5	CW	CW	0.06	>9	>0.97
4.	53827	9(f)	39↙	70 to 80	erratic	erratic	erratic	3.4	0.86 to 1
5.	53868	3(sf)	22↙	~7	CCW	CCW	0.9	4.3	NanE*
6.	56604	8(f)	11↙	~20	CW	CW	0.05	3.7	0.97
7a.	56621	7(f)	✯	~25	CCW	CCW	0.2	4.9	0.86 to 0.99
7b.	56808	✯	366↙	~20	both**	both**	erratic	4.1	0.72 to 1
8.	56992	6(f)	28↙	~25	CCW	CCW	0.04	5.6	0.997
9.	64700	5(sf)	194↙	~60	**	Osc.	**	4.8	NanE*
10.	136240	11(f)	449	6.7	both**	both**	0 to 0.14	>9	0.994 to 1
11.	42796‡	9(f)	330	45	CW	CCW	0.7	4.8	0.9
12	42799‡	12(f)	347	22	CCW	CW	0.4	9.3	0.96
13.	42815‡	28(f)	15	20-50	**	CCW	0.25	8.8	0.95

A: Frame number of first visible track.

B: Interval (in frames) between prior FoL and the first visible track of orbit. (f) denotes a flash and (sf) a semi-flash

C: Orbit duration (in frames).

D: Orbital frequency (Hz).

E: Orbital direction.

F: Precession direction.

G: Precession frequency (Hz).

H: Longest major axis (Run 1: cm, Run 2: degrees).

I: Eccentricity. We use the usual definition, $\varepsilon = \sqrt{a^2 - b^2}\,/a$, for eccentricity, where *a* and *b* are the major and minor semi-axes, respectively, of the ellipse [12].

↙ The orbit was (evidently) terminated by an FoL.

* NanE stands for Not an Ellipse.

✯ Run 7 is continuous but has a kink in Frame 56808, evidently a mid-vacuum collision (See text.) Its total duration is listed in 7b.

** See text.

‡ The orbital track segments seen in Fig. 6 (Run 2) are from Orbits 11, 12, and 13.

Table 5. Inputs to the DAQ for Run 7

Channel	Input Description	σ_{noise}(mV)
1.	Video Synch Square Wave*	0.87
2.	FGM Signal (× 25; dc blocked: $\tau = RC = 2.2$ s)	0.94
3.	FGM Signal, dc (Scale: ±200 mG ⇒ ±2.0 V)	0.056
4.	Helmholtz Coil (HC) Input Voltage	0.14
5.	PMT (Negative going voltage signal)	0.14
6.	TP (Negative going voltage signal)	2.6

N. B. The σ_{noise} is the sampling σ.

*The purpose of the video synch signal (a square wave with Field 1 = 0 V and Field 2 = 0.125 V) is to facilitate correlating the DAQ data with the video data.

Table 6. Flash Summary for Run 7

No.	*N*	ΔTP(mV)	τ_{TP}(ms)	Peak PMT (mV)	FGM(10^{-5} G)
1.	380565	–3	~30	0.7	2.8
2.	450809	–9	~90	1.6	2.8
3. [SF]	74124	–15	∞*	4.3	3.0
4.	527919	–16	75	7.4	2.8
5. [SF]	64936	–23	55	9.1	3.8
6.	780811	–26	50	3.0	3.9
7.	805827	–28	40	7.9	3.8
8.	812216	–30	23	14.9	2.5
9.	859472	–28	30	1.4	2.6
10.	1190162	–35	∞*	5.8	2.3

[SF] indicates a flash that saturates (Field 1 in) the video data.

[*] $\tau_{TP} = \infty$ indicates that the RF frequency control loop was knocked off resonance by the flash transient.

Table 7. TP-loss Events in Run 7

No.	Location*	ΔTP(mV)
1.	157180	–58
2.	157695	–15
3.	158447	–15
4.	168306	–26
5.	373548	–22
6.	375116	–56
7.	375672	–48
8.	375964	–31

*The location is defined by the sample number *N* at which the TP signal goes to zero.

Table 8. Significant Reference Points in the the Video Data of Run 7

Frame	Comment
11098	First PMT pulse
11103	Flash No. 1
11105	Typical MLO track
11108	First track of first dancing sequence
11839	Two MLO's merge
12784	Abrupt CW jump of ~90°
13208	Flash No. 2
13259	Abrupt CW jump of ~75°
13907	Flash No. 3
15519	Flash No. 4
24041	Flash No. 8